Measuring the Effects of Drugs on Single Cancer Cell Growth

by

Yaochung Weng

B.S., Electrical and Computer Engineering
Cornell University, 2005

Submitted to the Computational and Systems Biology Program
in partial fulfillment of the requirements for the degree of

Doctor of Philosophy

at the

MASSACHUSETTS INSTITUTE OF TECHNOLOGY

June 2012

Author .....
Computational and Systems Biology Program
March 19, 2012

Certified by .....
Scott R. Manalis
Professor of Biological and Mechanical Engineering
Thesis Supervisor

Accepted by .....
Christopher B. Burge
Director, Ph.D. Graduate Program

Measuring the Effects of Drugs on Single Cancer Cell Growth

by

Yaochung Weng

Submitted to the Computational and Systems Biology Program
on March 19, 2012, in partial fulfillment of the
requirements for the degree of
Doctor of Philosophy

Abstract

Understanding the effectiveness of a drug therapy on halting disease progression is an essential aspect of cancer biology. Conventional assays that study cell behavior after a drug intervention report the average response of a cell population which can mask the heterogeneity and dynamics of seemingly identical cells. Recently, many single-cell techniques have been developed, but there are currently no methods that can fully characterize the long-term effects of drug treatment on cancer cell growth.

To accomplish such, we developed an instrument to measure single-cell growth before and after drug treatment. In order to achieve femtogram-level mass resolution, we employed the suspended microchannel resonator (SMR), a vacuum-packaged cantilever with an embedded channel. Here, we describe three implementations that involve different technologies (optical trap, mechanical trap, and dynamic flow trapping) to capture a cell for repeated measurements and to perform drug delivery.

Applying the technique we developed based on the dynamic flow trapping, we were able to monitor one or more generations of a cancer cell before and after drug treatment. We investigated the growth of mouse leukemia cells in response to drugs that inhibit the mammalian target of rapamycin (mTOR) pathway, induce apoptosis, or prevent translational activity directly at the ribosome. Our method was able to discern a particular growth signature for each drug investigated and to discover a new phenotype in cells following mTOR inhibition. Furthermore, our data demonstrates that the instantaneous growth rate changes following a drug treatment could potentially predict the long-term inhibitory effect on cellular biogenesis and mass accumulation.

Thesis Supervisor: Scott R. Manalis
Title: Professor of Biological and Mechanical Engineering

Acknowledgments

I would like to begin by thanking Scott Manalis, my adviser, for allowing me to pursue engineering and biological research in his laboratory. His resourcefulness, charisma, and enthusiasm have been an emanating source of inspiration to me since the day I joined his group. Throughout my time as a graduate student, he has taught me countless many invaluable skills. Scott's ability to seek out opportunity and to establish collaborations is truly remarkable. Hindsight tells me that I could not have chosen a better adviser. Thank you, Scott.

Next, I would like to express my gratitude to those who helped me substantially along the way. Thomas Burg, who built the first-ever fully-functioning suspended microchannel resonator, took an in-depth interest in subsequent SMR generations. Steven Wasserman imparted to me a small portion of his encyclopedic knowledge on coding, optics, and electronics which was instrumental in the development of my system. I would also like to acknowledge Sungmin Son for our many constructive discussions on fluids as well as Francisco 'Scheeko' Delgado for his collaboration with me on the mechanical traps. Kris Wood of David Sabatini's lab has been a great collaborator and mentor to me during the last stretch of my time as a graduate student.

I am grateful to my committee members, David Sabatini and Roger Kamm, for offering their expert advice to me time and time again. I would also like to thank CSBi for funding me under an NIH training grant and NSF for generously sponsoring me on a graduate fellowship. Both of these financial support kept me afloat for many years and enabled me to think creatively, invent, and pursue the types of research that I did.

Last but not least, I would like to dedicate my doctoral thesis at M.I.T. to my mother and father, Cheng Huey-Min and Wen-Chang Weng, for all of their sacrifices. They gave up everything and immigrated halfway around the earth so that I may have the opportunity to be educated in the United States and to attend the best universities in the world.

Contents

Chapter 1

Introduction

Chapter 1

Introduction

1.1 Background

Traditional in vitro techniques that are used for investigating the effects of a chemotherapy on cancer cells reveal the extent to which a cell population proliferates, performs biosynthesis, or progresses through the cell-cycle. For example, flow cytometric analyses following drug exposure report the percentage of cells that have undergone DNA synthesis based on the measured BrdU incorporation (Fillmore and Kuperwasser, 2008; Olsson et al., 2006; Ouyang et al., 2002). Clonogenic assays monitor cell proliferation by looking for the formation of drug resistant cell colonies 1-3 weeks after the initial treatment (Fiebig et al., 2004; Franken et al., 2006). MTT and MTS assays estimate the concentration of viable cells following drug exposure based on the aggregate color changes that occur when formazan dye is chemically reduced within functional mitochondria (Carmichael et al., 1988; Romijn et al., 1988; Wang et al., 2010). While widely used, techniques such as these provide only the steady state responses of cells to chemotherapy. Furthermore, they report the bulk averages of a population which can mask both the heterogeneous and the dynamical processes of the single cell (Longo and Hasty, 2006; Zare and Kim, 2010).

Without the use of cell synchrony, assays that bulk average across various phases of the cell-cycle cannot discern the time-varying response of an individual cell (Spiller et al., 2010). However, synchronization of a mammalian cell line is not only difficult to

achieve but may also perturb the cells and produce undesirable artifacts in behavior (Davis et al., 2001). Nevertheless, even if perfect synchrony were possible, cell-to-cell heterogeneity would still exist in an isogenic population. For example, the time required after the initial drug treatment for each individual cell to reach a particular event, such as apoptosis, are not uniform even amongst sister cells (Spencer et al., 2009). In addition, cell-fate may not be the same, i.e., the degree to which molecular events are inhibited or affected within a population may differ.

Individual cells contribute to the behaviors of a larger population, and highly resolved single-cell responses may contain information about underlying biological processes that cannot be observed in the bulk (Irish et al., 2006; Reya et al., 2001). One approach that can comprehensively elucidate a cell's response to drug treatment is the direct observation of single-cell growth throughout both its native and its perturbed state (Figure 1). Such measurements not only allow cell-to-cell variability to be distinguished but also enable the contrast of a particular cell's normal behavior with that following drug treatment. In the last decade, several powerful techniques have been introduced to monitor single-cell growth, but as yet there are no methods that can fully appreciate the long-term effects of drug therapy on mammalian cells.

Microscopy has long been the technique of choice when it comes to observing single-cell growth and proliferation. For example, time lapse bright-field microscopy on a microfluidic device has enabled the observation of bacteria before and after treatment with antibiotics (Balaban et al., 2004). However, this technique is limited by its ability to precisely determine the size of a three-dimensional object. The growth rate was not derived from the increase in size of a single bacterium but from the aggregate one-dimensional elongation of all daughter cells arising from a single identified persister cell. More recently, microscopy involving the readout of a fluorescent reporter protein has been used to correlate cell mass to particular events in the yeast cell cycle and to ascertain the exponential growth kinetics of a single yeast cell (Talia et al., 2007). Although in general cell mass is comprised mainly of intracellular proteins, growth dynamics cannot be entirely represented by protein synthesis. Furthermore, this method has not been extended to mammalian cells nor has it been utilized to

observe the effects of perturbation. Quantitative phase microscopy (Davies et al., 1990; Mir et al., 2011; Popescu et al., 2008) can directly measure cell mass, but this technique lacks the necessary precision to determine individual mammalian cell growth. Advanced interferometric microscopy has a much better resolution ($\sim$1% of a mammalian cell's mass in standard deviation), but a recent implementation to study the therapeutic response of mammalian cells (Reed et al., 2011) did not obtain the growth rate before drug treatment. A fundamental limitation of the method, which ultimately precluded instantaneous and frequent sampling of growth rate after drug treatment, was the 1-hour time interval required for cells to settle in a 6-well plate upon introduction of new fluid. In addition, cells were monitored for only five hours following the initial exposure, not long enough to observe potential intergenerational effects.

An ideal method for tracking growth dynamics in response to extrinsic perturbations would allow for direct and precise mass measurements, support the long-term survival and proliferation of the cell under investigation, and enable drug or stimulus delivery to the cell's environment during observation. In order to create an approach that satisfies each of these criteria, we engineered cell trapping and fluid exchange techniques to work in concert with the suspended microchannel resonator (SMR), a sensor that can detect buoyant mass with an unprecedented mass resolution of $\sim$1 femtogram in a 1 Hz bandwidth (Burg et al., 2007).

1.2 System Concept

1.2.1 Mass Sensor

A recent development in mass sensing technology, the suspended microchannel resonator (SMR), has reported a resolution six orders of magnitude better than that of a state-of-the art quartz crystal balance (Burg and Manalis, 2003; Burg et al., 2007). The sensing ability of a micromechanical resonator can be modeled on the same principle that governs a mass on a spring system. Any change in cantilever mass results

in a shift in resonant frequency, f, given by:

$$f = \frac{1}{2\pi}\sqrt{\frac{k}{m^* + \alpha\Delta m}} \tag{1.1}$$

The parameters k, m^*, Δm, and α denote spring constant, effective mass, change in mass, and geometric correction factor. Thus, high sensitivity, or $\frac{\Delta f}{\Delta m}$, is contingent on the cantilever having a low effective mass and a pure ring tone. The quality factor, or Q, is an indication of how well the resonator performs as a mass sensor. The Q factor is inversely related to the amount of damping and is defined as the total energy stored over the energy dissipated per cycle. While unparalleled in detecting minuscule changes of mass in a vacuum, resonators have limited resolution for measuring biological targets which inevitably require a fluid environment. Viscous drag forces from the surrounding impose a substantial amount of damping, thereby increasing the sensor's effective mass and severely reducing the Q factor. The SMR uniquely circumvents this problem by bringing the solution environment into a microfluidic channel embedded within a silicon cantilever while it continues to oscillate in a vacuum (Burg et al., 2006).

A cell transit through the embedded channel (Figure 1-2A) is detected as a downward peak in resonant frequency (Figure 1-2B). From the SMR's perspective, a cell would result in the greatest amount of increase in the sensor's effective mass when it approaches the apex, the most sensitive region of the cantilever. This change in mass, reflected as the maximum change in resonant frequency, represents the buoyant mass of the cell. Defined as the mass of a cell in fluid, the buoyant mass is directly related to the amount of biomass in a cell and can be described mathematically as:

$$m_B = V_{cell} \cdot (\rho_{cell} - \rho_{fluid}) \tag{1.2}$$

where V and ρ are cell volume and density respectively. Since a majority of a cell's biomass is more dense than water, the buoyant mass, as a metric, is analogous to dry mass (Godin et al., 2010).

1.2.2 Basic SMR Operation

The oscillation of an SMR can be maintained in resonant frequency at all times through a positive feedback loop consisted of an optical lever system (Figure 1-3A) and electronics (Figure 1-3B). As in an atomic force microscope (AFM), a focused laser beam is reflected off of the vibrating cantilever (Alexander et al., 1989; Manalis et al., 1996) as it fluctuates in and out of the focal plane. The laser is then collected at a split photodiode where a cyclical focusing and defocusing of light is translated by a photodetector circuit to an analog sinusoid with a period equivalent to the reciprocal of the cantilever's resonant frequency. An oscillator circuit then optimizes the drive signal by amplifying and by phase shifting the sinusoid 90 degrees (Appendix A). The SMR can be actuated either electrostatically via electrodes fabricated within the vacuum packaging or mechanically via a vibrating piezoelectric crystal in contact with the device.

For frequency determination, the photodetector signal is read by a frequency counter (HP 5313A) and by a data acquisition (DAQ) system (NI-6259). The baseline resonant frequency of the SMR typically ranges from 200 - 400 MHz. Although the frequency counter can estimate that value with high precision (error at 10 ppb), it is limited by a readout rate of 2 data point per second. Events such as cell transit which take place on the order of 100 milliseconds cannot be resolved. The second method of frequency determination, the DAQ system, has a sampling clock rate at 80 MHz, but the readout rate is limited by the period of the input signal. In other words, frequency readout occurs only after an entire period of the sinusoid has been measured, or sampled, by the clock. Thus, if the photodetector signal oscillated too quickly or too slowly, certain changes in buoyant mass that result in resonant frequency shifts cannot be precisely determined. In the extreme case, the former would have a readout dominated by noise as not enough samples were taken per period, and the latter would not have enough readouts per second to resolve short time-scale events (Figure 1-4A). Because the resonant frequency shift of interest ranges from 1-100 Hz, a 200 - 400 MHz signal need not be analyzed in its entirety. Instead, the

last 1 KHz of the resonant frequency can be sampled by the DAQ system resulting in peak-to-peak noise $<$ 1Hz and an overall readout rate of 1ms. To achieve this, a multiplier circuit convolves the photodetector signal in the frequency domain with a digitally synthesized sinusoid and then filters for the lower frequency component. The result is a sinusoid with a frequency equal to the difference between that of the two convolved signals (Figure 1-4B).

In addition to the embedded channels of the cantilever, the microfluidics of the SMR device consists of two larger conduits which carry fluids from a reservoir upstream to a reservoir downstream of the mass sensor (Figure 1-5A). These bypass channels enable sample delivery to and from the hollow cantilever. The fluid flow through the device is controlled pneumatically by two computer activated pressure regulators (Proportion Air QPV1-TFEE-030-CXL) that are multiplexed by solenoid valves (SMC S070C-6DG-32). The four fluidic ports to the bypass channels (two upstream and two downstream) are connected via $\frac{1}{32}$" FEP tubings (Upchurch Scientific 1686) to tightly sealed air pressurized containers (VWR 80076-582). Under normal operations, sample is delivered from a single upstream source through the bypass channels to two separate waste vials. The fluid flow rates through the device and across the SMR can be leveraged by adjusting the pressure differential between the source and the waste vials. Each pressurized vial can toggle between one of three pressurized states: P_1, P_2, and atmosphere. The adjustable P_1 and P_2 (gauge pressure range 0-30 psi) correspond to the values set by the computer activated pressure regulators. During a priming or rinsing event, the upstream source is pressurized at P_1 and both the wastes vials are vented to atmosphere (Figure 1-5A). In some situations, pinch flow to force the fluid from one bypass to the other through the SMR may be required. The source and one waste vial is pressurized at P_1 while the second waste vial is pressurized at P_2, where $P_1 > P_2$ (Figure 1-5B). Lastly, gravity serves as a means to finely control the fluid flow through the SMR. The effective pressure within a particular vial can be adjusted by increasing or decreasing the height of the vial or the level of the fluid. Leakage flow across the SMR can either be amplified

or eliminated simply by accounting for gravitational effects without modifying the pressure settings on the pressure regulators.

1.2.3 Cell Traps and Drug Delivery

The primary goal of this thesis is to develop and to utilize an integrative high-precision microfluidic instrument for monitoring single mammalian cell stimulation and drug response. We consider a variety of cell traps that can be implemented within the SMR to capture a cell against flow for instantaneous drug delivery and for continuous mass measurements. Methods such as acoustic wave (Evander et al., 2007), dielectrophoresis (Gray et al., 2004; Issadore et al., 2010), and optical trap (Johann, 2006; Wang et al., 2003) are particularly enticing because no physical contact with a cell is necessary. These techniques form a stable trap around a cell by transferring momentum via mechanical or electromagnetic waves. However, the complexity of the SMR device, including vacuum packaging and multiple glass and silicon layers, makes it difficult to implement acoustic wave and dielectrophoresis without a complete and costly redesign. Whereas acoustic wave require a source in close proximity to the channel, dielectrophoresis require the fabrication of electrodes in a specific arrangement within the device.

Optical trap, on the other hand, is not limited by either of these constraints. It involves the focusing of a high-powered laser beam down to a diffraction-limited spot forming a sharp gradient in photon density. A dielectric object, such as a cell, near the center of the trap experiences a gradient force from the photons it refracts and a scattering force from the photons it reflects (Ashkin et al., 1986; Svoboda and Block, 1994). When the two force components are balanced, the result is a stable three-dimensional trap that sits slightly beyond the focal point of the laser (Ashkin, 2000; Block, 1992; Lang and Block, 2003; Rohrbach and Stelzer, 2002). Chapter 2 describes the design and construction of a prototype optical trap SMR instrument. It also presents hydrodynamic calculations and considerations relevant to not only the optical trap but also to subsequent cell trap implementations (Appendix B).

Mechanical traps such as constrictions (Carlo et al., 2006; Wheeler et al., 2003) or posts (Valero et al., 2005; Werdich et al., 2004) surrounding a dock restrict the movement of a captured cell but continue to allow fluid carrying nutrients and other analytes to pass. Although physical contact with a cell is required, mechanical traps guarantee sufficient force to immobilize a cell against fluid moving at low to moderate flow rates (0.1-1$nL\ s^{-1}$). While adding physical structures to the SMR requires fabrication of new devices, the modification is minor and is limited to the initial reactive ion etching (RIE) step at which the embedded channels of the cantilever are formed. The operation of the device, including functionality and noise floor, is preserved. Chapter 3 details two particular implementations of mechanical trap SMRs: the first conducted density measurements of yeast cells while the second observed the short-term effects of mammalian cells following exposure to sodium azide. Appendix C discusses centrifugal force from the SMR's oscillation, the technological discovery which enables a cell of interest to be trapped on demand within the confines of the mechanical structures.

Godin, Delgado et al. (2010) introduced the concept of dynamic trapping to measure the time course mass accumulation of bacteria, yeast, and mammalian cells within the SMR. While the mass sensor detects cell transits through the cantilever, a control software simultaneously keeps track of the transits and iteratively readjusts the settings on the pressure regulators to prevent the cell from leaving the SMR. The resulting motion of the cell within the channel is analogous to a ping pong ball moving back and forth between two paddles. By combining dynamic trapping with periodic cell storage and a newly developed single-cell manipulation technique to perform drug delivery, we created the microfluidic mass-based analysis of single-cell stimulation, or MMASS, to discover the long-term effects of drugs on cells. Chapter 4 presents the culmination of this work: the utilization of MMASS to study single cancer cells before and after treatment with protein synthesis inhibitors that act on different timescales.

1.3 References

S. Alexander, L. Hellemans, O. Marti, J. Schneir, V. Elings, P. K. Hansma, M. Longmire, and J. Gurley. An atomic-resolution atomic-force microscope implemented using an optical lever. *Journal of Applied Physics*, 65(1):164, 1989. ISSN 00218979. doi: 10.1063/1.342563.

A. Ashkin. History of optical trapping and manipulation of small-neutral particle, atoms, and molecules. *IEEE Journal of Selected Topics in Quantum Electronics*, 6 (6):841–856, Dec. 2000. ISSN 1077-260X. doi: 10.1109/2944.902132.

A. Ashkin, J. M. Dziedzic, J. E. Bjorkholm, and S. Chu. Observation of a single-beam gradient force optical trap for dielectric particles. *Optics Letters*, 11(5):288–290, May 1986. doi: 10.1364/OL.11.000288.

N. Q. Balaban, J. Merrin, R. Chait, L. Kowalik, and S. Leibler. Bacterial persistence as a phenotypic switch. *Science (New York, N.Y.)*, 305(5690):1622–1625, Sept. 2004. ISSN 1095-9203. doi: 10.1126/science.1099390. PMID: 15308767.

S. M. Block. Making light work with optical tweezers. *Nature*, 360(6403):493–495, Dec. 1992. doi: 10.1038/360493a0.

T. P. Burg and S. R. Manalis. Suspended microchannel resonators for biomolecular detection. *Applied Physics Letters*, 83(13):2698, 2003. doi: 10.1063/1.1611625.

T. P. Burg, A. R. Mirza, N. Milovic, C. H. Tsau, G. A. Popescu, J. S. Foster, and S. R. Manalis. Vacuum-Packaged suspended microchannel resonant mass sensor for biomolecular detection. *Journal Of Microelectromechanical Systems*, 15(6):1466–1476, 2006. doi: 10.1109/JMEMS.2006.883568.

T. P. Burg, M. Godin, S. M. Knudsen, W. Shen, G. Carlson, J. S. Foster, K. Babcock, and S. R. Manalis. Weighing of biomolecules, single cells and single nanoparticles in fluid. *Nature*, 446(7139):1066–1069, Apr. 2007. ISSN 0028-0836. doi: 10.1038/nature05741.

D. D. Carlo, L. Y. Wu, and L. P. Lee. Dynamic single cell culture array. *Lab Chip*, 6 (11):1445–1449, Sept. 2006. doi: 10.1039/B605937F.

J. Carmichael, J. B. Mitchell, W. G. DeGraff, J. Gamson, A. F. Gazdar, B. E. Johnson, E. Glatstein, and J. D. Minna. Chemosensitivity testing of human lung cancer cell lines using the MTT assay. *British Journal of Cancer*, 57(6):540–547, June 1988. ISSN 0007-0920. PMID: 2841961 PMCID: 2246465.

J. M. Davies, C. Brownlee, and D. H. Jennings. Electrophysiological evidence for an electrogenic proton pump and the proton symport of glucose in the marine fungus dendryphiella salina. *Journal of Experimental Botany*, 41(4):449 –456, Apr. 1990. doi: 10.1093/jxb/41.4.449.

P. K. Davis, A. Ho, and S. F. Dowdy. Review biological methods for Cell-Cycle synchronization of mammalian cells. *Biotechniques*, 30(6):13221331, 2001.

M. Evander, L. Johansson, T. Lilliehorn, J. Piskur, M. Lindvall, S. Johansson, M. Almqvist, T. Laurell, and J. Nilsson. Noninvasive acoustic cell trapping in a microfluidic perfusion system for online bioassays. *Analytical Chemistry*, 79(7): 2984–2991, Apr. 2007. ISSN 0003-2700. doi: 10.1021/ac061576v. PMID: 17313183.

H. Fiebig, A. Maier, and A. Burger. Clonogenic assay with established human tumour xenografts: correlation of in vitro to in vivo activity as a basis for anticancer drug discovery. *European Journal of Cancer*, 40(6):802–820, Apr. 2004. ISSN 0959-8049. doi: 10.1016/j.ejca.2004.01.009.

C. M. Fillmore and C. Kuperwasser. Human breast cancer cell lines contain stem-like cells that self-renew, give rise to phenotypically diverse progeny and survive chemotherapy. *Breast Cancer Research*, 10(2):R25, Mar. 2008. ISSN 1465-5411. doi: 10.1186/bcr1982.

N. A. P. Franken, H. M. Rodermond, J. Stap, J. Haveman, and C. v. Bree. Clonogenic assay of cells in vitro. *Nature Protocols*, 1(5):2315–2319, Dec. 2006. ISSN 1754-2189. doi: 10.1038/nprot.2006.339.

M. Godin, F. F. Delgado, S. Son, W. H. Grover, A. K. Bryan, A. Tzur, P. Jorgensen, K. Payer, A. D. Grossman, M. W. Kirschner, and S. R. Manalis. Using buoyant mass to measure the growth of single cells. *Nat Meth*, 7(5):387–390, May 2010. ISSN 1548-7091. doi: 10.1038/nmeth.1452.

D. S. Gray, J. L. Tan, J. Voldman, and C. S. Chen. Dielectrophoretic registration of living cells to a microelectrode array (vol 19, pg 771, 2004). *Biosensors Bioelectronics*, 19(12):1765–1774, 2004.

J. M. Irish, N. Kotecha, and G. P. Nolan. Mapping normal and cancer cell signalling networks: towards single-cell proteomics. *Nat Rev Cancer*, 6(2):146–155, Feb. 2006. ISSN 1474-175X. doi: 10.1038/nrc1804.

D. Issadore, T. Franke, K. A. Brown, and R. M. Westervelt. A microfluidic microprocessor: controlling biomimetic containers and cells using hybrid integrated circuit/microfluidic chips. *Lab on a Chip*, 10(21):2937–2943, 2010. doi: 10.1039/C0LC00092B.

R. M. Johann. Cell trapping in microfluidic chips. *Analytical and Bioanalytical Chemistry*, 385(3):408–412, Apr. 2006. ISSN 1618-2642, 1618-2650. doi: 10.1007/s00216-006-0369-6.

M. J. Lang and S. M. Block. Resource letter: LBOT-1: laser-based optical tweezers. *American journal of physics*, 71(3):201–215, Mar. 2003. ISSN 0002-9505. doi: 10.1119/1.1532323. PMID: 16971965 PMCID: 1564163.

D. Longo and J. Hasty. Dynamics of single-cell gene expression. *Molecular Systems Biology*, 2:64, Nov. 2006. ISSN 1744-4292. doi: 10.1038/msb4100110. PMID: 17130866 PMCID: 1682029.

S. R. Manalis, S. C. Minne, A. Atalar, and C. F. Quate. Highspeed atomic force microscopy using an integrated actuator and optical lever detection. *Review of Scientific Instruments*, 67(9):3294–3297, Sept. 1996. ISSN 00346748. doi: doi:10.1063/1.1147410.

M. Mir, Z. Wang, Z. Shen, M. Bednarz, R. Bashir, I. Golding, S. G. Prasanth, and G. Popescu. Optical measurement of cycle-dependent cell growth. *Proceedings of the National Academy of Sciences*, July 2011. doi: 10.1073/pnas.1100506108.

A. Y. Olsson, A. Feber, S. Edwards, R. t. Poele, I. Giddings, S. Merson, and C. S. Cooper. Role of E2F3 expression in modulating cellular proliferation rate in human bladder and prostate cancer cells. *Oncogene*, 26(7):1028–1037, Aug. 2006. ISSN 0950-9232. doi: 10.1038/sj.onc.1209854.

X. S. Ouyang, X. Wang, M. Ling, H. L. Wong, S. W. Tsao, and Y. C. Wong. Id-1 stimulates serum independent prostate cancer cell proliferation through inactivation of p16(INK4a)/pRB pathway. *Carcinogenesis*, 23(5):721–725, May 2002. ISSN 0143-3334. PMID: 12016143.

G. Popescu, Y. Park, N. Lue, C. Best-Popescu, L. Deflores, R. R. Dasari, M. S. Feld, and K. Badizadegan. Optical imaging of cell mass and growth dynamics. *American Journal of Physiology - Cell Physiology*, 295(2):C538 –C544, 2008. doi: 10.1152/ajpcell.00121.2008.

J. Reed, J. Chun, T. Zangle, S. Kalim, J. Hong, S. Pefley, X. Zheng, J. Gimzewski, and M. Teitell. Rapid, massively parallel Single-Cell drug response measurements via live cell interferometry. *Biophysical Journal*, 101(5):1025–1031, Sept. 2011. ISSN 0006-3495. doi: 10.1016/j.bpj.2011.07.022.

T. Reya, S. J. Morrison, M. F. Clarke, and I. L. Weissman. Stem cells, cancer, and cancer stem cells. *Nature*, 414(6859):105–111, Nov. 2001. ISSN 0028-0836. doi: 10.1038/35102167. PMID: 11689955.

A. Rohrbach and E. H. K. Stelzer. Trapping forces, force constants, and potential depths for dielectric spheres in the presence of spherical aberrations. *Applied Optics*, 41(13):2494–2507, May 2002. doi: 10.1364/AO.41.002494.

J. C. Romijn, C. F. Verkoelen, and F. H. Schroeder. Application of the MTT assay to human prostate cancer cell lines in vitro: establishment of test conditions and assessment of hormone-stimulated growth and drug-induced cytostatic and cytotoxic effects. *The Prostate*, 12(1):99–110, 1988. ISSN 0270-4137. PMID: 3126493.

S. L. Spencer, S. Gaudet, J. G. Albeck, J. M. Burke, and P. K. Sorger. Non-genetic origins of cell-to-cell variability in TRAIL-induced apoptosis. *Nature*, 459(7245): 428–432, Apr. 2009. ISSN 0028-0836. doi: 10.1038/nature08012.

D. G. Spiller, C. D. Wood, D. A. Rand, and M. R. H. White. Measurement of single-cell dynamics. *Nature*, 465(7299):736–745, June 2010. ISSN 0028-0836. doi: 10.1038/nature09232.

K. Svoboda and S. M. Block. Biological applications of optical forces. *Annual Review of Biophysics and Biomolecular Structure*, 23:247–285, 1994. ISSN 1056-8700. doi: 10.1146/annurev.bb.23.060194.001335. PMID: 7919782.

S. D. Talia, J. M. Skotheim, J. M. Bean, E. D. Siggia, and F. R. Cross. The effects of molecular noise and size control on variability in the budding yeast cell cycle. *Nature*, 448(7156):947–951, 2007. ISSN 0028-0836. doi: 10.1038/nature06072.

A. Valero, F. Merino, F. Wolbers, R. Luttge, I. Vermes, H. Andersson, and A. van den Berg. Apoptotic cell death dynamics of HL60 cells studied using a microfluidic cell trap device. *Lab on a Chip*, 5(1):49–55, Jan. 2005. ISSN 1473-0197. doi: 10.1039/b415813j. PMID: 15616740.

M. Wang, C. Ozkan, R. Flynn, A. Birkbeck, and S. Esener. Optical manipulation of objects and biological cells in micro uidic devices. *Electrical Engineering*, 5(1): 61–67, 2003.

P. Wang, S. M. Henning, and D. Heber. Limitations of MTT and MTS-Based assays for measurement of antiproliferative activity of green tea polyphenols. *PLoS ONE*, 5(4):e10202, Apr. 2010. doi: 10.1371/journal.pone.0010202.

A. A. Werdich, E. A. Lima, B. Ivanov, I. Ges, M. E. Anderson, J. P. Wikswo, and F. J. Baudenbacher. A microfluidic device to confine a single cardiac myocyte in a sub-nanoliter volume on planar microelectrodes for extracellular potential recordings. *Lab on a Chip*, 4(4):357–362, Aug. 2004. ISSN 1473-0197. doi: 10.1039/b315648f. PMID: 15269804.

A. R. Wheeler, W. R. Throndset, R. J. Whelan, A. M. Leach, R. N. Zare, Y. H. Liao, K. Farrell, I. D. Manger, and A. Daridon. Microfluidic device for Single-Cell analysis. *Anal. Chem.*, 75(14):3581–3586, 2003. ISSN 0003-2700. doi: 10.1021/ac0340758.

R. N. Zare and S. Kim. Microfluidic platforms for single-cell analysis. *Annual Review of Biomedical Engineering*, 12:187–201, Aug. 2010. ISSN 1545-4274. doi: 10.1146/annurev-bioeng-070909-105238. PMID: 20433347.

1.4 Figures

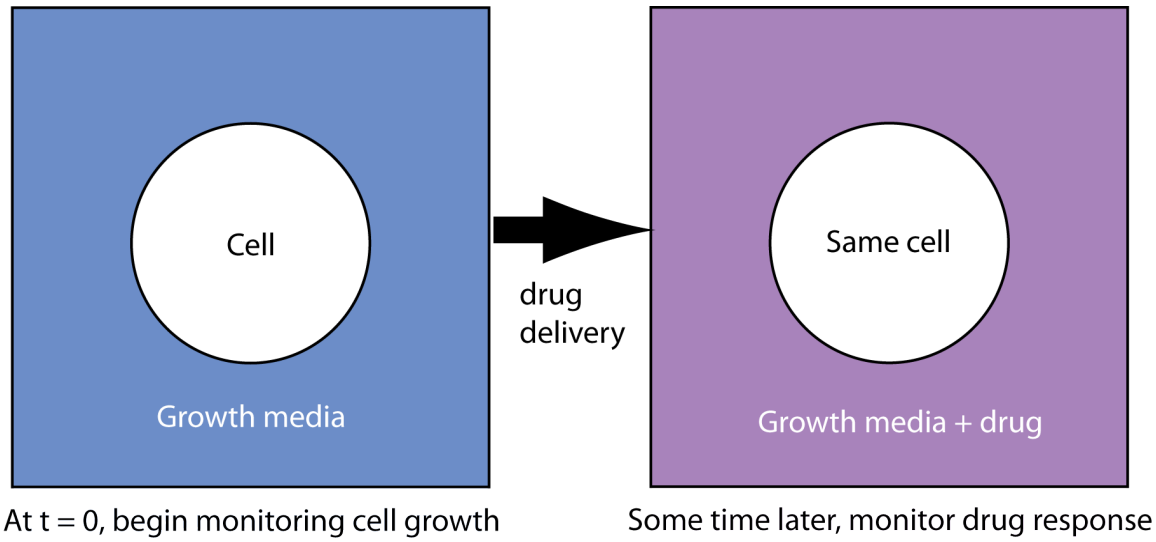

Figure 1-1: In order to fully understand a mammalian cell's response to a therapeutic intervention, one must first monitor the cell in growth media to obtain its normal growth characteristics. At some arbitrary time, the same cell is treated with a particular drug and monitored again thereafter. Even amongst a seemingly homogeneous population, cell-to-cell variabilities may yield widely different results at the individual cell. Having the ability to distinguish which cells are not growing well prior to the perturbation is essential. The central theme of this thesis is the development and application of an instrument to achieve such measurements.

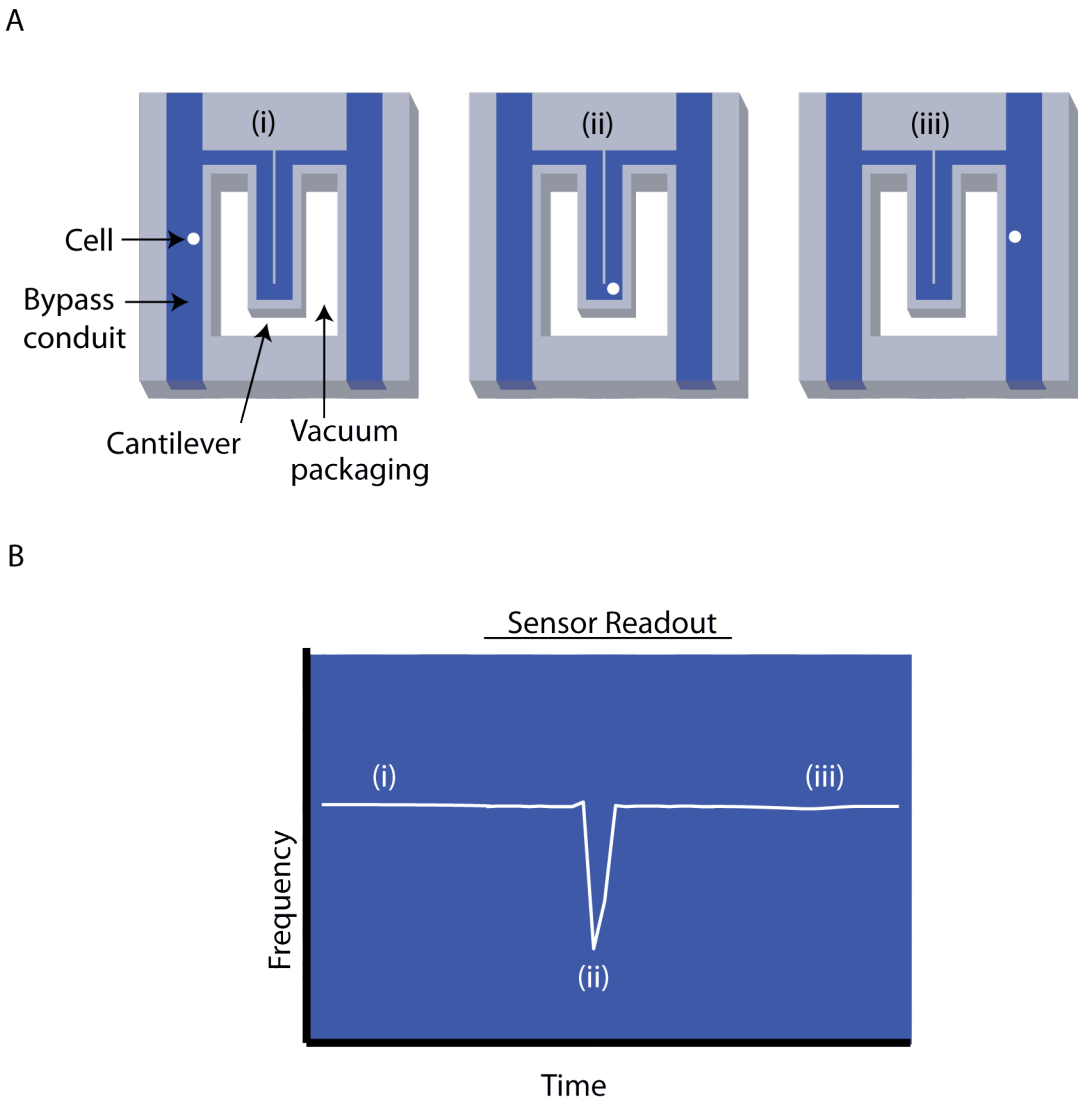

Figure 1-2: The mass sensing region of the suspended microchannel resonator (SMR) consists of a vacuum-packaged cantilever with an embedded microfluidic channel. (A) A series of cartoons (i-iii) illustrates a cell moving from the first bypass conduit of the device through the cantilever and into the second bypass conduit. (B) An example readout demonstrating what the frequency of the mass sensor would look like while the cell is at various positions of the device (i-iii).

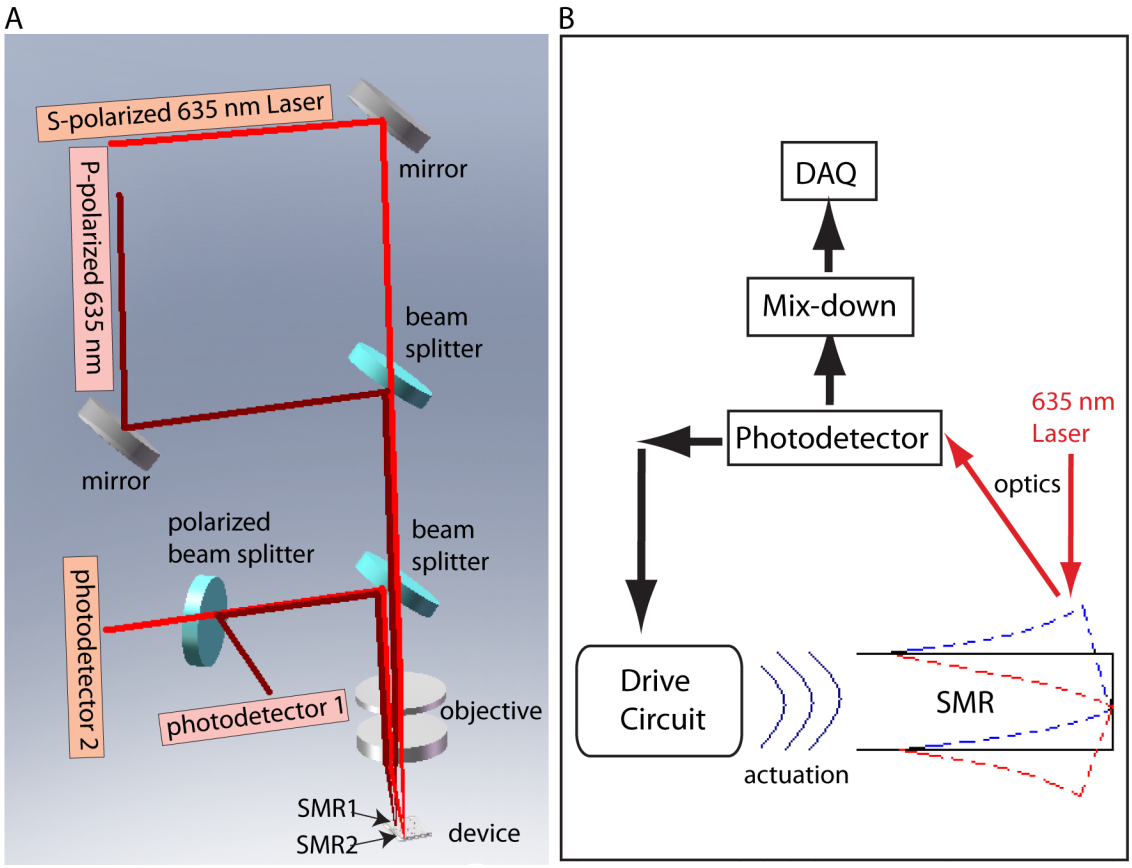

Figure 1-3: The oscillation of the SMR is amplified via a positive feedback loop consisting of optics and electronics. (A) An optical lever system much like that of the atomic force microscope (AFM) is used to detect the oscillation of the SMR. A 635 nm (red) laser is focused down to a diffraction-limited spot on the cantilever. A periodic focusing and defocusing of the light is projected onto a photodetector and is converted to a voltage signal. Each device is equipped with two fully functioning SMRs. The optics shown here take advantage of s and p polarization to enable dual readout. (B) The voltage signal, a sinusoid with respect to time, is amplified and phase shifted at the drive circuit. The SMR can be actuated electrostatically via electrodes or mechanically via a piezoelectric crystal. In parallel, the photodetector signal is mixed down to a lower frequency and sent to a data acquisition card.

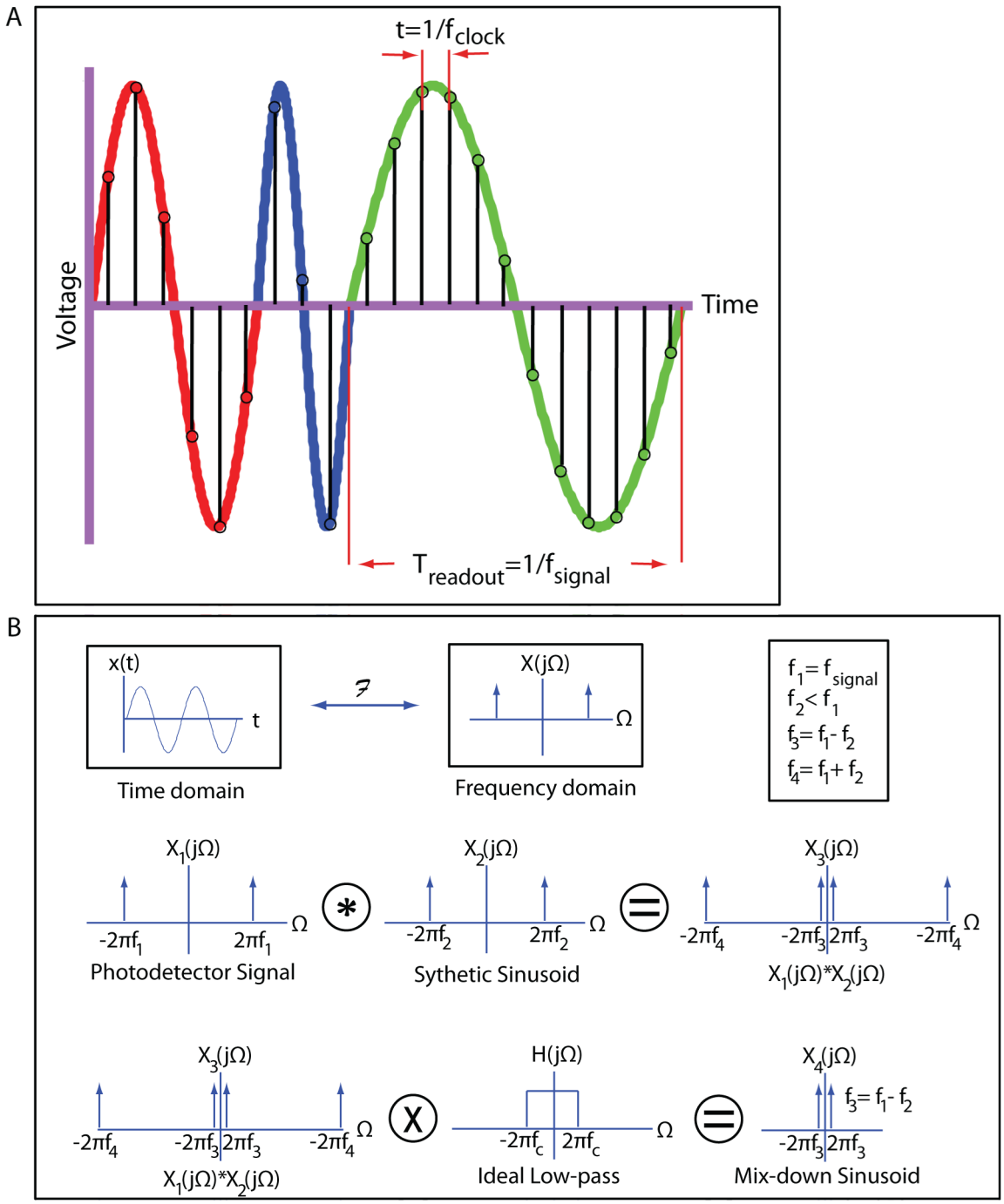

Figure 1-4: (A) The DAQ, sampling at f_{clock}, can acquire more samples per period if the frequency of the input signal is lowered. More samples result in lower noise per readout. However, if the frequency of the signal is too low, the interval between each readout would be too long to resolve fast events such as cell transits. (B) Indicated here is an idealized scheme by which the photodetector signal is mixed down. The result is a sinusoid with a frequency equal to the difference between that of the photodetector signal and that of the synthetic sinusoid. We have found that a mixed-down frequency centered about 1kHz is at an optimal trade-off between noise and readout speed.

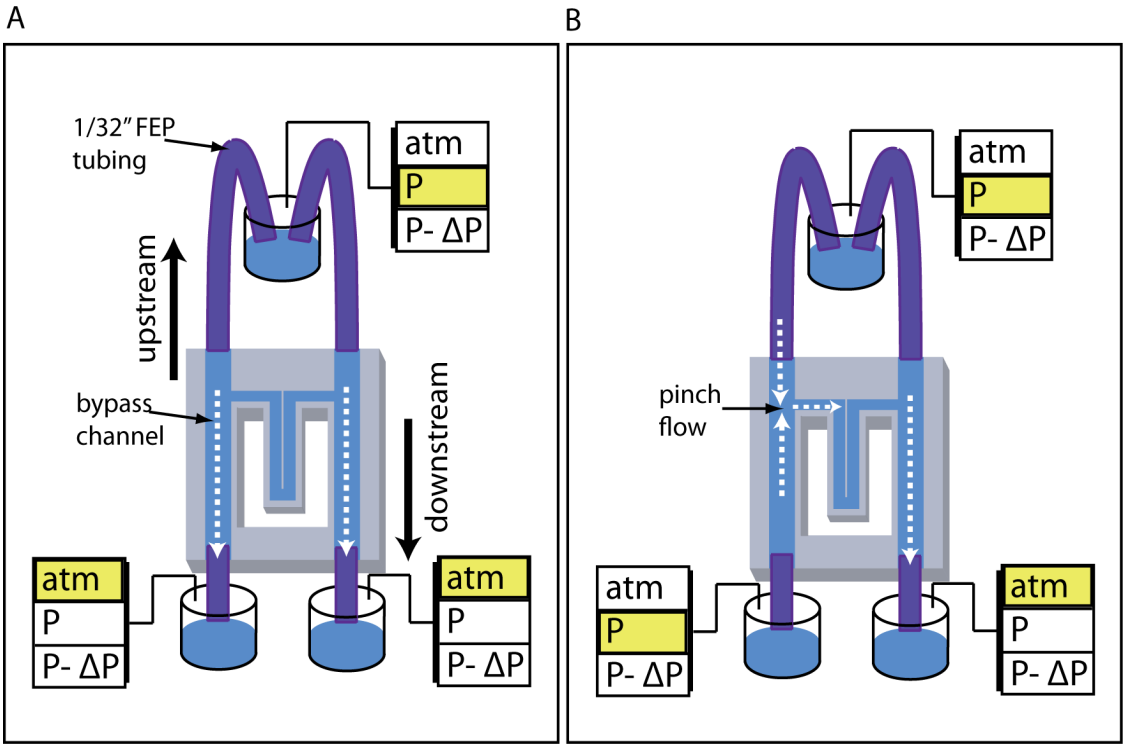

Figure 1-5: Fluid is driven by pressure through the SMR device. A combination of valves and pressure regulators allow each vial (both downstream and upstream) to multiplex between atmosphere, P, and P-ΔP. The latter two are given in gauge pressures. (A) This configuration is commonly used for priming the device. The system flushes fluid from a single upstream vial through all tubings and bypass channels. (B) In this mode, the system forces all the fluid in one bypass to pinch flow through the SMR into the second bypass. The downstream waste vial on the second bypass could either be at P-ΔP or at atmosphere depending on the desired magnitude of flow rate.

Chapter 2

Cell capture against flow: implementing an optical trap

Chapter 2

Cell capture against flow: implementing optical tweezers

2.1 Motivation

By combining the mass-sensing capabilities of the SMR with a single laser beam optical trap (Figure 2-1A,B), also known as optical tweezers, we can capitalize on decades of research manifesting the deft for capturing, probing, and manipulating micron-sized objects with radiation pressure (Block, 1992, 1995; Lang and Block, 2003; Wright et al., 1989). Utilizing forces on the order of 1-100 pN (Ashkin et al., 1986; Huang et al., 2009), Ashkin et al. (1987) studied the proliferation of bacteria and yeast cells while dragging individual cells up to a velocity of 500 μm s^{-1} and 100 μm s^{-1} respectively. This demonstrated that cell viability can be maintained even after hours of laser exposure. Optical tweezers have also been used to probe viruses (Ashkin and Dziedzic, 1987), understand cell movement (Block et al., 1989; Takahashi et al., 2003), and perform force spectroscopy on single molecules (Lang et al., 2002, 2004; Neuman and Nagy, 2008).

In order to harness the power of the optical force within the SMR, we must first examine the physical constraints of the device. Since a cell is immobilized against hydrodynamic drag, understanding the flow rates and the fluidic profile within the cantilever provides us with an approximate magnitude of force required to keep the

cell captured. Understanding the optical characteristics of silicon allows us to not only maximize the transmission of light through the cantilever but also to minimize heating from laser absorption. The considerations provided here, however, have implications beyond just the optical trap implementation. They are central in the development of an optical imaging system as well as in the design of cell traps for later generations of the instrument.

2.2 Design considerations

2.2.1 Fluid dynamics

In order to solve for the velocity profile in the rectangular channels of the SMR (Figure 2-2A), we employed the Navier-Stokes equation in Cartesian coordinates. The flow of an incompressible fluid through the hollow cantilever is steady and fully developed since the fluid velocity does not vary in the axial direction, $\frac{dV_z}{dz} = 0$, or in time, $\frac{d\vec{V}}{dt} = 0$. It is laminar as expected of a fluid in the low Reynold's number regime. Furthermore, without any rotational or swirling component in the velocity, a fully developed flow can only be unidirectional ($V_x = 0$ and $V_y = 0$). Under these conditions, the inertial effects on flow are neglected in the microfluidic channel (Whitesides, 2006). Since gravitational effects are assumed negligible for this calculation, the Navier-Stokes equation reduces to the Poisson's equation:

$$\frac{1}{\mu}\frac{dP}{dz} = \left[\frac{d^2V_z}{dx^2} + \frac{d^2V_z}{dy^2}\right]$$

where P is the pressure drop across the channel, μ is the viscosity of the fluid, and V_z is the fluid velocity in the axial direction. Using harmonic analysis (see appendix A), we found that the solution of the Poisson's equation is in the form

$$V_z(x,y) = \sum_{k=odd}\sum_{l=odd} a_{k,l} cos\left(\frac{k\pi}{L_x}x\right) cos\left(\frac{l\pi}{L_y}y\right) \tag{2.1}$$

where $a_{k,l}$ are the Fourier series coefficients, L_x is the width of the channel, and L_y is the height of the channel. The coefficients of the sine series equal zero as a no-slip boundary condition is imposed on the walls. At a low flow rate equivalent to half of the entire SMR volume per second, the parabolic flow reaches a maximum velocity of 482 μm s^{-1} and 717 μm s^{-1} near the center of an 8x8 μm and a 15x20 μm channel respectively. At these velocities, the Reynolds number (Re) is $\sim$0.01, confirming that fluid movement is viscous-dominated inside the SMR. The velocity profiles for both types of channels are shown in Figure 2-2B,C.

We estimated the drag force on a cell (with a radius r) immobilized in the midst of the channel by substituting an average fluid velocity into Stoke's law:

$$F_{avg} = 6\pi\mu r \left[\frac{1}{A} \int \int_A V_z(x,y)\, dxdy \right] \tag{2.2}$$

Table 2-1 lists the average optical forces required to immobilize objects traveling through the SMR with various flow velocities, presented as transit durations and pressure drops across the channel. We found that for a trap to be effective in capturing a mammalian cell, it must be able to generate approximately 30 pN within the embedded channels of the cantilever. Optical tweezers can typically produce a force of $\sim$1 pN per mW (Farinato and Dubin, 1999). Based on this prediction, we estimated that $\sim$30 mW of laser power at the specimen plane is required.

2.2.2 Particle oscillation

In viscous dominated flow, changes in fluid velocity profile in response to an applied pressure or a surface movement will occur instantaneously (Deen, 1998). For example, if the pressure differential across a conduit is suddenly removed, the flow will not slow to a stop but will rather cease immediately. An object that is vanishingly small compared to the channel dimensions and has a negligible mass typically follows the streamlines exactly even when the velocity fields change. However, as the object becomes larger, its mass inevitably increases precluding inertial effects from being ignored. In response to a step change in velocity field, a drag force will be imposed

on the object until its velocity matches that of the streamlines once again.

From the perspective of an object within the SMR, the oscillation of the cantilever consistently changes the fluid velocity profile in the y-direction (Figure 2-1A). For an object sizable enough such that inertial effects are nontrivial, its velocity and the fluid velocity are at a constant mismatch. We investigated the resulting differences in displacement between the object and the fluid so that we might understand how this oscillation affects the immobilization of a cell.

The velocity of the cantilever and the fluid within is represented as the time derivative of the cantilever oscillation

$$v(t) = \frac{dy(t)}{dt} = -A\omega sin(\omega t)$$

where A is the amplitude of oscillation, ω is the frequency of oscillation, and $y(t)$ is the cantilever displacement. Applying Stoke's law, we found that the drag force on an object is depicted by the first order differential equation

$$F = \left[\rho\frac{4}{3}\pi r^3\right]\frac{dv_p}{dt} = 6\pi\mu r\big[-A\omega sin(\omega t) - v_p\big] \tag{2.3}$$

where v_p, $\rho\frac{4}{3}\pi r^3$, and r are the object's velocity, buoyant mass (m_b), and radius respectively. The parameter ρ is the density difference between the object and the surrounding fluid medium. In appendix A, we determined that the solution to (2.3) is

$$v_p = -\frac{\Phi A\omega^2}{\omega^2+\Phi^2}exp(-\Phi t) + \frac{\Phi A\omega^2}{\omega^2+\Phi^2}cos(\omega t) - \frac{\Phi^2 A\omega}{\omega^2+\Phi^2}sin(\omega t) \tag{2.4}$$

where $\Phi = \frac{6\mu r}{m_b}$, a constant that relates the fluid viscosity to the object's buoyant mass. To find the object's displacement (y_p), we integrated v_p with respect to time and evaluated the boundary condition of $y_p = A$ at $t = 0$.

$$y_p = \frac{A}{\omega^2+\Phi^2}\left[\omega^2 exp(-\Phi t) + \Phi\omega sin(\omega t) + \Phi^2 cos(\omega t)\right] \tag{2.5}$$

Table 2-2 lists the steady state amplitude of oscillation for four spherical objects

each with a density similar to that of a cell ($\rho_{cell} = 1.1\ g\ cm^{-3}$) but with dramatically different radii, $r\ \epsilon\ \{100\ nm,\ 1\ \mu m,\ 5\ \mu m\ \ 10\ \mu m\}$. We assumed that the cantilever oscillates with a maximum amplitude of $\sim$100 nm at a frequency of 200kHz and that the fluid within has a viscosity of 0.89 centipoise. The results show that objects with a radius less than 1 μm experience negligible resistance to displacement and follow the oscillation of the cantilever almost exactly. However, for an object larger than 1 μm, inertial effects from its buoyant mass become substantial, and its movements become more sluggish with increasing size.

One interesting observation to note is that the oscillation of the cantilever hydrodynamically focuses the object at the equilibrium point, or the position at which the cantilever's displacement, $y(t)$, is 0. As time increases, the exponential term in (2.5) becomes negligible and the object's oscillation consists purely of two sinusoids with no position offset. For example, if a 10 μm object were initially displaced by 100nm in the y-direction, it would travel that length to center its oscillation about the equilibrium point despite only having a steady state oscillation amplitude of $\sim$31.5 nm. A caveat to take into consideration, however, is that for an object with a diameter on the order of the channel's height, its resistance to movement is, in fact, mitigated by the higher resistance of the fluid layers closer to the walls. Although both the 5 μm and the 10 μm objects will in reality experience a larger displacement than estimated because of this effect, we can conclude from this analysis that inertia will confine micron-sized objects such as cells to oscillation amplitudes well within a few tens of nanometers. Vascillations of this magnitude are unlikely to eject the object from a stable trap formed by optical tweezers.

2.2.3 Heat transport

Two coherent light sources, the frequency readout laser and the optical tweezers, are each focused down to a diffraction-limited spot either on the surface of or within the cantilever. Absorption of light can potentially heat the fluid inside the embedded channel to a temperature incapable of sustaining cell survival. To estimate the magnitude of heating, we must first consider the optical properties of the cantilever. Silicon,

the primary material of the SMR, has a low transmittance and a high absorbance for light throughout the visible and part of the IR spectrum. The percentage of transmittance, reflectance, and absorbance of light passing through the cantilever (Figure 2-3A) is determined based on the data provided by Aspens (1988); Hull (1999).

To estimate heat transfer, we employed a lumped-element circuit model (Figure 2-3B) where the fluid and silicon layers are modeled as resistances in parallel. Heating is assumed to take place at one end (the cantilever apex), and the other end (the base) is assumed to be at an infinite heat sink due to a large device to cantilever size ratio. Writing the equation for the circuit model, we obtained

$$\Delta T = P(R_{si}||R_{water}) = P\left[\frac{R_{si}R_{water}}{R_{si}+R_{water}}\right] \tag{2.6}$$

where P is the laser power that is absorbed by the material. The thermal resistance, like electrical resistance, is defined as

$$R = \frac{1}{\kappa}\frac{L}{A} \tag{2.7}$$

where κ is the conductivity, L is the length of the resistor, and A is the cross-sectional area. We substitute equation (2.7) into (2.6) and get

$$\Delta T = P\left[\frac{L}{A_{si}\kappa_{si}+A_{water}\kappa_{water}}\right] \tag{2.8}$$

The κ_{water}=0.6 W K^{-1} m^{-1} and κ_{si}=150 W K^{-1} m^{-1}. Since both the cross sectional area and the heat conductivity of silicon is larger than that of water, the contribution of the fluid layer can effectively be neglected ($A_{si}\kappa_{si} >> A_{water}\kappa_{water}$).

To get an upper bound on temperature increase, we computed the heat transfer for the 8x8 μm channel which has a higher thermal resistance than its counterpart 15x20 μm channel. For the 635 nm readout laser, the power is attenuated down to $\sim$50 μW before reaching the SMR. According to Figure 2-3A, the absorbance of silicon at 635 nm is $\sim$65%. Evaluating (2.8), we found that the temperature increase due to the readout laser is less than 1 K. We used the same technique to estimate

the heat transfer due to the optical tweezers. Since the cantilever transmits slightly more than 50% of light in the near infrared spectrum, we determined that 100 mW of laser power entering the SMR can provide more than the estimated required force of 30 pN at the specimen plane. Figure 2-3C summarizes the temperature increase for a range of near infrared wavelengths. We found that at 1064 nm, the cantilever heating is at most 13.75 K. Since the clamp holding the SMR device is thermally controlled, we can adjust for a temperature increase on this order simply by cooling.

In our lumped-element circuit model, we assumed that fluid convection does not affect the temperature of the cantilever. To assess the validity of this assumption, we calculated the time constant for heat conduction

$$\tau_d = d^2 \frac{\sigma C}{\kappa_{water}} \tag{2.9}$$

where d, σ, and C are thickness, density, and heat capacity of the fluid layer. For a thickness of 8 μm, τ_d is equal to 446 μs. At this time scale, the fluid traverses less than 2% of the entire cantilever length even when moving at a high flow rate of twenty times the SMR volume per second, or equivalent to an average velocity of 9.2x10^3 μm s^{-1}. From this result, we can conclude that the effects of convection is minimal and that for low to moderately high flow rates, the fluid is in thermal equilibrium with the channel walls.

2.3 Optical trap prototype

2.3.1 Microscope objective and laser

To achieve strong optical gradient force requires not only sufficient laser power but also a tightly focused spot at the trap position. This necessitates a microscope objective with a high numerical aperture (NA) which typically means that the working distance is short. The SMR, however, is encased on the bottom side by 0.6-1mm of Pyrex and vacuum combined. Therefore, the objective must have a long working distance such that the laser may penetrate multiple layers before focusing on the specimen plane.

The use of oil-immersion to achieve a higher NA is precluded by the vacuum which limits the maximum effective NA of any objective at unity. Light entering this region from beyond the critical angle will experience total internal reflection. Additionally, the thick Pyrex creates aberrations at the focus by introducing phase shifts in the axial direction of the trap (Rohrbach and Stelzer, 2002). Because of its large working distance (0.95-1.3 mm) and its high NA (0.85), the CFI L Plan EPI CRB 100x Nikon objective is chosen. It also has a variable cover-slip thickness correction (0.6-1.3 mm) which ameliorates the aberrations from the Pyrex to achieve a better focus.

To provide sufficient laser power while avoiding excessive cantilever heating, we selected a continuous wave IR Laser at 1064nm (Ventus IR from Laser Quantum) which has a maximum output of 3W. At this wavelength, the cantilever absorbs less than 3% and transmits more than 50%. Accounting for the main components of the optical tweezers (mirrors, lenses, beam splitters, objective, Pyrex, silicon), we found that ∼80% of the initial laser power is dissipated even before the light reaches the fluid layer. If we assume a fiber coupling efficiency of 50%, then the maximum amount of power we can attain at the specimen plane is ∼300mW, or 10 times the estimated amount required to immobilize a mammalian cell.

2.3.2 SMR reimplementation

Both the optical tweezers and the readout laser must have access to the cantilever. To facilitate the process of alignment, we decoupled the two optics. Because the optical trap setup also contain an imaging system, it is comparatively bulkier than the frequency detection optics. We redesigned the frequency detection so that the entire contraption (laser, optics, and photodetector electronics) can be suspended from above allowing it access to the cantilever from the top side. Figure 2-4A shows the ray tracing diagram for the optical lever readout. In order to minimize weight, we simplified the optics down to a beam splitter and a customized objective (meniscus lens and achromatic doublet) with an effective focal length (EFL) of 50 mm. The beam splitter allows 50% of the incident collimated laser to proceed and focus onto the cantilever through the objective. It also allows 50% of the collimated rays returning

from the cantilever to be reflected onto the photodetector. Rather than using mirrors to steer the beam, we mounted the 635 nm laser directly onto a tilting stage. By rotating the position of the laser, we can pinpoint the position of the diffraction-limited spot to the apex of the SMR. The photodetector circuit is assembled on a cage plate attached to a kinematic mount so that it may be clamped onto the damped post which suspends the rest of the frequency detection optics.

2.3.3 Optical tweezers and imaging system implementation

The ray tracing diagram for the optical tweezers is provided in Figure 2-4A. The 1064 nm laser is fiber coupled and attached to the optics via an FC connector. Two mirrors in series serve as the course adjust for aligning the laser through the center (z-axis) of the microscope objective. A pair of lenses (focal lengths: -40 mm and 100 mm) is positioned in a Galilean telescope arrangement to achieve a beam expansion ratio of 1.67:1. The expansion allows the laser to overfill the back aperture of the microscope objective enabling the trap to take advantage of the maximum NA. While the distance between the beam expansion lenses can be finely adjusted to control the focal point of the laser in the axial direction (z-axis), the center point of the second lens with respect to the first lens can also be adjusted to control the lateral position (x-y direction) of the trap in the specimen plane. After the expansion, the laser is reflected by a broadband IR beam splitter (45% reflection, 55% transmission) and is directed by a 45° mirror into the back aperture of the objective.

In order to visualize the inside of the cantilever, we implemented an imaging system that utilizes epi-illumination (Figure 2-4A). For illumination, we used a monochromatic source at 940 nm, a wavelength with sufficient transmission through silicon while distinct enough such that the trapping laser does not interfere with the image. Light from a 1W diode is collimated and then injected into the system via a broadband IR beam splitter. The collimated light is focused onto the back aperture of the objective through a 200 mm tube lens and is again collimated at the specimen plane to avoid forming a light bulb image within the cantilever. Reflected light carrying the image from within the SMR is collimated through the objective and is then focused

by the 200 mm tube lens onto the CCD camera. A 1 μm short-pass filter allows >80% transmission of the image (at 940 nm) to the camera and attenuates ∼99% of the reflected light from the 1064 nm laser.

The optical portion of the instrument, excluding the lasers and the photodetector mount, is shown in Figure 2-4B. For stability and ease of alignment, all lenses and mirrors are mounted on a cage system. The SMR device is enclosed within a temperature-controlled clamp consisting of a top copper and a bottom aluminum. The clamp is mounted on a 3-axis stage enabling the quick alignment of a new or a different SMR device without having to readjust the configurations of the optical tweezers and the frequency readout optics.

2.4 Trap assessment and discussions

2.4.1 Trap stiffness

Much like a mass on a spring, any object held by optical tweezers will experience a Hookean restoring force for small displacements away from the trap center. Thus stiffness, in units of a spring constant, is a conventional metric for measuring the strength of optical tweezers. To make this assessment, we performed the Stokes drag calibration in which the restoring force of the trap was equated to the hydrodynamic drag applied by a fluid velocity v on a trapped object with a radius r (Appleyard et al., 2007).

$$F = kx = 6\pi\mu rv \tag{2.10}$$

To determine the stiffness coefficient k, we measured x, the displacement of an object away from the trap center, for various fluid velocities. Since the relationship between x and v is linear, we fitted a first order polynomial (x=Mv+b) through the data points and extracted the slope M. The stiffness was then calculated from $k = \frac{6\pi\mu r}{M}$. In place of the SMR device, we used a glass flow cell mounted on an automated motorized stage. Following the capture of a 3.2 μm polystyrene bead by the optical tweezer, the stage executed the following program: wait, apply a positive

velocity of a known magnitude, wait, and apply a negative velocity of the same magnitude. The duration of each step lasted only for a few seconds. When the stage applied a velocity on the flow cell, the fluid within would move against the object and displace it from the center of the trap. The entire sequence was recorded into file by a video camera on the imaging system. Each frame of the video was analyzed by a particle tracking algorithm that calculated the bead's position based on a weighted centroid of the pixels. A least squares fit of all the positions measured was used to determine the displacement of the bead from the center of the optical trap (Figure 2-5A).

The results of the displacement versus fluid velocity calibration is shown in Figure 2-5B. The stiffness of our trap (with 50 mW of laser power at the specimen plane) was 0.0362 $pNnm^{-1}$. Appleyard et al. (2007) reported a similar stiffness value but for 30 mW of laser power. We attributed this discrepancy to the difference in the microscope objectives of the two instruments. Whereas Appleyard et al. (2007) used a 1.25NA oil immersion objective, we required one with a long working distance $\sim$1 mm which limited the NA to 0.85. Having less NA meant that there was a higher proportion of low angle incident rays (scattering force) than there was of the wide angle incident rays (gradient force) in our trap. Although both the scattering and the gradient forces were necessary for a dielectric object to be captured by optical tweezers, an increased amount of scattering would result in a weaker trap.

To obtain the maximum attainable optical force on a captured 3.2 μm object, the motorized stage was programmed to sweep across a number of velocity step increases. We found that a step increase of 210 $\mu m\ s^{-1}$ was the fastest fluid velocity for which the bead would still remain trapped. Evaluating this in (2.10), we concluded that the maximum attainable optical force was 5.6 pN which was similar to the calculated value from table 2-1: a 3.2 μm object transiting the entire length of the SMR in 2 seconds would require $\sim$6.1 pN to immobilize.

2.4.2 Conclusions

Using laser powers up to 100 mW at the specimen plane, or three times the estimated amount required, we tried to trap various micron sized objects traveling through the SMR. However, we were unable to form a stable trap inside the cantilever regardless of the object's dimension or shape. Despite the optical tweezer's ability to generate forces in a glass flow cell that rivaled the hydrodynamic drag within the SMR, the trap was severely weakened by interference when positioned inside the cantilever. The top silicon wall, only a few microns away from the focus, reflected and scattered the laser resulting in the destabilization of the optical tweezers. In our attempts to capture an object within the SMR, we leveraged flow rates approaching the lower limits achievable by the pressure regulators. Bulk flow through the bypass channels were already too slow for any appreciable fluid exchange to occur. Thus, even if we could optically trap an object by further reducing the transit velocity, doing so would not be practical. Transient pressure instabilities from flow rate increase during drug delivery would suffice to remove a trapped object from within the cantilever. In the end, the SMR device which imposed geometric restrictions on the selection of a high NA microscope objective also limited the laser's ability to form a tightly focused spot, one that was free of distortion from interference. Both of these factors synergistically resulted in a weak or unstable trap.

Cell viability considerations regarding prolonged laser exposure on a cell has directed us to explore alternatives. Liu et al. (1996) reported that a 1064 nm laser at 88 mW will exert substantial damage on mammalian cells if the exposure is for more than 5 minutes. In order to monitor long-term cellular growth dynamics and response to drugs, the SMR must be able to weigh a single cell on the times scale of hours. The idea of mechanical traps came about originally as a method to assist optical tweezers. A cell is initially captured optically against flow and guided into a dock. Thereafter, the laser can be turned off, and the dock will hold the cell in place during the drug delivery process. In this scheme, the exchange can occur at high flow rates because the cell is unlikely to leave its confinement. As the possibility

of optically immobilizing a cell against flow within the SMR began to wane, mass sensors with mechanical traps became its own method for capturing and monitoring cells.

2.5 References

D. C. Appleyard, K. Y. Vandermeulen, H. Lee, and M. J. Lang. Optical trapping for undergraduates. *American Journal of Physics*, 75(1):5, 2007. ISSN 00029505. doi: 10.1119/1.2366734.

A. Ashkin and J. M. Dziedzic. Optical trapping and manipulation of viruses and bacteria. *Science (New York, N.Y.)*, 235(4795):1517–1520, Mar. 1987. ISSN 0036-8075. PMID: 3547653.

A. Ashkin, J. M. Dziedzic, J. E. Bjorkholm, and S. Chu. Observation of a single-beam gradient force optical trap for dielectric particles. *Optics Letters*, 11(5):288–290, May 1986. doi: 10.1364/OL.11.000288.

A. Ashkin, J. M. Dziedzic, and T. Yamane. Optical trapping and manipulation of single cells using infrared laser beams. *Nature*, 330(6150):769–771, Dec. 1987. doi: 10.1038/330769a0.

D. Aspens. *Properties of Silicon*. INSPEC, IET, London, UK, 1988.

S. M. Block. Making light work with optical tweezers. *Nature*, 360(6403):493–495, Dec. 1992. doi: 10.1038/360493a0.

S. M. Block. Nanometres and piconewtons: the macromolecular mechanics of kinesin. *Trends in Cell Biology*, 5(4):169–175, Apr. 1995. ISSN 0962-8924. PMID: 14732153.

S. M. Block, D. F. Blair, and H. C. Berg. Compliance of bacterial flagella measured with optical tweezers. *Nature*, 338(6215):514–518, Apr. 1989. doi: 10.1038/338514a0.

W. M. Deen. *Analysis of transport phenomena*. Oxford University Press, Mar. 1998. ISBN 9780195084948.

R. S. Farinato and P. Dubin. *Colloid-polymer interactions: from fundamentals to practice*. Wiley, New York, June 1999. ISBN 9780471243168.

Y. Huang, J. Wan, M. Cheng, Z. Zhang, S. M. Jhiang, and C. Menq. Three-axis rapid steering of optically propelled micro/nanoparticles. *Review of Scientific Instruments*, 80(6):063107–063107–8, June 2009. ISSN 00346748. doi: doi:10.1063/1.3156838.

R. Hull. *Properties of crystalline silicon*. IET, 1999. ISBN 9780852969335.

M. J. Lang and S. M. Block. Resource letter: LBOT-1: laser-based optical tweezers. *American journal of physics*, 71(3):201–215, Mar. 2003. ISSN 0002-9505. doi: 10.1119/1.1532323. PMID: 16971965 PMCID: 1564163.

M. J. Lang, C. L. Asbury, J. W. Shaevitz, and S. M. Block. An automated Two-Dimensional optical force clamp for single molecule studies. *Biophysical Journal*, 83(1):491–501, July 2002. ISSN 0006-3495. doi: 10.1016/S0006-3495(02)75185-0.

M. J. Lang, P. M. Fordyce, A. M. Engh, K. C. Neuman, and S. M. Block. Simultaneous, coincident optical trapping and Single-Molecule fluorescence. *Nature methods*, 1(2):133–139, Nov. 2004. ISSN 1548-7091. doi: 10.1038/nmeth714. PMID: 15782176 PMCID: 1483847.

Y. Liu, G. J. Sonek, M. W. Berns, and B. J. Tromberg. Physiological monitoring of optically trapped cells: assessing the effects of confinement by 1064-nm laser tweezers using microfluorometry. *Biophysical Journal*, 71(4):2158–2167, Oct. 1996. ISSN 0006-3495. PMID: 8889192 PMCID: 1233684.

K. C. Neuman and A. Nagy. Single-molecule force spectroscopy: optical tweezers, magnetic tweezers and atomic force microscopy. *Nat Meth*, 5(6):491–505, June 2008. ISSN 1548-7091. doi: 10.1038/nmeth.1218.

A. Rohrbach and E. H. K. Stelzer. Trapping forces, force constants, and potential depths for dielectric spheres in the presence of spherical aberrations. *Applied Optics*, 41(13):2494–2507, May 2002. doi: 10.1364/AO.41.002494.

F. Takahashi, Y. Higashino, and H. Miyata. Probing the cell peripheral movements by optical trapping technique. *Biophysical Journal*, 84(4):2664–2670, Apr. 2003. ISSN 0006-3495. PMID: 12668475 PMCID: 1302833.

G. M. Whitesides. The origins and the future of microfluidics. *Nature*, 442(7101): 368–373, July 2006. ISSN 0028-0836. doi: 10.1038/nature05058.

W. H. Wright, G. J. Sonek, and M. W. Berns. Optical trapping of microspheres as a model for biological cells. In *Engineering in Medicine and Biology Society, 1989. Images of the Twenty-First Century., Proceedings of the Annual International Conference of the IEEE Engineering in*, pages 1203–1204 vol.4. IEEE, Nov. 1989. doi: 10.1109/IEMBS.1989.96160.

2.6 Figures

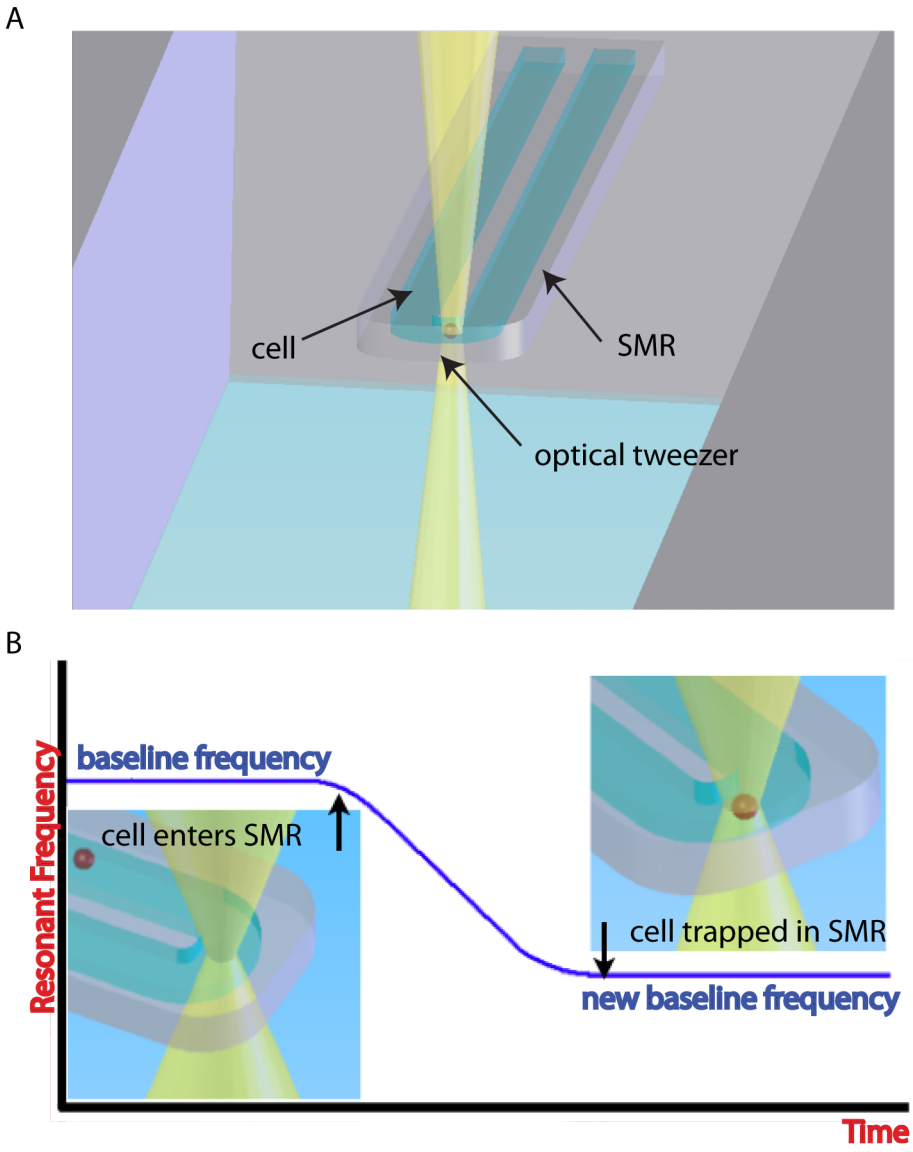

Figure 2-1: Illustration of an optical tweezer positioned within the SMR. (A) Cell trapped by the optical tweezer at the apex of the cantilever. (B) Frequency readout as a cell is trapped.

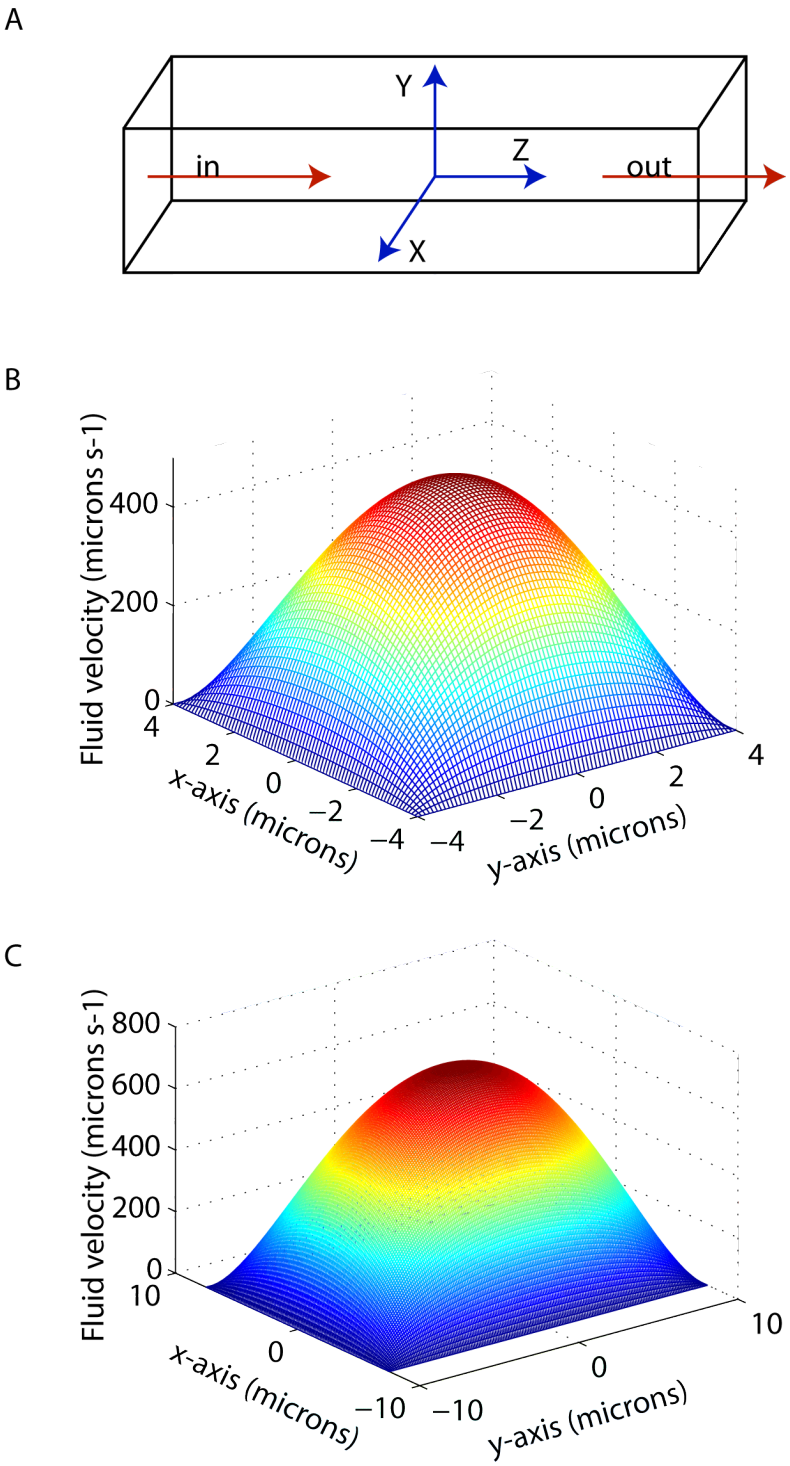

Figure 2-2: (A) A flow cell representation of the cantilever's embedded channel. We report the fluid velocity profile within the SMR for (B) an 8x8 μm channel and (C) a 15x20 μm channel at a flow rate equal to one-half of the channel's total volume per second.

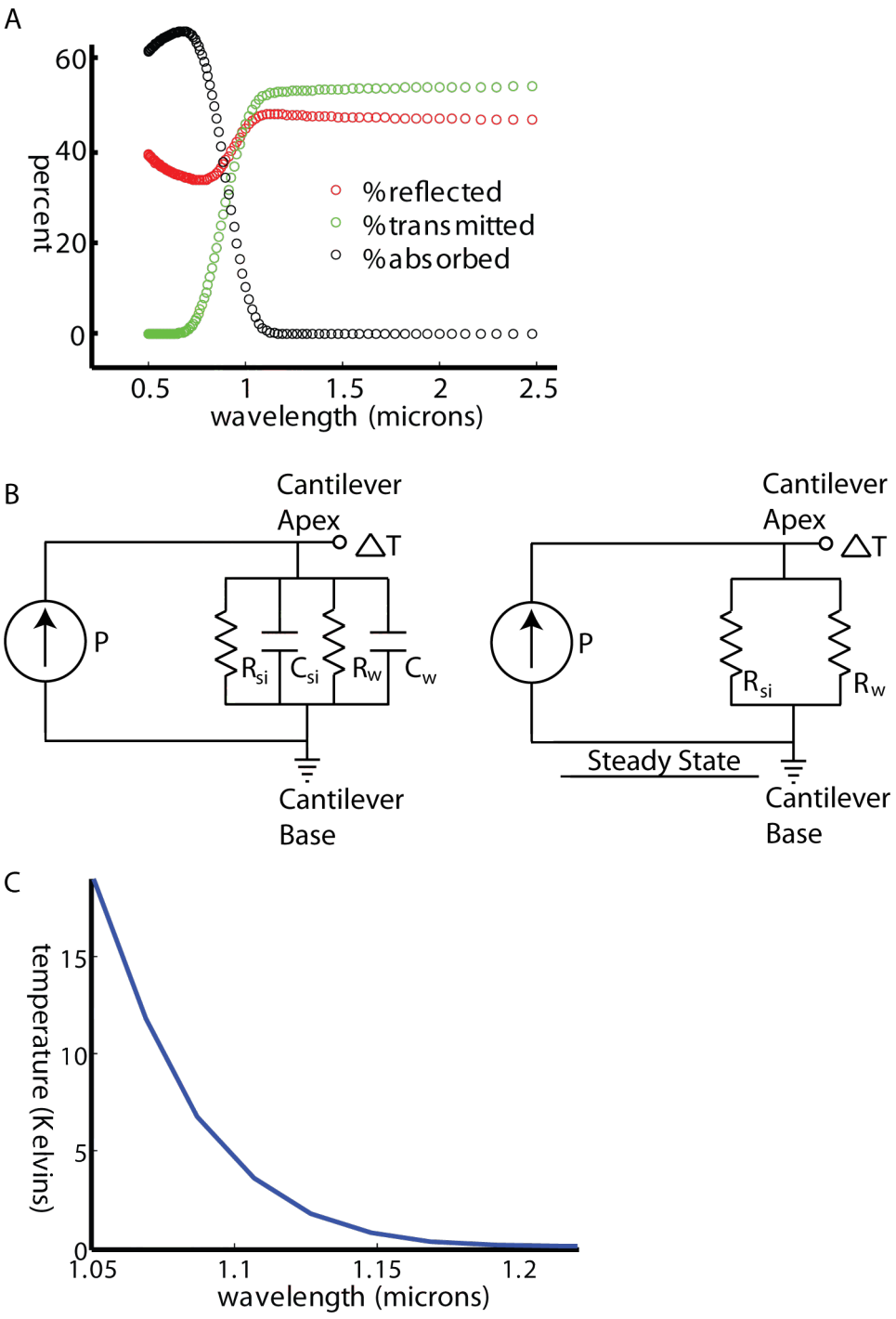

Figure 2-3: (A) Optical properties of silicon $\sim$25 μm in thickness. (B) Lumped-element circuit model of cantilever heating due to focused laser sources. Computation is based on the steady-state model. (C) ΔT at the cantilever apex for an infrared laser at various wavelengths penetrating the surface of the SMR at 100mW.

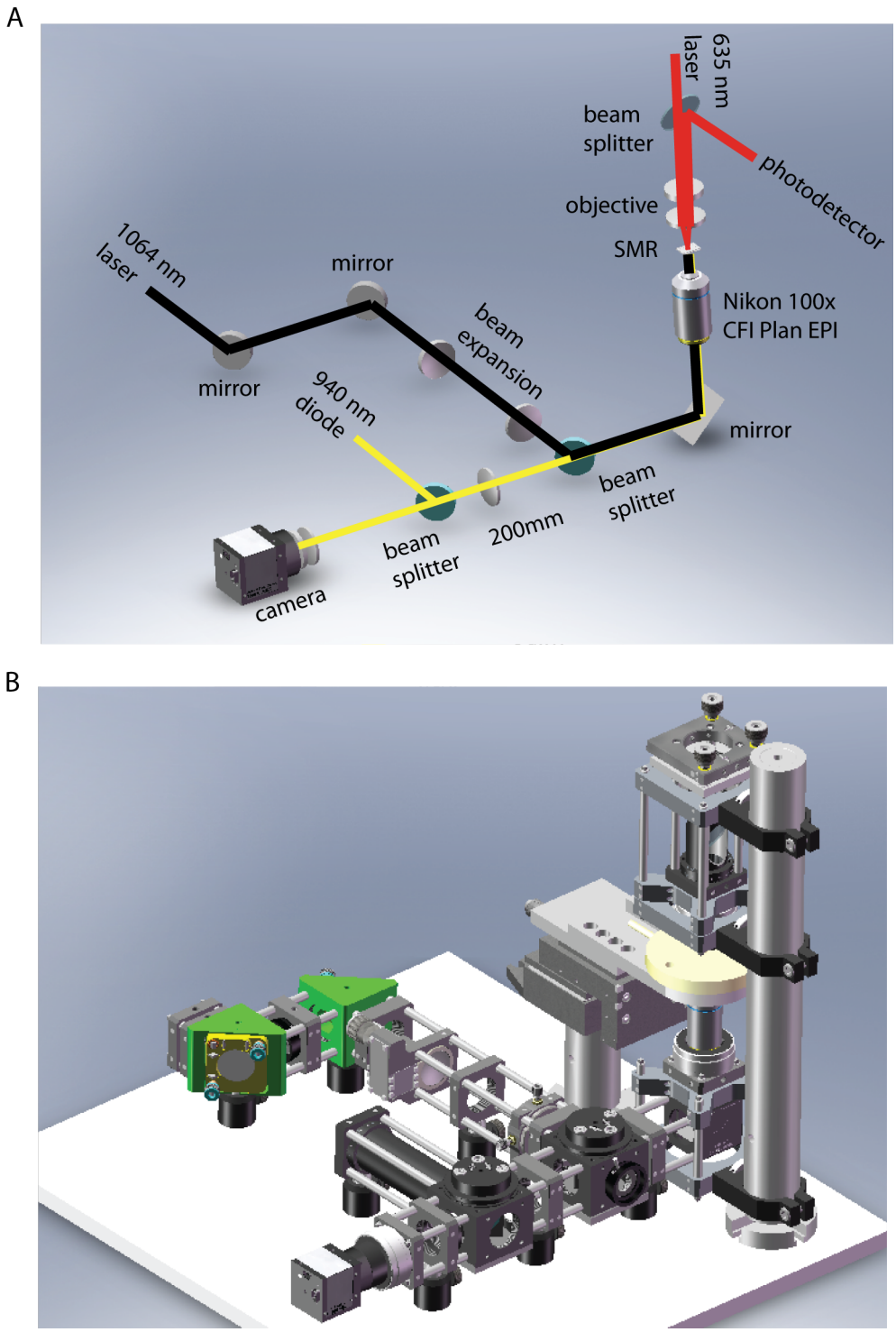

Figure 2-4: (A) Ray tracing diagram for: 1) frequency readout (red); 2) optical tweezer (black); 3) imaging system (yellow). (B) The optical system.

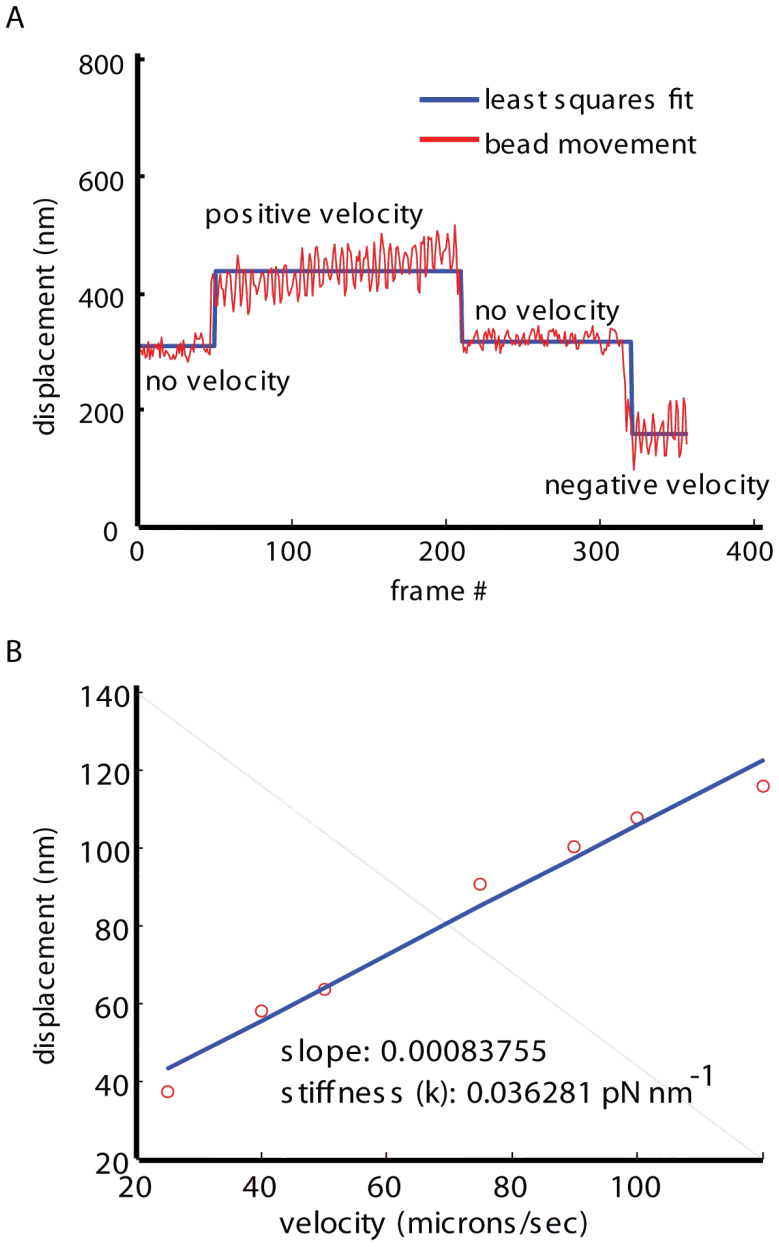

Figure 2-5: (A) A particle tracking algorithm was used to determine the displacement of a trapped bead as a result of applied velocity. Red: frame-by-frame bead position was calculated by weighted centroids. Blue: least squares fit to determine the actual displacement. (B) The displacement of a 3.2 μm object away from the optical trap center for various applied velocities. The stiffness coefficient was determined from the slope of the first order polynomial fit.

2.7 Tables

Table 2-1: The approximate forces required to trap a cell traveling through the SMR at various transit times. The pressure drop across an 8x8 μm and a 15x20 μm channel for the listed transit times are also reported. The value 0.003* psi approaches the lower limits of what can be achieved across the SMR by the pressure regulator.

.

Transit	$\Delta P_{8x8\mu m}$	D=1 μm	D=3.2 μm	D=5 μm	$\Delta P_{15x20\mu m}$	D=10 μm
t=50ms	0.24 psi	77 pN	246 pN	394 pN	0.12 psi	1.06 nN
t=100ms	0.12 psi	38 pN	123 pN	192 pN	0.06 psi	578 pN
t=2s	0.006 psi	1.92 pN	6.14 pN	9.60 pN	0.003* psi	28.9 pN

Table 2-2: The maximum oscillation amplitude of micron-sized objects as a result of SMR vibration. The inertial effects for objects with diameters on the order of channel height are mitigated by the higher resistances of fluid layers close to the wall. In actuality, the amplitudes of oscillation for the 5 and 10 μm objects should be slightly higher than the values reported here.

Object	Oscillation Amplitude (nm)
SMR	100
D=100nm	100
D=1μm	100
D=5μm	78.6*
D=10μm	31.5*

Chapter 3

Mass sensors with mechanical traps for weighing single cells in different fluids

Yaochung Weng, Francisco F. Delgado, Sungmin Son, Thomas P. Burg, Steven C. Wasserman, and Scott R. Manalis

The text and figures presented here originally appeared in *Lab on a Chip*, 11(24):4174, 2011 and have been reproduced by permission of the Royal Society of Chemistry. This chapter was a collaboration with Francisco F. Delgado in the Manalis Laboratory. Y.W., S.S., T.P.B., and S.R.M. designed the SMRs with mechanical traps. Y.W. and F.F.D. developed the instruments, performed experiments, and analyzed data. S.C.W. and S.S. contributed to the instrument development.

Chapter 3

Mass sensors with mechanical traps for weighing single cells in different fluids

3.1 Abstract

We present two methods by which single cells can be mechanically trapped and continuously monitored within the suspended microchannel resonator (SMR) mass sensor. Since the fluid surrounding the trapped cell can be quickly and completely replaced on demand, our methods are well suited for measuring changes in cell size and growth in response to drugs or other chemical stimuli. We validate our methods by measuring the density of single polystyrene beads and *Saccharomyces cerevisiae* yeast cells with a precision of approximately 10^{-3} gcm^{-3} and by monitoring the growth of single mouse lymphoblast cells before and after drug treatment.

3.2 Introduction

The suspended microchannel resonator (SMR) enables single-cell measurements of buoyant mass with femtogram-level resolution (Burg et al., 2007; Godin et al., 2010). The SMR consists of an embedded microfluidic channel inside a cantilever that res-

onates in an on-chip vacuum. Cells or particles with a different density than the surrounding fluid cause a small change in the cantilevers resonant frequency as they flow through the cantilever, and their buoyant mass can be determined from the magnitude of the frequency change. The buoyant mass, or mass of a particle in fluid, is defined as

$$m_{buoyant} = V(\rho_p - \rho_f) \tag{3.1}$$

where V is the particle volume, and ρ_p and ρ_f are the particle and fluid densities, respectively.

Early SMR implementations could provide the buoyant masses of cells in a population but could weigh each cell only once and were unable to monitor single cells over time (Bryan et al., 2010). Later systems added fluidic controls to implement dynamic trapping, during which an individual cell is repeatedly passed back and forth through the SMR. When maintained over extended time periods, this dynamic trap can measure the growth of individual cells in real time (Godin et al., 2010). But delivering chemical stimuli to a dynamically trapped cell is challenging because viscous-dominated flow inside the microchannel ensures that the cell moves along with the surrounding fluid.

Recently, Grover et al. (2011) showed that by loading the SMR device with two different fluids, single cells can be dynamically trapped within the two fluids, weighed in the first fluid and then weighed in the second fluid. This technique is well suited for measuring the density of single cells by weighing them in two fluids of different densities. However, their technique is unsuitable for measuring the response of a cell to chemical stimuli because the duration of exposure of the cell to the second fluid is limited to only a few seconds, and the growth rate of a single cell cannot be measured both pre- and post-treatment with a drug. Finally, the buoyant mass measured by this method is subject to uncertainty caused by variations in the cells flow path through the cantilever. A novel strategy for overcoming these limitations is to physically trap each cell within the SMR. The buoyant mass of the cell could then be monitored continuously while the fluid surrounding the cell is changed at

will. Several designs for cell traps were considered: methods such as standing acoustic waves (Evander et al., 2007), dielectrophoresis (Gray et al., 2004; Issadore et al., 2010) and optical trapping (Johann, 2006; Wang et al., 2003) have their appeal in that no cell contact is necessary and that the action of capturing and releasing a cell can be readily controlled. However, while it is possible to generate forces on the order of tens to hundreds of piconewtons by applying acoustic or electromagnetic waves in an ordinary microfluidic channel, the multilayered geometry and complex design of the SMR device make it difficult to implement these techniques. Mechanical structures involving cell-sized docks preceding a constriction (Valero et al., 2005; Werdich et al., 2004) and U-shaped trapping compartments (Carlo and Lee, 2006; Carlo et al., 2006; Kim et al., 2008; Wheeler et al., 2003) proved to be more robust cell capturers for our application.

Mechanical trapping structures integrated with the SMR can effectively load and unload a single cell while its buoyant mass and the density of the surrounding fluid are continuously monitored. We evaluated two types of mechanical trap: the first, referred to as three-channel SMRs (Figure 4-1A,B), proved to be most suitable for single-cell density measurements, while the second type, referred to as columned SMRs (Figure 4-1C), was used to measure cell growth before and after exposure to a drug.

3.3 Three-channel SMRs

3.3.1 Method

Three-channel SMRs were fabricated as described previously (Burg et al., 2007) with a capture dock at the apex of the cantilever (Figure 4-1A,B) and a third fluidic channel used to control flow into and out of the dock. At the T-junction where the dock meets the third channel (channel 3), a narrow constriction allows fluid to pass, but not cells of the appropriate size. Two versions of the three-channel SMR with different dimensions were fabricated: one with a 3x8 μm channel cross-section and a

200 nm wide horizontal slit; and another with an 8x8 μm channel cross-section device and a 2 μm wide vertical gap. A computer-controlled fluidic system orchestrates a sequence of pressure changes that traps a cell, measures its buoyant mass, quickly replaces the fluid around the cell, measures its buoyant mass a second time in the new fluid, and ejects the cell.

To prime the device, fluid 1 flows from bypass channel B1 to the cantilever. Fluid 1 carries the cells to be measured (Figure 4-2, blue). Relative pressure settings ensure that the majority of fluid 1 travels from B1 to the second bypass B2 via the SMR to minimize the likelihood of cells being captured in the dock. After the device is primed, the fluid velocity through the SMR is reduced, and pressure on the bypass B3 is lowered so that a significant amount of the fluid now flows through the third channel. Thus, a transiting cell will be directed into the pocket and captured (Figure 4-4 inset). Cell capture is detected as a stepwise change in the resonant frequency due to the change in mass inside the cantilever (if the cell sinks, mass increases and frequency decreases; if the cell floats, mass decreases and frequency increases). Cell immobilization eliminates position uncertainty, a source of error, which exists when measuring samples in a flow through mode.

After a cell is trapped, the computer reverses the flow to flush the SMR with fluid 2 (Figure 4-2, red) from bypass channel B2. Fluid 1 is completely rinsed out of the cantilever, leaving the cell immersed in fluid 2. Prior to removing the cell from the trap, bypass B3 is filled with fluid 2, and a constant flow is maintained. This clears out remnants of fluid 1 that have previously exited through the third channel and is crucial for preventing the two fluids from mixing during the ejection step. The control system then gradually pressurizes the third channel until the cell leaves the dock. After the cell is ejected, there is another step in the resonant frequency corresponding to the buoyant mass of the cell in fluid 2. The entire sequence of events takes 3-5 s and can be observed in Supplementary Movie 1. The duration of serial measurements depends on cell concentration. Smaller concentrations of cells will increase the delay between measurements, but high concentrations will lead to multiple cells being trapped.

With two buoyant mass measurements and two measurements of the fluid density, the cells density can be determined. The device is calibrated with fluids of known density, allowing the density of fluids 1 and 2 to be accurately determined. The cell density is, therefore, determined as:

$$\rho_{cell} = \frac{m_{buoyant2} \cdot \rho_{fluid1} - m_{buoyant1} \cdot \rho_{fluid2}}{m_{buoyant2} - m_{buoyant1}} \tag{3.2}$$

Measurement error in the cells density is affected by the choice of densities of fluids 1 and 2. If the reference fluid densities are close, the buoyant mass values in both fluids will also be close, and the measurement error will play a more significant role in (3.2). This error was minimized by choosing reference fluids as far apart in density as was convenient. Furthermore, we took care to bracket the samples density between the fluid densities (fluid 1 is less dense than the cell, and fluid 2 is more dense than the cell). In order to calculate volume and mass, the sensitivity of the SMR, relating buoyant mass to cantilever resonant frequency change, was determined with NIST size standard beads as previously reported (Godin et al., 2010). Note that since the buoyant mass calibration factor affects all the buoyant mass terms proportionally in (3.2), calibration is not actually required for measuring cell density.

3.3.2 Material

Buffers Yeast was grown and measured in yeast extract plus peptone medium supplemented with 2% glucose and 1 $mg\ mL^{-1}$ adenine (YEPD) and bacteria in Luria-Bertani (LB) broth (Sigma-Aldrich L2542). For the secondary fluid for the density measurements we used Milli-Q ultrapure water, deuterium oxide (Sigma-Aldrich 151882) and a 1:9 dilution of 10x PBS (Omnipur 6505) in high-density Percoll (Sigma-Aldrich P4937, modified as reported by Grover et al. (2011)).

Cells Saccharomyces cerevisiae cells (strain A2587) were grown in YEPD at 30 °C with agitation and measured about 2.5 hours after the culture had been started, prior to beginning of exponential growth phase. Escherichia coli (ATCC 25922) were grown in LB overnight at 37 °C then diluted 1:100 an hour before the measurement.

Polystyrene Beads The beads used in the measurements and calibrations were the size standards from Bangs Labs NT17N (1.9 μm) and Thermo Scientific 4205A (5 μm).

3.3.3 Results

We first applied this technique to polystyrene beads, which were measured in water ($\rho = 0.9983\ g\ cm^{-3}$) and deuterium oxide ($\rho = 1.1046\ g\ cm^{-3}$). All experiments were performed at 23.3 °C. The measurements, shown in Table 4-1 and Figure 4-3 for 1.9 μm and 5 μm beads, were carried out in the 3x8 μm and 8x8 μm devices respectively. The results, $\rho_{1.9} = 1.0497 \pm 0.0010\ g\ cm^{-3}$ and $\rho_5 = 1.0491 \pm 0.0008\ g\ cm^{-3}$ (mean $\pm$ standard deviation), matched the reported density of polystyrene ($\sim$1.05 $g\ cm^{-3}$). In addition, we determined the population statistics of the calculated diameters by assuming the volume of a sphere in (3.1). Both samples showed lower standard deviations and coefficients of variation than the ones reported by the manufacturers (Table 4-1).

The method was also used to measure the density of S. cerevisiae cells with an 8x8 μm SMR. The results obtained by consecutive measurements of the cells in their medium ($\rho = 1.0182\ g\ cm^{-3}$) and PBS:Percoll ($\rho = 1.1667\ g\ cm^{-3}$) are shown in Figure 4-4. An average cell density $\rho = 1.1042 \pm 0.0057\ g\ cm^{-3}$, CV = 0.59%, n = 244 (totaling 2 runs) was determined. This value is in accordance with single-cell yeast density measurements obtained through other methods (Table 2). The two experimental runs were measured from two samples taken from the same culture, one hour apart. The measured densities were $\rho = 1.1049 \pm 0.0068\ g\ cm^{-3}$, CV = 0.62% for the earlier one (n=132) and $\rho = 1.1033 \pm 0.0061\ g\ cm^{-3}$, CV = 0.56% for the later sample (n=112). The results for calculated mass are m = 95.08 $\pm$ 46.30 pg, CV = 48.7% and volume V = 78.1 $\pm$ 35.3 μm^3, CV = 45.2% and V = 95.9 $\pm$ 47.5 μm^3, CV = 49.6%, respectively. The data of the two separate measurements are shown in Supplementary Figure 3-1. Volume was also measured with a Coulter Counter (Beckman Coulter, Multisizer 4), V = 78.5 $\pm$ 49.2 μm^3, CV = 62.6% and V = 91.45 $\pm$ 58.5 μm^3, CV = 64.0%, respectively (n = 20,000 cells).

3.3.4 Discussion

The results demonstrate that our method can accurately determine the density, mass, and volume of single cells to the extent that osmotic shock can be avoided or minimized and that the density of the cell being measured can be bracketed by the appropriate solution densities. More than one cell can be trapped at the same time if a cluster of cells enter simultaneously or if the flow reversal time is not short enough to prevent an additional cell from being captured. For density measurements, the capture of multiple cells will result in a measured average, which will mask the variability amongst those cells. However, these events can be detected optically or by size signatures and can be rejected by data analysis.

We further attempted to achieve the same measurement on bacterial cells (E. coli) with the 3x8 μm SMR. However, although single bacterium can be trapped within the pocket, ejection proved to be difficult without large pressure differentials due to cell adhesion to the walls. Further developments such as bacteria-resistant surfaces (Cheng et al., 2009) are still required to successfully measure the density of single bacteria.

3.4 Columned SMRs

3.4.1 Method

In order to measure the drug response of single cells, we used our existing process (Burg et al., 2007) to fabricate SMRs of 15x20 μm cross-sectional area with 3 μm diameter trapping columns that are spaced evenly by 3 μm in a U-shape located either at the side or at the center of the cantilever apex (Figure 4-1C). Two larger bypass channels (100 μm in diameter) deliver fluid to and from the SMR. Under normal device operation, a sample containing cells suspended in a carrier medium (Figure 4-5, blue) is first loaded via pressure driven flow. A single cell entering the SMR that happens to be caught within the columns will result in a step-wise change in resonant frequency corresponding to an increase or decrease in total sensor mass.

Most cells flowing through the SMR follow the path of least resistance and are diverted away from the columns. In order to optimize the likelihood of trapping a cell within the columns, two additional technical components are employed. First, the pressure drop across the SMR is precisely adjusted by a combination of both ambient and hydrostatic control to reduce or eliminate fluid flow; and second, the SMR is driven at higher amplitudes to appreciate a significant centrifugal force on the cell (Lee et al., 2010b). The SMR is typically actuated only by electrostatic forces from an adjacent electrode. In order to generate sufficient vibration amplitude for guiding the cell into the columns, piezoelectric actuation tuned in phase with the electrostatic drive is superimposed. Piezoelectric actuation has been shown to produce a few microns of amplitude in SMR oscillation (Lee et al., 2010a). This in turn exerts a nanonewton-scale centrifugal force on a 10 μm polystyrene bead, which provides enough acceleration to move a bead at rest near the cantilever apex into the trapping compartment in less than a second. The average centrifugal force is given by the following equation

$$\mathbf{F_c} = \frac{\mathrm{m_b}}{2\mathrm{L}}\left[\left(\frac{\Phi \mathrm{A}\omega^2}{\omega^2+\Phi^2}\right)^2 + \left(\frac{\Phi^2 \mathrm{A}\omega}{\omega^2+\Phi^2}\right)^2\right] \tag{3.3}$$

where $\Phi = \frac{6\mu r}{m_b}$, μ is viscosity of the fluid medium, m_b is the buoyant mass of an object with a radius r, A is the amplitude of oscillation, ω is the angular frequency of oscillation, and L is the length of the SMR. Although a similar approach can be used for trapping cells, an overall smaller centrifugal force is experienced by a cell suspended in growth medium. In order to compensate for this, stop flow (or zero pressure differential) across the cantilever must be imposed when a transiting cell arrives at the vicinity of the columns allowing sufficient time to accelerate the cell into the mechanical trap. Appendix C discusses the centrifugal force in greater depth. Once the cell is trapped, a pressure differential across the cantilever is resumed. This is achieved by applying pressure-driven flow to the upstream of both bypass channels. The flow rate on one side is greater than the other in order to prevent the cell from escaping the trap as a new fluid carrying a drug or stimulus enters the SMR (Figure

4-5, red). When the fluidic exchange is completed, the SMR resonant frequency stabilizes. Reversing the flow effectively removes a cell from the trap, resulting in another step-wise shift in resonant frequency.

A drug response experiment begins by employing the dynamic trapping method (Godin et al., 2010) to measure the instantaneous growth rate of the cell. The cell is then mechanically trapped within the columns as described previously, and a new fluid containing the drug is delivered as depicted in Figure 4-5. Following drug delivery, the cell is ejected from the columns and dynamic flow trapping is utilized once again to monitor the buoyant mass of the cell. When compared to statically holding a cell within the SMR, monitoring buoyant mass by dynamically trapping the cell has the important advantage that the baseline signal is measured after every passage in order to correct for drift.

3.4.2 Material

Buffers Cells were grown and measured in Lebovitzs L15 medium (Invitrogen 21083027) supplemented with 10% FBS (Invitrogen no. 16000-044), 0.4% glucose (Sigma-Aldrich G8769) and 1% penicillin/streptomycin mix (Cellgro MT-30-002-CI) at 37 °C. Sodium azide (Sigma Ultra S8032-100G) was added for drug treatment experiments. Deuterium oxide (Sigma-Aldrich 151882) was used as the second fluid for the polystyrene bead measurement.

Cells L1210 mouse lymphoblasts were grown in medium (L-15+FBS+glucose+penstrep) inside tissue culture flasks at 37 °C and at 5% ambient carbon dioxide. Cell culture was maintained in log phase by periodically diluting and re-suspending cells in fresh medium every two days. Total cell count in culture was kept between 50 x 10^3 mL^{-1} and 200 x 103 mL^{-1}. To fix cells, 5 mL of a saturated culture (cell count at 1 x 106 mL^{-1}) was spun down (150 rcf for 5 minutes), washed with 1x PBS, and then re-suspended in 0.5 mL 100 mM phosphate buffer + 0.5 100 mM phosphate buffer solution with 7.4% Formaldehyde and 4% Glutaraldehyde. The sample was then left at room temperature overnight and later washed and re-suspended in 1x PBS. The fixed cells were kept at 37 °C overnight to ensure that any possible molecular exchange

between the cells and the medium have reached equilibrium.

Polystyrene Beads The beads used in the measurements and calibrations were from Bangs Labs NT27N (10 μm).

3.4.3 Results

As with the three-channel SMRs, the feasibility of fluidic exchange for the columned devices was first assessed using 10 μm diameter polystyrene beads. Figure 4-5 reports on this proof of concept experiment. The bead is sinking in water when it is captured in the columns. Following complete fluid replacement, it is then floating in deuterium oxide. In contrast to the three-channel SMRs, any new fluid entering the columned SMRs must first replace the contents of both bypass channels. Thus, the entire process of fluidic exchange, which typically requires 3 to 5 minutes, takes substantially longer than can be achieved by three-channel SMR.

We measured the growth rate of L1210 mouse lymphoblast cells before and after fluidic exchange in three conditions: 1) a single growing cell before and after a control exchange from medium to like medium; 2) a single growing cell before and after exchange from medium to medium + 1% sodium azide; 3) a single fixed cell before and after a control exchange from medium to like medium. Cells that were exchanged from medium to like medium grew at comparable rates before and after fluidic exchange (Figure 4-6A), indicating that shear stress from the fluidic exchange does not alter the short-term growth properties. In contrast, cells that were exchanged from medium to medium + 1% sodium azide exhibited a negative growth rate immediately following exchange (Figure 4-6B). Sodium azide causes ATP synthesis to shut down, which results in depolarization of the cell due to inhibition of active transporters on the plasma membrane in ion exchange (Davies et al., 1990; Riemersma, 1968). An increase in osmotic pressure inside the cell stimulates an increase in uptake of water and thereby decreases the density of the cell. As a result, the buoyant mass decreases. The negative growth rate exhibited following treatment with sodium azide is a biophysical manifestation of the cells inability to maintain a concentration gradient across the plasma membrane. Results from additional measurements are summarized in Figure

4-7.

3.4.4 Discussion

We demonstrated that the columned SMRs can effectively monitor the buoyant mass of a cell before and after drug treatment. However, the columned SMRs have several drawbacks: i) long-term growth studies (in excess of 60 minutes) have not yet been possible to achieve because shear stress from the continuous flow trapping and the fluid exchange ultimately affects cell viability, ii) small pressure fluctuations during the fluidic exchange process can cause the cell to squeeze through the column gaps and escape the trap, and iii) the entire procedure requires approximately an hour to measure the drug response from one cell. The last two drawbacks, when taken together, resulted in an effective throughput of about one cell per day. Nevertheless, the method in its current state can be used to gain biophysical insight into how drugs alter the ability of a cell to uptake nutrients immediately following exposure to a drug.

3.5 Conclusion

Our work augments current SMR capabilities with single-cell manipulation techniques based on mechanical trapping structures. This capability enables measurements that are not possible using flow-through mass sensing. The ability to measure the buoyant mass of an individual cell in two fluids allows its density as well as its response to a drug to be measured. We measured the density, mass, and volume of individual yeast cells in their culture medium and in PBS:Percoll solution. We also measured the dynamics of buoyant mass accumulation and loss in mouse lymphoblast cells before and after complete buffer replacement with and without the presence of a drug or stimulus. We developed two approaches for making these measurements. In the first, three-channel SMRs capture single cells and rapidly exchange the surrounding buffer for a new fluid. Consecutive buoyant mass measurements in different fluids are rapidly acquired without the need for microfluidic mixing. This approach is not

optimal for monitoring growth behavior of the cells prior to and after drug delivery as the presence of a third channel introduces fluidic pressure variations that prevent stable dynamic flow trapping. To address this limitation, we developed columned SMRs that enable a complete fluid exchange throughout the system by temporarily capturing a cell. Dynamic flow trapping can be resumed without hindrance following fluid exchange, thereby allowing for effective growth monitoring before and after drug delivery.

3.6 Acknowledgements

This work was supported by the Institute of Collaborative Biotechnologies through contract no. W911NF-09-D-0001 from the US Army Research Office and the National Cancer Institute contracts R21 CA137695 and Physical Sciences Oncology Center U54CA143874. The authors would like to thank the Kirschner lab at Harvard Medical School for providing L1210 Mouse Lymphoblast cells as well as the Amon lab at the Massachusetts Institute of Technology for providing S. cerevisiae cells (strain A2587). The authors would also like to thank William Grover for his invaluable comments and help with the manuscript. Y.W. acknowledges support through an NSF graduate fellowship. F.F.D. acknowledges support from Fundao para a Cincia e a Tecnologia, Portugal, through a graduate fellowship (SFRH/BD/47736/2008). S.S. acknowledges support from KEF, South Korea, through a graduate fellowship. T.P.B. acknowledges support by the Max Planck Society and the Max Planck Institute for Biophysical Chemistry.

3.7 References

S. Aiba, S. Kitai, and H. Heima. Determination of equivalent size of microbial cells from their velocities in hindered settling. *Journal of General and Applied Microbiology*, 10(3):243–256, 1964.

W. W. Baldwin and H. E. Kubitschek. Buoyant density variation during the cell cycle of saccharomyces cerevisiae. *Journal of Bacteriology*, 158(2):701–704, May 1984. ISSN 0021-9193. PMID: 6373726 PMCID: 215486.

A. K. Bryan, A. Goranov, A. Amon, and S. R. Manalis. Measurement of mass, density, and volume during the cell cycle of yeast. *Proceedings of the National Academy of Sciences of the United States of America*, 107(3):999–1004, Jan. 2010. ISSN 1091-6490. doi: 10.1073/pnas.0901851107. PMID: 20080562.

T. P. Burg, M. Godin, S. M. Knudsen, W. Shen, G. Carlson, J. S. Foster, K. Babcock, and S. R. Manalis. Weighing of biomolecules, single cells and single nanoparticles in fluid. *Nature*, 446(7139):1066–1069, Apr. 2007. ISSN 0028-0836. doi: 10.1038/nature05741.

D. D. Carlo and L. P. Lee. Dynamic Single-Cell analysis for quantitative biology. *Anal. Chem.*, 78(23):7918–7925, 2006. ISSN 0003-2700. doi: 10.1021/ac069490p.

D. D. Carlo, L. Y. Wu, and L. P. Lee. Dynamic single cell culture array. *Lab Chip*, 6 (11):1445–1449, Sept. 2006. doi: 10.1039/B605937F.

G. Cheng, G. Li, H. Xue, S. Chen, J. D. Bryers, and S. Jiang. Zwitterionic carboxybetaine polymer surfaces and their resistance to long-term biofilm formation. *Biomaterials*, 30(28):5234–5240, Oct. 2009. ISSN 0142-9612. doi: 10.1016/j.biomaterials.2009.05.058.

J. M. Davies, C. Brownlee, and D. H. Jennings. Electrophysiological evidence for an electrogenic proton pump and the proton symport of glucose in the marine fungus dendryphiella salina. *Journal of Experimental Botany*, 41(4):449 –456, Apr. 1990. doi: 10.1093/jxb/41.4.449.

M. Evander, L. Johansson, T. Lilliehorn, J. Piskur, M. Lindvall, S. Johansson, M. Almqvist, T. Laurell, and J. Nilsson. Noninvasive acoustic cell trapping in a microfluidic perfusion system for online bioassays. *Analytical Chemistry*, 79(7): 2984–2991, Apr. 2007. ISSN 0003-2700. doi: 10.1021/ac061576v. PMID: 17313183.

M. Godin, F. F. Delgado, S. Son, W. H. Grover, A. K. Bryan, A. Tzur, P. Jorgensen, K. Payer, A. D. Grossman, M. W. Kirschner, and S. R. Manalis. Using buoyant mass to measure the growth of single cells. *Nat Meth*, 7(5):387–390, May 2010. ISSN 1548-7091. doi: 10.1038/nmeth.1452.

D. S. Gray, J. L. Tan, J. Voldman, and C. S. Chen. Dielectrophoretic registration of living cells to a microelectrode array (vol 19, pg 771, 2004). *Biosensors Bioelectronics*, 19(12):1765–1774, 2004.

W. H. Grover, A. K. Bryan, M. Diez-Silva, S. Suresh, J. M. Higgins, and S. R. Manalis. Measuring single-cell density. *Proceedings of the National Academy of Sciences*, June 2011. doi: 10.1073/pnas.1104651108.

S. Haddad and C. Lindegren. A method for determining the weight of an individual yeast cell. *Applied Microbiology*, 1(3):153–156, 1953.

D. Issadore, T. Franke, K. A. Brown, and R. M. Westervelt. A microfluidic microprocessor: controlling biomimetic containers and cells using hybrid integrated circuit/microfluidic chips. *Lab on a Chip*, 10(21):2937–2943, 2010. doi: 10.1039/C0LC00092B.

R. M. Johann. Cell trapping in microfluidic chips. *Analytical and Bioanalytical Chemistry*, 385(3):408–412, Apr. 2006. ISSN 1618-2642, 1618-2650. doi: 10.1007/s00216-006-0369-6.

M. Kim, Z. Wang, R. H. W. Lam, and T. Thorsen. Building a better cell trap: Applying lagrangian modeling to the design of microfluidic devices for cell biology. *Journal of Applied Physics*, 103(4):044701–044701–6, Feb. 2008. ISSN 00218979. doi: doi:10.1063/1.2840059.

J. Lee, R. Chunara, W. Shen, K. Payer, K. Babcock, T. P. Burg, and S. R. Manalis. Suspended microchannel resonators with piezoresistive sensors. *Lab Chip*, 11(4): 645–651, Dec. 2010a. doi: 10.1039/C0LC00447B.

J. Lee, W. Shen, K. Payer, T. P. Burg, and S. R. Manalis. Toward attogram mass measurements in solution with suspended nanochannel resonators. *Nano Lett.*, 10 (7):2537–2542, 2010b. ISSN 1530-6984. doi: 10.1021/nl101107u.

M. Reuss, D. Josic, M. Popovic, and W. Bronn. Vicosity of yeast suspensions. *European Journal of Applied Microbiology and Biotechnology*, 8(3):167–175, 1979.

J. C. Riemersma. Effects of sodium azide and 2,4-dinitrophenol on phosphorylation reactions and ion fluxes in saccharomyces cerevisiae. *Biochimica Et Biophysica Acta*, 153(1):80–87, Jan. 1968. ISSN 0006-3002. PMID: 5638404.

A. Valero, F. Merino, F. Wolbers, R. Luttge, I. Vermes, H. Andersson, and A. van den Berg. Apoptotic cell death dynamics of HL60 cells studied using a microfluidic cell trap device. *Lab on a Chip*, 5(1):49–55, Jan. 2005. ISSN 1473-0197. doi: 10.1039/b415813j. PMID: 15616740.

M. Wang, C. Ozkan, R. Flynn, A. Birkbeck, and S. Esener. Optical manipulation of objects and biological cells in micro uidic devices. *Electrical Engineering*, 5(1): 61–67, 2003.

A. A. Werdich, E. A. Lima, B. Ivanov, I. Ges, M. E. Anderson, J. P. Wikswo, and F. J. Baudenbacher. A microfluidic device to confine a single cardiac myocyte in a sub-nanoliter volume on planar microelectrodes for extracellular potential recordings. *Lab on a Chip*, 4(4):357–362, Aug. 2004. ISSN 1473-0197. doi: 10.1039/b315648f. PMID: 15269804.

A. R. Wheeler, W. R. Throndset, R. J. Whelan, A. M. Leach, R. N. Zare, Y. H. Liao, K. Farrell, I. D. Manger, and A. Daridon. Microfluidic device for Single-Cell analysis. *Anal. Chem.*, 75(14):3581–3586, 2003. ISSN 0003-2700. doi: 10.1021/ac0340758.

3.8 Figures

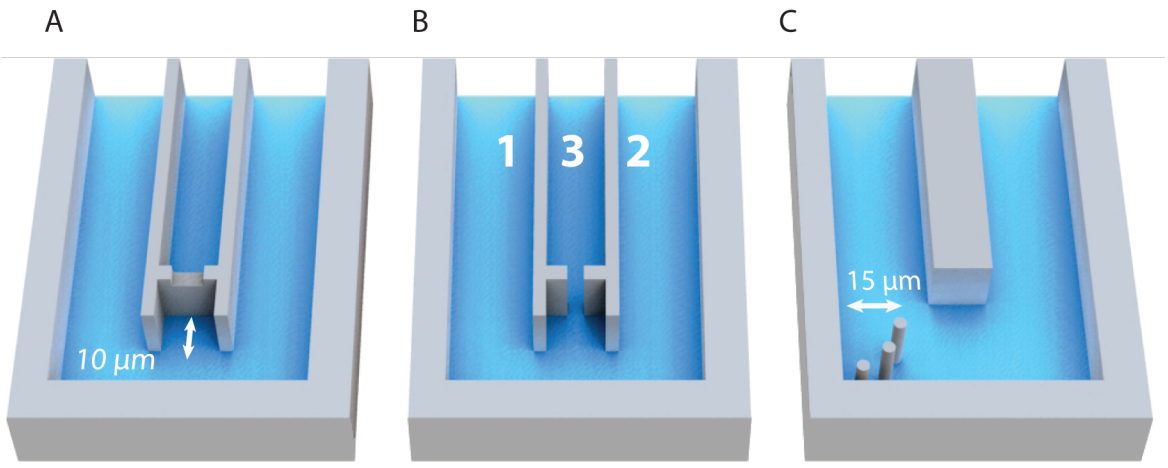

Figure 3-1: Top perspective of SMRs with mechanical traps. Three-channel SMRs with different third-channel dock geometries: (A) 3x8 μm device with a 200 nm horizontal slit and (B) 8x8 μm device with a vertical 2 μm wide opening. (C) Columned SMR.

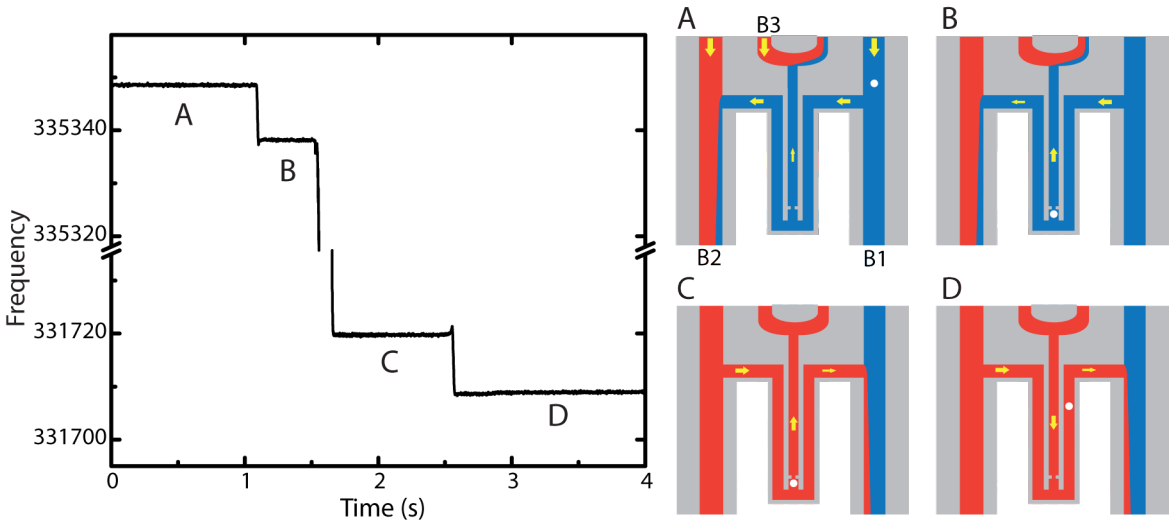

Figure 3-2: SMR resonant frequency response is plotted versus time as the density of a 5 μm polystyrene bead is measured. (A) SMR is filled with water. (B) A bead is trapped. The short spike at the end of the step is due to the bead rounding the corner of the wall, before entering the pocket; (C) Water is replaced by D_2O. (D) The particle is ejected.

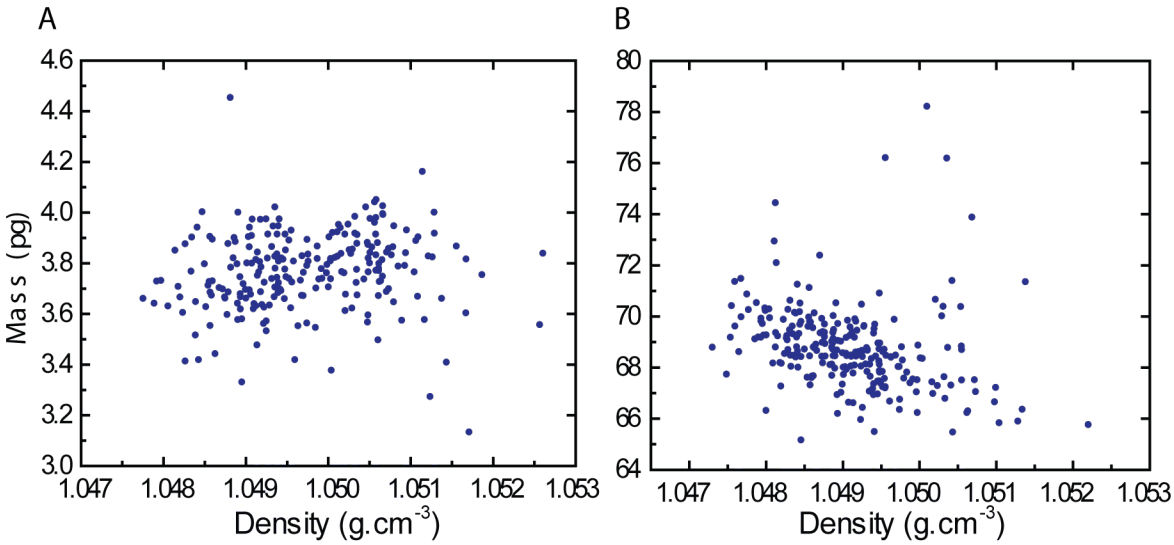

Figure 3-3: Density and mass of polystyrene size standard beads measured in two different three-channel devices. Mean densities: (a) 1.9 μm particles $\rho = 1.0497 \pm 0.0010$ $g\ cm^{-3}$, CV = 0.09%, n = 231 (b) 5.003 μm particles $\rho = 1.0491 \pm 0.0008$ $g\ cm^{-3}$, CV = 0.08%, n = 247.

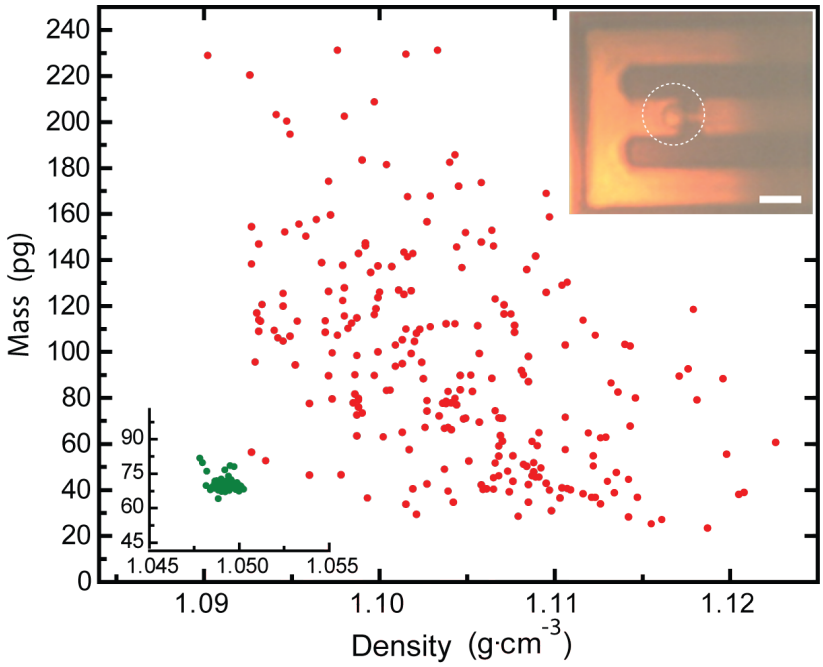

Figure 3-4: Density and mass of S. cerevisiae cells. Mean density $\rho = 1.1042 \pm 0.0066\ g\ cm^{-3}$, CV = 0.59%, n = 244. Inset plot Density and mass of 5 μm polystyrene beads measured in the same conditions as the cells. Scales are the same as the main plot. The biological variability as determined by the spread of cell measurements is less than the instrument variability as predicted by the measurement and dispersion of bead samples. Inset picture Immobilized cell (circled). Scale bar: 10 μm.

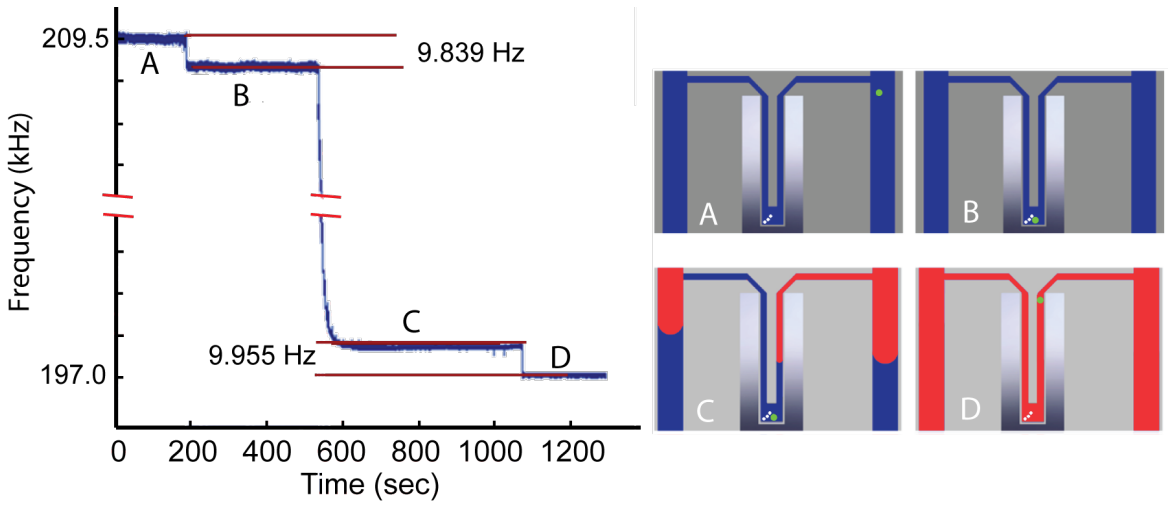

Figure 3-5: Columned SMR device operation. (A) Empty channel; (B) 10 μm polystyrene bead (green, ρ =1.05 $g\ cm^{-3}$) is trapped in H2O (blue, ρ =1.00 $g\ cm^{-3}$); (C) Fluid is exchanged to D_2O (red, ρ =1.10 $g\ cm^{-3}$); (D) Bead is ejected from trap.

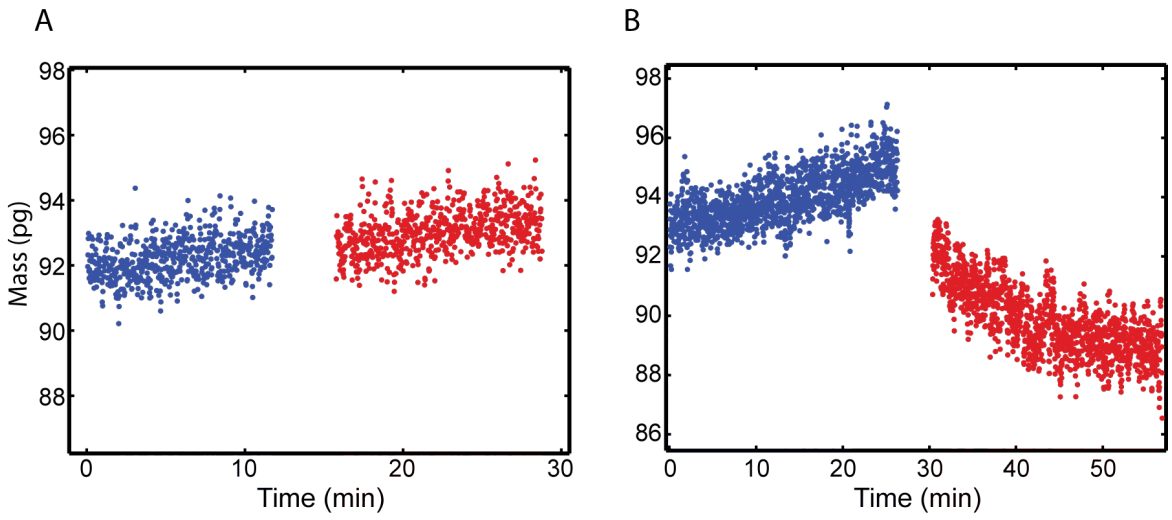

Figure 3-6: The buoyant mass versus time of individual L1210 mouse lymphoblast cells. (a) Control: monitored in medium (red) and exchanged into medium (blue). (b) Drug delivery: monitored in medium (red) and exchanged in medium with 1% sodium azide (blue).

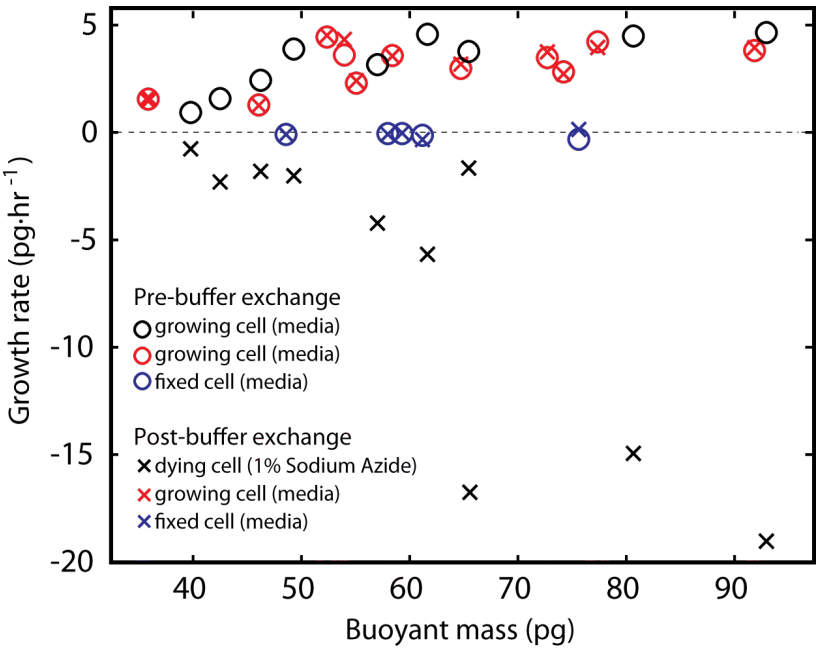

Figure 3-7: The growth rates of all L1210 mouse lymphoblast cells monitored before and after fluidic exchange. The fixed cell measurements determined the noise floor of the technique to be -0.1296 $\pm$ 0.1109 $pg\ hr^{-1}$ before the exchange and -0.0809 $\pm$ 0.1697 $pg\ hr^{-1}$ after the exchange.

3.9 Tables

Table 3-1: Density and population statistics of the diameter of polystyrene beads. Diameter was calculated from (3.1) assuming the volume of a sphere. Mean values (*) of diameter are the same by definition as they were used as buoyant mass calibration, therefore the values are merely indicative.

sample		**density**	**diameter**	
		$g \cdot cm^{-3}$	µm	
			measured	datasheet
1.9 µm (n=231)	Mean	1.0497	1.9*	1.9*
	St. Dev	1×10^{-3}	0.03	0.03
	CV (%)	0.09%	1.4%	1.6%
5.0 µm (n=247)	Mean	1.0491	5.003*	5.003*
	St. Dev	8×10^{-4}	0.04	0.05

Table 3-2: Reported measurements of yeast density.

reference	density $g \cdot cm^{-3}$	method
Reuß et al. (1979)	1.0952 ± 0.011	Anton Parr DMA 45 densitometer
Aiba et al. (1964)	1.090 ± 0.0112	settling velocity
Haddad et al. (1953)	1.087 ± 0.026	settling velocity
Baldwin et al. (1984)	1.1126 ± 0.010	density gradient centrifugation
Bryan al. (2010)	1.1029 ± 0.0026	SMR + Coulter Counter
current result	1.1042 ± 0.0066	SMR

3.10 Supplementary Data

Supplementary Movie 1 Two consecutive measurements of yeast cells, each in medium and PBS:Percoll.

Supplementary Movie 2 The demonstration of inertial trapping in the columned SMR using a polystyrene bead.

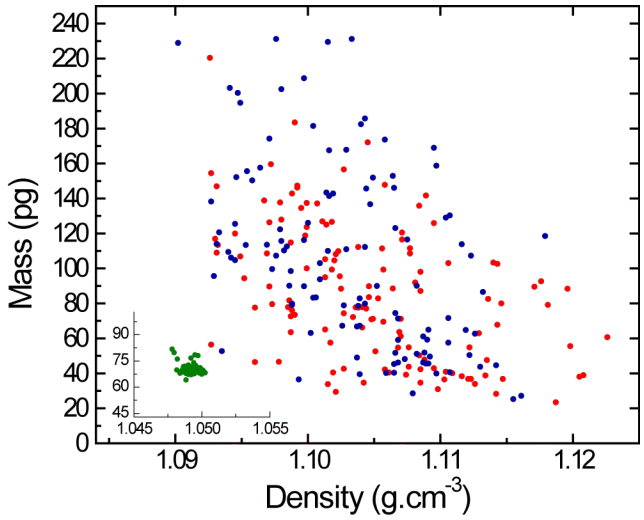

Supplementary Figure 3-1: Density and mass of S. cerevisiae cells. The plot is the same as Figure 4, but distinguishes the two different samples. The measured densities were $\rho = 1.1049 \pm 0.0068\ g\ cm^{-3}$, CV = 0.62% for the sample measured 2 hour after the culture was started (red, n=132) and $\rho = 1.1033 \pm 0.0061\ g\ cm^{-3}$, CV = 0.56% for the sample measured 3 hour after the culture was started (blue, n=112). Inset plot Density and mass of 5 μm polystyrene beads measured in the same conditions as the cells. Scales are the same as the main plot.

Chapter 4

Measuring the dynamics of single-cell growth in response to drug therapy

Yaochung Weng, Kris C. Wood, Sungmin Son, David M. Sabatini, and Scott R. Manalis

Y.W., K.C.W., S.R.M., and D.M.S. designed the experiments. Y.W. developed the instrument, performed all experiments, and analyzed data. K.C.W. performed the radiolabeled leucine incorporation assay and analyzed data. S.S. contributed to the long-term trapping methodology.

Chapter 4

Measuring the dynamics of single-cell growth in response to drug therapy

4.1 Abstract

Measurements that describe the average response of a cell population to a perturbation can obscure the behaviors of individual cells, which may be heterogeneous or may contain information not described by bulk averaging. Here, we developed a microfluidic system that enables sensitive, long-term single-cell growth measurements in response to dynamically changing environmental conditions. Using this system, we demonstrated that cells can exhibit significantly different growth responses to three distinct drugs which act, at least in part, by inhibiting protein synthesis. In addition, we showed that the instantaneous responses of single cells to drug intervention may predict long-term responses of both single cells and bulk populations. The tools and findings described here may have implications for mapping chemical, genetic, or environmental perturbations to classes of cellular responses and for rapidly predicting drug responses in patient-derived samples.

4.2 Introduction

Cell growth is an important phenotype for assessing drug response. The most complete characterization of the effect of a chemical perturbation on cell growth would be to dynamically monitor the change in size of individual cells before and after exposure to a drug. This would reveal not only the variation in growth dynamics between cells within the population but also how a particular cell alters its own behavior in response to a therapy.

Aldridge et al. (2012) recently achieved single-cell growth measurements by using microscopy to monitor the length of mycobacterial cells within microfluidic channels. They found that asymmetric growth and division results in subpopulations of cells that vary in their susceptibility to clinically relevant classes of antibiotics. Previously, Balaban et al. (2004) used a similar method to observe persister E. coli cells. They discovered that these cells, which were not antibiotic resistant but persisted after ampicillin treatment, grew at a lower rate than untreated cells even prior to drug exposure. A lower than normal growth rate is an inherent characteristic of persister cells and not the result of antibiotic treatment. Although analogous studies with mammalian cells could potentially provide valuable, finely-resolved insights into the individual responses of cancer cells to drugs, an appropriate method still does not exist.

Three essential criteria are required for establishing a growth monitoring system for mammalian cells: i) the size of irregularly shaped cells must be monitored with high precision over extended periods of time; ii) cells must proliferate in the system as they do in standard cultures; and iii) the drug must be uniformly delivered to the cells within a defined time period without perturbing cell growth from excess shear stress. Each of these criteria has been separately demonstrated. For example, Lecault et al. (2011) developed a microfluidic platform containing thousands of nanoliter-scale chambers suitable for live-cell imaging studies of clonal cultures of nonadherent cells with precise control of the conditions over periods approaching 100 hours. However, the conventional microscopy used in their study, while appropriate for monitoring

cell proliferation, was not suitable for measuring cell size with meaningful precision. In contrast, Reed et al. (2011) used interferometry, an advanced form of optical microscopy (DAVIES and WILKINS, 1952), to measure the dry mass of cells with a precision of nearly 1%. However, cells were not tracked before drug delivery and were only monitored for five hours after the initial treatment. Recently, we used a suspended microchannel resonator (SMR) with mechanical traps to observe the dynamic changes in the buoyant mass of a cell before and after sodium azide exposure (Weng et al., 2011). However, studies in excess of an hour could not be achieved since shear stress from continuous dynamic trapping for growth monitoring (Godin et al., 2010) would eventually degrade cell viability. Furthermore, the throughput was extremely low because cells trapped in mechanical structures were frequently lost due to pressure fluctuations during drug delivery .

Here we have created a method called the Microfluidic Mass-based Analysis of Single-cell Stimulation (MMASS) which satisfies each of the essential criteria described above. MMASS uses the SMR to measure the buoyant mass of single mammalian cells with a precision near 0.05%, and its measurements are not influenced by cell morphology (Burg et al., 2007). It employs an advanced dynamic trapping system, which uses periodic cell storage, to enable continuous monitoring of a cell and its progeny for over a hundred hours and tens of generations without compromising viability (Son et al., 2012). More importantly, this method incorporates a single-cell manipulation technique we have developed specifically to provide an on-demand evolution of a cell's surrounding from one fluid environment to another within a five-minute window. As the cell successively moves between two larger bypass channels through the SMR, the contents of each are incrementally refreshed. In this fashion, the same cell can be transferred from normal growth media to growth media containing an added drug without introducing additional stress which may alter or affect growth. Using MMASS, we measured the growth of single cancer cells before and after drug therapy with high resolution, revealing unexpected cellular behaviors that provide new insights which may be useful for rapidly predicting drug activities in cells, including limited cell populations.

4.3 Results

MMASS is loaded sequentially upstream of the SMR with growth media (Figure 4-1, blue) followed by growth media carrying a drug (Figure 4-1, red). Cells are loaded downstream by forming a fluidic loop from one bypass channel to the other through the embedded channels of the cantilever. As a cell flows through the SMR, its buoyant mass is reflected as a peak in sensor frequency. To keep the cell dynamically trapped, the system reverses flow every time a cell transit through the SMR is sensed. During this iterative process, the cell is brought out deep into the bypass channels and a substantial amount of fluid is displaced (Figure 4-1A-F) until all of the existing growth media upstream has been exchanged with new growth media containing a drug. Due to a density tag placed within the carrier media, the sensor baseline frequency shifts when the drug enters the SMR and stabilizes when the drug has been delivered at full concentration.

Because shear stress resulting from fast or frequent transit through the SMR into nearby bypass channels can perturb growth, we first established that the dynamic trapping and drug delivery processes do not alter the long-term growth trajectory, the viability, and the interdivisionary period of the cells. We accomplished this by measuring the growth of single mouse lymphocytic leukemia cells (L1210) before and after exchanging the growth media vial with another vial of identical growth media. Figure 4-2A shows the growth, or mass accumulation, of a cell (black line) and that of its subsequent generations (colored lines). The first cell was dynamically trapped and monitored until mitosis, after which one of the two daughter cells was expelled and the other was kept for additional monitoring. This process occurred at the end of every cell-cycle, resulting in the multiple single-cell trajectories shown. The media exchange took place during the growth of the first cell and is denoted by the demarcation between the red and the blue backdrop. To determine if the media exchange altered the growth trajectory, it is helpful to observe how the growth rate of each cell (defined as the rate at which it accumulates mass) changes as it progresses through the cell cycle. Figure 4-2B plots the growth rate (time-derivative

of trajectories shown in Figure 4-2A) as a function of the cell mass at the time the derivative was calculated. Every trajectory in Figure 4-2B, which is color-coded to correspond to its generation shown in Figure 4-2A, spans from the mass at which the cell was born to that at which it divided. As the cells increased in mass, their growth rates also increased. This observation agrees well with a previous study by Tzur et al. (2009). Furthermore, the individual cell's growth rate versus mass was overlaid on a gray shading which represents the estimated range of expected values derived from control cells (N=12) grown in pure media, which were consistent with those of a more extensive growth study (N=100) by Son et al. (2012). All cells grew near or within the expected growth rate and mass ranges. The first cell's growth rate remained unaffected by the fluidic exchange (denoted by the asterisk) and even slightly exceeded the range of expected growth rates just prior to mitosis. In addition, the interdivisionary period of a single-cell was found to be approximately 10 hours, which is in agreement with bulk measurements from a healthy culture (Rauscher and Cadman, 1983).

We used MMASS to monitor the growth of L1210 cells before and after treatment with 250 nM Torin1, a selective molecule inhibitor of the mTOR kinase, which regulates cell growth, cell cycle progression, and protein synthesis (Figure 4-2C and Supplementary Figure 4-3A-F) (Guertin and Sabatini, 2007, 2009; Liu et al., 2010; Sarbassov et al., 2005). Single-cell responses were quantitatively heterogeneous but shared principle qualitative features. We found that single-cell growth appeared largely unaffected immediately (2-4 hours) following drug treatment, but at later times (5-10 hours), growth of the treated cell (Figure 4-2C, green) began to slow appreciably relative to controls grown without Torin1. Smaller cell masses were accompanied by progressively increasing interdivisionary periods (Figure 4-2C, blue and Supplementary Figure 4-3) and decreasing cell sizes at division. Typically, a complete cessation of mass accumulation was observed 1-3 divisions after the initial treatment of a cell. In some cases, this was followed by a significant loss of mass. Figure 4-2D shows that the growth rate versus mass of cells (black and red) prior to drug treatment fell within the expected range of control cells. Although the first treated cell (green)

continued to grow at approximately the same rate shortly after drug treatment, it was neither able to reach the mass nor attain the growth rate of its predecessors at mitosis. The subsequent generation (blue) exhibited lower birth size, total mass accumulation, and growth rate, leading eventually to zero or negative growth.

We next investigated the growth response of L1210 cells following treatment with two additional inhibitors of growth and protein synthesis, staurosporine (STS) and cycloheximide (CHX). STS is a multi-targeted kinase inhibitor that is capable of inducing apoptosis through both caspase-dependent and -independent mechanisms (Belmokhtar et al., 2001). Figure 4-2E and Supplementary Figure 4-4 show that cells treated with 3 μM STS exhibited slower than expected mass accumulation beginning 2 hours post-treatment, followed by a dramatic loss of mass at approximately 5 hours. Figure 4-2F shows that following STS-treatment, a cell continued to increase in mass at a steady rate before falling short of the expected range of growth rates. In contrast, treatment with cycloheximide (CHX) (5 $\mu g\ mL^{-1}$), an inhibitor of eukaryotic protein biosynthesis that interferes with the translocation step in translation (Baliga et al., 1969), resulted in an almost immediate impairment of cell growth, with complete growth inhibition within 2-3 hours of treatment, followed again by a significant loss of mass (Figure 4-2G and Supplementary Figure 4-5). Figure 4-2H indicates that upon treatment with CHX, the cell exhibits a dramatic change in growth rate which immediately fell below the expected range of an unperturbed cell.

We further investigated whether or not short-term single cell drug response data may provide insights into longer term cellular behaviors. As shown in Figure 4-3A, there is a correlation between the amount of time required for a cell to stop growing and the instantaneous effects of the drug on the same cell as represented by the growth rate ratio (GRR), which is determined by the ratio of the growth rates calculated within 30-minute windows before and after delivery of the drug. To assess the effects of each drug on the growth of a population of cells, we measured leucine incorporation, a proxy for total mass accumulation (Figure 4-3B). As expected, we found that CHX, which results in the lowest GRR, reduces population protein synthesis by more than 90% within two hours of exposure. At the other end of the spectrum, Torin1, which

results in the highest GRR, suppresses protein synthesis by 47% nearly a day after the initial treatment. STS, which results in an intermediate GRR, reduces protein synthesis by more than 90% some time between 5 and 20 hours of exposure. Finally, we hypothesized that impairment of single-cell mass accumulation may also affect proliferation because progression through the biosynthetic phases of the cell cycle would be expected to occur more slowly. To determine if there is a relationship between growth and proliferation, we performed a 72-hour time-lapsed cell count on a bulk population following treatment with the same drugs and found that cells treated with drugs that decrease growth rate also proliferated at significantly slower rates than did control (DMSO-treated) cells (Figure 4-3C).

4.4 Discussion and Conclusion

To our knowledge, MMASS is the first system that allows for the high-precision measurement of long-term growth dynamics in single mammalian cells during exposure to dynamically changing environmental conditions. Control experiments involving single-cell growth in media followed by an exchange into the same media have shown that the method of drug delivery does not affect the growth dynamics of an unperturbed cell. A comparison of interdivisionary period between single-cell and bulk measurements further supports the observation that cells are viable and divide regularly from one cell cycle to the next in this system.

Using MMASS, we resolved the growth dynamics of individual cells in response to pharmacological perturbations. We found that three drugs, each of which impairs cell growth at least in part by inhibiting protein synthesis, cause distinct cellular growth trajectories on differing timescales, suggesting differing modes of action. Additional mechanistic insights can also be ascertained from these measurements. For example, by measuring individual cell growth before and after the addition of CHX, a drug which potently inhibits protein translation, it is possible to place an upper limit on the amount of time required for drug transport through the cell membrane and subsequent ribosome inhibition to impact cellular-level growth processes (2-3 hours).

Second, a cell treated with STS, a multi-targeted kinase inhibitor known to induce apoptosis (Belmokhtar et al., 2001), maintains a significant period of continued growth (3-8 hours) before it begins to show signs of mass loss, a likely indicator of apoptosis (Bortner and Cidlowski, 2002). Our findings contrast those of a prior report which demonstrated an increase in cell density due to volume loss shortly after exposure to STS, implying that the cell responds to this drug within minutes (Grover et al., 2011). Interestingly, this discrepancy suggests that an STS-treated cell is capable of growth, i.e. nutrient uptake, protein synthesis, and mass accumulation, despite undergoing an initial rapid loss of volume.

We also demonstrated that following treatment with Torin1, a cell does not change its growth appreciably until 5-10 hours post-drug treatment, when its growth rate begins to slow substantially as compared to cells grown in pure media. Decreased growth rates, smaller cell sizes at division, and progressively increasing interdivisionary periods follow, all of which are consistent with the known role of the mTOR pathway in growth and cell-cycle regulation. The eventual cessation of mass accumulation observed in single cells parallels the cytostasis observed in bulk populations treated with Torin1 (Thoreen et al., 2009). These data provide the first direct evidence that the smaller cell sizes which commonly result from mTOR inhibition (Guertin and Sabatini, 2009) are the result of successively smaller cell sizes at division, which result in successively smaller daughter cells, rather than the direct shrinking of a cell upon drug addition. This phenomenon may reflect the depletion of an mTOR-controlled, limiting cellular factor required for proper cell growth. According to this hypothesis, the inhibition of mTOR results in the diminished abundance of this factor, which is diluted upon successive rounds of cell division until a critical threshold is reached, beyond which continued growth cannot proceed. Additional studies will be required to confirm this hypothesis, identify the relevant factor(s), and clarify the role of cell cycle staging on its effects.

Finally, our data suggests that the GRR parameter can be used to relate the short- and long-term effects of drug exposure on a cell's fate. Based on these data, we hypothesize that it may be possible to rapidly identify drugs which impair cell

growth and proliferation using the instantaneous GRR, an accessible quantity that can be empirically determined from a single cell in less than an hour. We are currently performing studies using a diverse set of drugs to confirm the generality of this relationship. In the future, we anticipate that MMASS may enable the rapid identification of effective anticancer drugs in cell lines and patient-derived tumor cells.

4.5 Material and Methods

Mouse Lymphoblast Culture and Growth Medium. L1210 mouse lymphocytic leukemia cells were cultured and measured in Lebovitz's L15 medium (Invitrogen 21083027) supplemented with 0.4% (wt/vol) glucose (Sigma-Aldrich G8769), 10% (wt/vol) fetal bovine serum (Invitrogen 16000-044), and 1% (wt/vol) penicillin streptomycin mix (Cellgro MT-30-002-CI). The cells were grown inside tissue culture flasks at 37°C and at an ambient 5% carbon dioxide. The culture was kept in log phase by periodically taking an aliquot of cells and re-suspending it into fresh medium every 48 hours. Cell count was maintained between 50 x 103 mL^{-1} and 200 x 103 mL^{-1}. Single-cell growth conditions inside the SMR emulated that of the culture (L15+FBS+glucose+penstrep medium and 37°C).

For drug response measurements, the growth medium was additionally supplemented with the drug of interest. The final concentrations are listed in the following: 250nM Torin1 (provided by N.S. Gray, Dana-Farber Cancer Institute), 3 μM staurosporine (Sigma-Aldrich S6942), and 5 $\mu g\ mL^{-1}$ cycloheximide (Calbiochem 239763). The drugs were dissolved in DMSO (Sigma-Aldrich 472301).

Priming the Microfluidic System. A schematic of the microfluidics is illustrated in Supplementary Figure 4-1. The SMR device consisted of two larger bypass channels connected by a buried channel (15 x 20 μm in cross-section) embedded in a mass-sensing silicon cantilever (SMR). The bypass channels provided two independent flow paths from a single upstream sample vial to the downstream waste vials. A portion of the fluid content from either bypass could be diverted through the SMR to the other by applying a pressure differential across the buried channel. In a typical experiment,

the three glass vials were pressurized by two computer-controlled pressure regulators (Proportion Air) which were multiplexed by solenoid valves (SMC) to generate three distinct pressure levels: atmosphere (atm), P, P-ΔP. Supplementary Figure 4-1A shows that the first step in any experiment was filling the channels and fluidics with growth media. At a pressure differential of 15 psi between upstream and downstream, it took less than two minutes for the entire system to be primed.

Sample Loading. Supplementary Figure 4-1B,C illustrates a technique we employed for sample loading to ensure that only a single cell was monitored by the system. One of the two downstream vials containing 1 mL of water was replaced with 1 mL of cell sample (25 x 10^3 counts). Positive gauge pressure P = 8 psi was applied on both the upstream sample vial (containing growth medium) and the downstream sample vial (containing cells). The remaining waste vial was kept at atmospheric pressure, or 0 psi gauge pressure. In this configuration, pinch flow in one bypass channel forced the upstream media and the downstream cells to converge upon entry into the SMR. On the other bypass, there was a constant flow of media from sample to waste. When a cell transit was sensed by the SMR, the gauge pressure on the waste vial was raised 8 psi to balance the pressure and to achieve stop flow. At the flow rates and cell concentration described here, cell loading took approximately 2-3 minutes.

Dynamic Trapping. Once a cell was loaded, the upstream sample vial was replaced with one containing 1mL of media supplemented with the drug of interest, and the downstream cell sample was replaced with 1mL of water (Supplementary Figure 4-1D). The heights of all the vials were also adjusted accordingly so that the cell remains stationary within the bypass channel during stop flow. Keeping the fluids at the same volume and balancing the vial heights prevented unwarranted gravitational leakage flow. Supplementary Figure 4-1E,F demonstrates how a single cell was kept within the system and how additional cells were flushed out. The process involved keeping the upstream sample vial at a positive gauge pressure of P = 2.5 psi while the downstream waste vials alternated between P = 0 and P = 2.5 psi. Dynamic trapping software written in NI Labview 10.0 was used to sense cell transit upon which, the computer actuated the solenoid valves to alternate the pressure settings.

With every iterative reverse flow, the cells were brought out deep into the bypass. Additional cells loaded in the system were flushed out into the waste. Simultaneously, growth media supplemented with a drug began loading into a reservoir upstream of the bypass channels.

During growth monitoring, the flow rate across the SMR was reduced substantially as the pressure in the waste vials alternated between P- $\Delta P = 2.3$ psi and $P = 2.5$ psi. The transit time of a cell through the cantilever was approximately 100 milliseconds. Every flow reversal event (triggered by a cell transit through the SMR) was preceded by 1-2 minutes of stop flow where the cell was held within the large bypass channels. In long-term dynamic trapping, the system cycled through the sequence beginning with Supplementary Figure 4-1G. When the cell passed through the SMR and entered the left bypass, the system proceeded to stop flow, or cell storage, (Supplementary Figure 4-1H) for 1-2 minutes. This was followed by a flow reversal event (Supplementary Figure 4-1I). Upon completion of the cell transit in Supplementary Figure 4-1I, the system entered another stop flow (not shown), or cell storage in the right bypass, and then returned to the configuration in Supplementary Figure 4-1G for a new cycle. Lengthening the interval between mass measurements reduced the collective shear stress on the cell from frequent transits through the SMR and was essential to the cell's long-term survival.

Because the fluid entering the SMR from upstream and downstream was pinched at each flow reversal step (Supplementary Figure 4-1G, 4-1I), the cell was hydrodynamically focused to either the inner or outer wall of the embedded channel. Fluid flow within the SMR is viscous dominated, so the cell's path was confined the entire way during traversal. Hydrodynamic focusing has been shown to reduce the measurement error of a mammalian cell's buoyant mass in the SMR down to as low as 0.05% in standard deviation (Son et al., 2012).

Fluid Switching. The process of evolving a cell's surrounding from growth media to growth media carrying a drug involved the successive forwarding of fluid from the upstream reservoir while simultaneously re-suspending the cell into a gradually changing environment as shown in Figure 4-1A-F. The dynamic trapping software

utilized time derivative of SMR frequency to detect cell transit. Cells could be trapped in fluids of various densities enabling the use of a density tag to indicate the entry of a new fluid into the SMR. Prior to each experiment, a density tag was introduced on the media carrying the drug by evaporating ∼1% of its water content.

The pressure settings used for fluid forwarding (or drug delivery) were the same as those described in Supplementary Figure 4-1E,F for flushing out excess cells in the bypass and for loading new fluid into the upstream reservoir (upstream sample vial is kept at a positive gauge pressure of P = 2.5 psi while the downstream waste vials alternated between P = 0 and P = 2.5 psi). At these pressure differentials, cells were brought out deep into the bypass channel on the downstream side resulting in tens of nanoliters of new fluid entering the system per iteration. The number of cell transits per minute is increased by ten to twenty times and the transit duration across the SMR is reduced ten folds from 100 milliseconds to 10 milliseconds. The entire exchange was completed in less than 5 minutes.

Leucine Incorporation Assay. Four culture flasks were used, each containing one of the following: DMSO (2 $\mu L\ mL^{-1}$), Torin1 (250 nM), STS (3 μM), and CHX (5 $\mu g\ mL^{-1}$). At t=0, 5 $\mu Ci\ mL^{-1}$ 3H-leucine (American Radiolabeled Chemicals) was added to each culture flask along with drugs at the concentrations listed above. At the indicated time points (2, 5, and 20 h), cell suspensions were pelleted by centrifugation and media was removed by aspiration. Cells were washed twice with ice cold PBS. Cells were then resuspended in 1 mL of ice cold 10% trichloroacetic acid (TCA) in H2O and incubated at 4°C for 30 min. Precipitates were then washed with ice cold PBS and dissolved with 0.5 M NaOH at room temperature (1 mL). Leucine incorporation was determined by scintillation counting of the resulting solution.

Coulter Counter Volumetric Measurements. 72-hour time-lapsed cell count measurements were taken on the Multisizer 4 Coulter Counter for four culture flasks each containing the same contents as that listed in the leucine incorporation assay. At t=0, the drug of choice was added into the culture flask and an aliquot of the cells was measured to determine initial cell concentration. Thereafter, the measurements were repeated at t=2, 5, 10, 20, 42, and 72 hours.

Data Processing. The buoyant mass versus time presented here was derived by smoothing raw data with a 30-minute moving average. For growth rate versus mass, a point-by-point derivative was taken on the smoothened data. An additional 30-minute time window was applied to smooth the results of the growth rate calculation. For GRR computation, 30-minute windows of raw data before and after drug delivery were fitted with linear curves. The time to no growth from drug delivery was calculated based on the following criterions: 1) the average growth rate had to be at most 10-fold less than that prior to drug treatment; 2) the growth of the cell cannot be more than 1% of its total growth from birth after the determined time point.

Error Calculation. The error was calculated from analyzing the raw data of a cell trapped for over ten hours with no apparent growth. The standard deviation of the raw data over a 30-minute window was used to estimate the error bar for buoyant mass versus time. Supplementary Figure 4-6A shows a red line representing the average mass across a 30-minute window superimposed on the raw data. Supplementary Figure 4-6B shows a histogram of the data in Supplementary Figure 4-6A with a Gaussian fit. The measurement error across a 30-minute window was determined to be approximately 0.14% of the cell's mass in standard deviation. Growth rates over the entire 12-hour window were then calculated by a 30-minute sliding window linear fit. In a cell without appreciable growth, the growth rate should be centered about zero pg hr-1. Therefore, a good estimate of the error would be the maximum and minimum growth rate over the 12-hour window (Supplementary Figure 4-6C).

System Calibration. Polystyrene beads from Bangs Labs NT27N (10 μm) with a known density and a standardized volume were measured by the SMR to generate a histogram of resonant frequency shifts. The mass of a polystyrene bead (density x volume) was divided by the average resonant frequency shift to determine the calibration factor ($pg\ hz^{-1}$).

4.6 Acknowledgements

We thank the Kirschner lab at Harvard Medical School for providing the L1210 mouse lymphocytic leukemia cell lines and the knowledge regarding cell culture. This research was funded by the Institute of Collaborative Biotechnologies through contract no. W911NF-09-D-0001 from the US Army Research Office and the National Cancer Institute contracts R21 CA137695 and Physical Sciences Oncology Center U54CA143874. Y.W. acknowledges support through an NSF graduate fellowship. K.C.W. is the recipient of a NIH Ruth L. Kirschstein National Research Service Award and a Misrock Fund Postdoctoral Fellowship through the Koch Institute for Integrative Cancer Research at MIT. S.S. is supported by a graduate fellowship from KEF, South Korea.

4.7 References

B. B. Aldridge, M. Fernandez-Suarez, D. Heller, V. Ambravaneswaran, D. Irimia, M. Toner, and S. M. Fortune. Asymmetry and aging of mycobacterial cells lead to variable growth and antibiotic susceptibility. *Science*, 335(6064):100 –104, Jan. 2012. doi: 10.1126/science.1216166.

N. Q. Balaban, J. Merrin, R. Chait, L. Kowalik, and S. Leibler. Bacterial persistence as a phenotypic switch. *Science (New York, N.Y.)*, 305(5690):1622–1625, Sept. 2004. ISSN 1095-9203. doi: 10.1126/science.1099390. PMID: 15308767.

B. S. Baliga, A. W. Pronczuk, and H. N. Munro. Mechanism of cycloheximide inhibition of protein synthesis in a cell-free system prepared from rat liver. *The Journal of Biological Chemistry*, 244(16):4480–4489, Aug. 1969. ISSN 0021-9258. PMID: 5806588.

C. A. Belmokhtar, J. Hillion, and E. Sgal-Bendirdjian. Staurosporine induces apoptosis through both caspase-dependent and caspase-independent mechanisms. *Oncogene*, 20(26):3354–3362, June 2001. ISSN 0950-9232. doi: 10.1038/sj.onc.1204436. PMID: 11423986.

C. D. Bortner and J. A. Cidlowski. Apoptotic volume decrease and the incredible shrinking cell. *Cell Death and Differentiation*, 9(12):1307–1310, Dec. 2002. ISSN 1350-9047. doi: 10.1038/sj.cdd.4401126. PMID: 12478467.

T. P. Burg, M. Godin, S. M. Knudsen, W. Shen, G. Carlson, J. S. Foster, K. Babcock, and S. R. Manalis. Weighing of biomolecules, single cells and single nanoparticles in fluid. *Nature*, 446(7139):1066–1069, Apr. 2007. ISSN 0028-0836. doi: 10.1038/nature05741.

H. G. DAVIES and M. H. F. WILKINS. Interference microscopy and mass determination. *Nature*, 169(4300):541, Mar. 1952. doi: 10.1038/169541a0.

M. Godin, F. F. Delgado, S. Son, W. H. Grover, A. K. Bryan, A. Tzur, P. Jorgensen, K. Payer, A. D. Grossman, M. W. Kirschner, and S. R. Manalis. Using buoyant mass to measure the growth of single cells. *Nat Meth*, 7(5):387–390, May 2010. ISSN 1548-7091. doi: 10.1038/nmeth.1452.

W. H. Grover, A. K. Bryan, M. Diez-Silva, S. Suresh, J. M. Higgins, and S. R. Manalis. Measuring single-cell density. *Proceedings of the National Academy of Sciences*, June 2011. doi: 10.1073/pnas.1104651108.

D. A. Guertin and D. M. Sabatini. Defining the role of mTOR in cancer. *Cancer Cell*, 12(1):9–22, July 2007. ISSN 1535-6108. doi: 10.1016/j.ccr.2007.05.008. PMID: 17613433.

D. A. Guertin and D. M. Sabatini. The pharmacology of mTOR inhibition. *Sci. Signal.*, 2(67):pe24, Apr. 2009. doi: 10.1126/scisignal.267pe24.

V. Lecault, M. VanInsberghe, S. Sekulovic, D. J. H. F. Knapp, S. Wohrer, W. Bowden, F. Viel, T. McLaughlin, A. Jarandehei, M. Miller, D. Falconnet, A. K. White, D. G. Kent, M. R. Copley, F. Taghipour, C. J. Eaves, R. K. Humphries, J. M. Piret, and C. L. Hansen. High-throughput analysis of single hematopoietic stem cell proliferation in microfluidic cell culture arrays. *Nat Meth*, 8(7):581–586, July 2011. ISSN 1548-7091. doi: 10.1038/nmeth.1614.

Q. Liu, J. W. Chang, J. Wang, S. A. Kang, C. C. Thoreen, A. Markhard, W. Hur, J. Zhang, T. Sim, D. M. Sabatini, and N. S. Gray. Discovery of 1-(4-(4-Propionylpiperazin-1-yl)-3-(trifluoromethyl)phenyl)-9-(quinolin-3-yl)benzo[h][1,6]naphthyridin-2(1H)-one as a highly potent, selective mammalian target of rapamycin (mTOR) inhibitor for the treatment of cancer. *J. Med. Chem.*, 53(19):7146–7155, 2010. ISSN 0022-2623. doi: 10.1021/jm101144f.

r. Rauscher, F and E. Cadman. Biochemical and cytokinetic modulation of l1210 and HL-60 cells by hydroxyurea and effect on 1-beta-D-arabinofuranosylcytosine metabolism and cytotoxicity. *Cancer Research*, 43(6):2688–2693, June 1983. ISSN 0008-5472. PMID: 6189585.

J. Reed, J. Chun, T. Zangle, S. Kalim, J. Hong, S. Pefley, X. Zheng, J. Gimzewski, and M. Teitell. Rapid, massively parallel Single-Cell drug response measurements via live cell interferometry. *Biophysical Journal*, 101(5):1025–1031, Sept. 2011. ISSN 0006-3495. doi: 10.1016/j.bpj.2011.07.022.

D. D. Sarbassov, S. M. Ali, and D. M. Sabatini. Growing roles for the mTOR pathway. *Current Opinion in Cell Biology*, 17(6):596–603, Dec. 2005. ISSN 0955-0674. doi: 10.1016/j.ceb.2005.09.009. PMID: 16226444.

S. Son, A. Tzur, Y. Weng, P. Jorgensen, M. W. Kirschner, and S. R. Manalis. Direct observation of cell growth and size regulation in mammalian cell. *submitted manuscript.*, Jan. 2012.

C. C. Thoreen, S. A. Kang, J. W. Chang, Q. Liu, J. Zhang, Y. Gao, L. J. Reichling, T. Sim, D. M. Sabatini, and N. S. Gray. An ATP-competitive mammalian target of rapamycin inhibitor reveals rapamycin-resistant functions of mTORC1. *Journal of Biological Chemistry*, 284(12):8023–8032, Mar. 2009. ISSN 0021-9258, 1083-351X. doi: 10.1074/jbc.M900301200.

A. Tzur, R. Kafri, V. S. LeBleu, G. Lahav, and M. W. Kirschner. Cell growth and size homeostasis in proliferating animal cells. *Science*, 325(5937):167 –171, July 2009. doi: 10.1126/science.1174294.

Y. Weng, F. F. Delgado, S. Son, T. P. Burg, S. C. Wasserman, and S. R. Manalis. Mass sensors with mechanical traps for weighing single cells in different fluids. *Lab on a Chip*, 11(24):4174, 2011. ISSN 1473-0197, 1473-0189. doi: 10.1039/c1lc20736a.

4.8 Figures

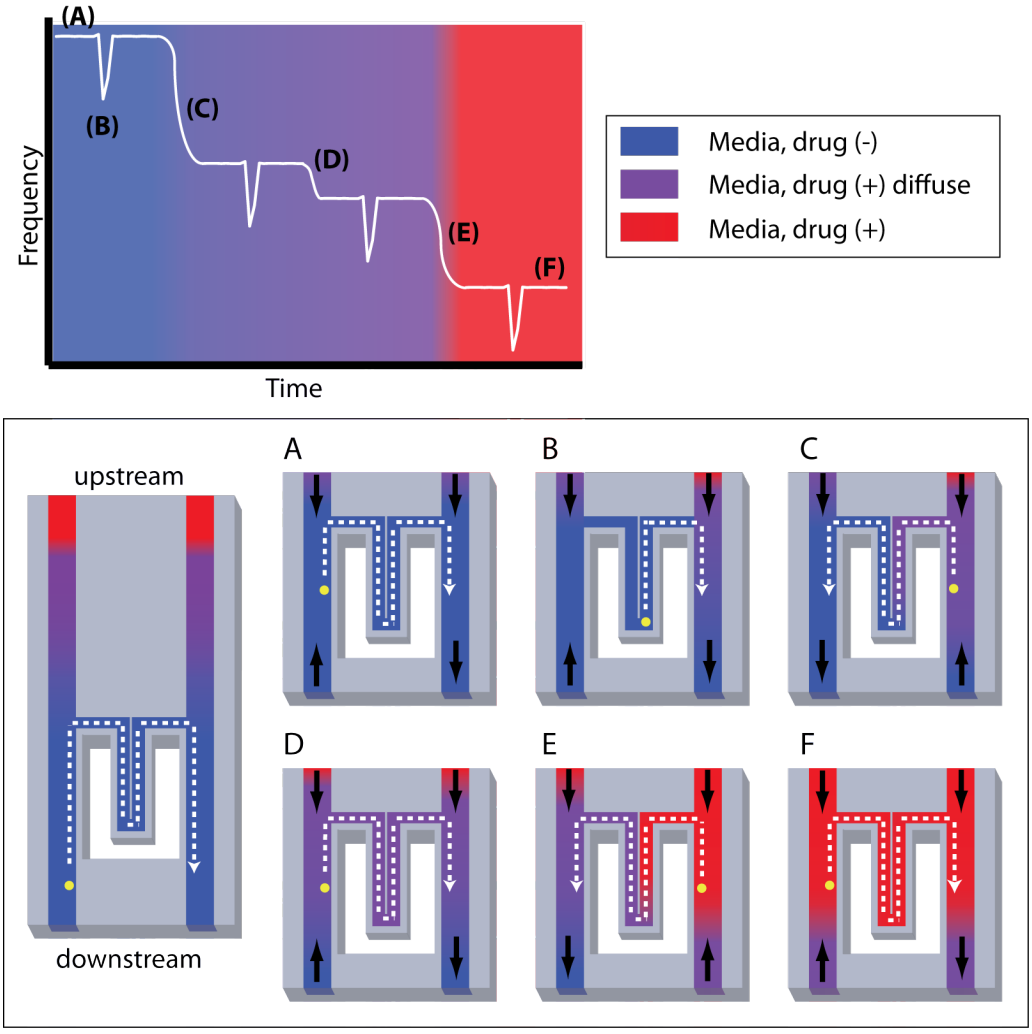

Figure 4-1: The progression of fluid exchange in the channel and drug delivery to the cell Is illustrated (left: sensor readout; right: the corresponding state of the SMR device). At the interface between media (blue) and media with drug (red), there is a minor amount of mixed fluid (purple) that is flushed out during drug delivery. A) cell is in growth media only. B) peak corresponds to cell passing through the sensor. C,D) cell is suspended into new media and sensor baseline frequency shifts as channel is filled with media containing diffuse drug. E,F) cell is suspended into new media and sensor baseline frequency shifts as channel is filled with growth containing the drug at full concentration.

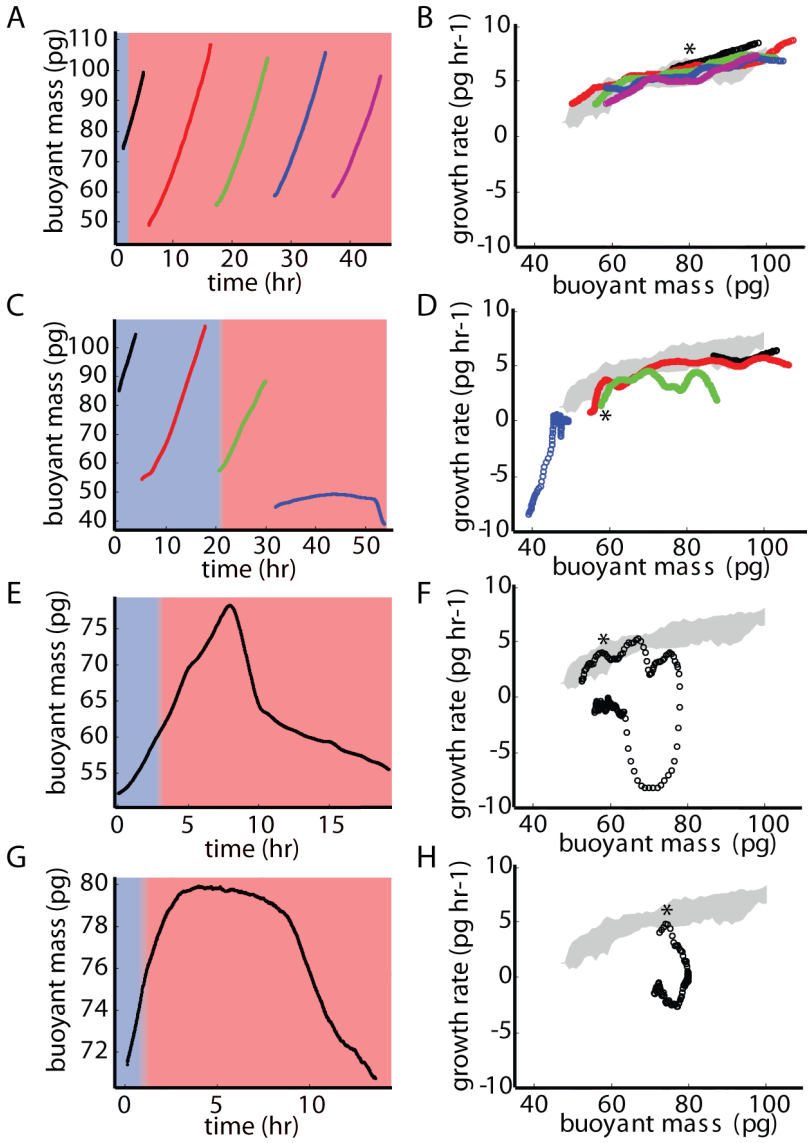

Figure 4-2: A) The mass accumulation of a cell grown in growth media exchanged into growth media. New growth media delivery occurred at the time point where the blue backdrop becomes red. The mass versus time of a single progeny from subsequent generations are also shown. B) The growth rate versus size of each cell generation shown in A; gray shading represents the growth rate of 12 untreated cells; asterisk (*) denotes fluidic exchange. C) Growth response of single cells in the same lineage to mTOR inhibition. Black and red represents cells that grew in pure media. Treatment with 250 nM took place in early green. D) Growth rate versus size of (C). E) Growth response of a single cell treated with $3\mu M$ STS. F) Growth rate versus mass of (E). G) Growth response of a single cell treated with $5\mu g$ mL-1 CHX. H) Growth rate versus mass of (G).

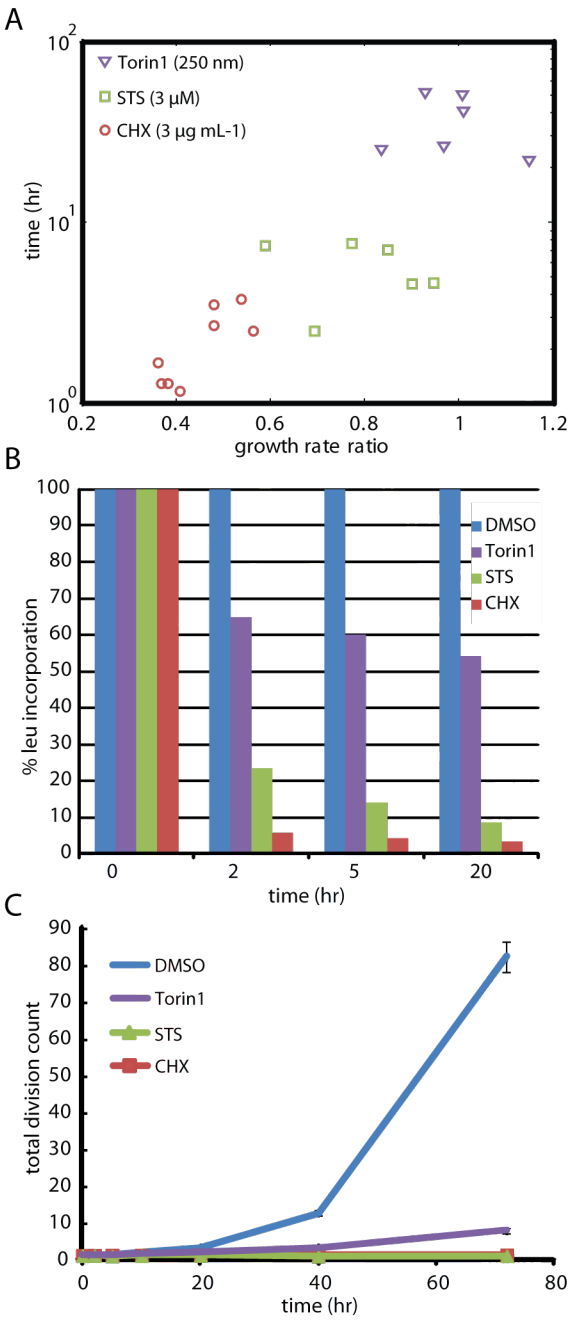

Figure 4-3: A) Cumulative time following drug treatment required for a cell to reach minimal or no growth versus GRR, the ratio that compares the instantaneous growth rate after to that before drug delivery. B) Leucine incorporation assay performed on bulk cultures treated with vehicle (DMSO), Torin1, STS, or CHX to obtain population growth rates. C) Proliferation assay by cell count following drug treatment.

4.9 Supplementary Figures

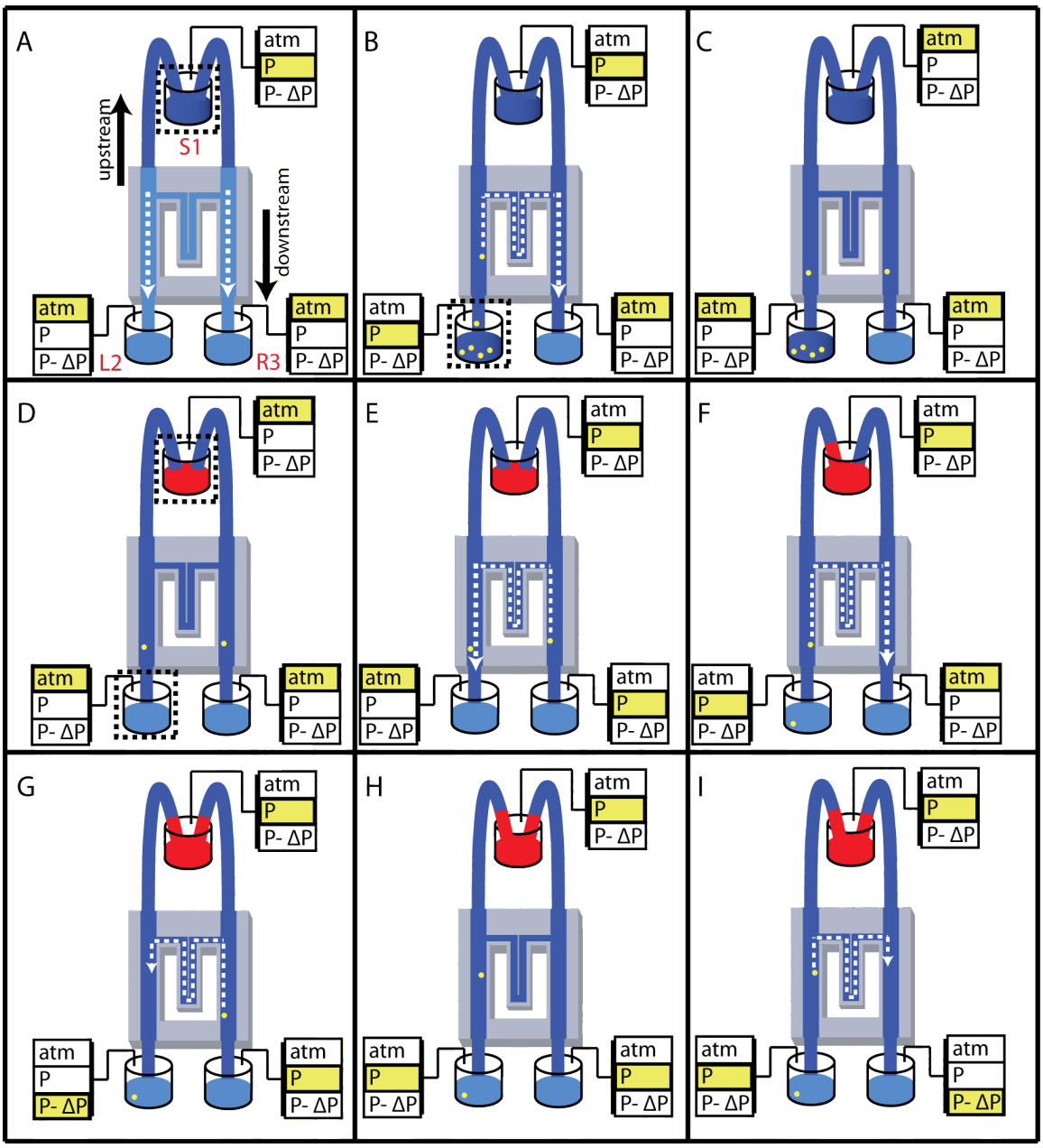

Supplementary Figure 4-1: Schematic of MMASS fluidics. Upstream source vial is referred to as S1, downstream left vial is referred to as L2, and downstream right vial is referred to as R3. A) Priming step: contents of S1 are flushed through both bypasses to the L2 and R3. B) Cell loading step: L1 (containing waste) is replaced with cell sample. Pressure (P) applied on L2 and S1. C) Cell loading is complete after a single cell passes through the SMR from the left to the right bypass; pressure on all vial is set to atmosphere (atm). D) S1 (containing media) is replaced with another (containing media + drug). L2 is replaced with waste vial. At this point, all vials contain the same amount of fluid; heights of vial are adjusted to ensure that there is no leakage flow due to gravity during stop flow. E) Pressure (P) is applied to S1 and R3 to reverse flow enabling the cell in the

right bypass to pass through the SMR into the left bypass. F) Pressure (P) is applied to the S1 and L2 to reverse flow enabling the cell to return to the right bypass. Steps (E) and (F) flush out any extra cells loaded into the system and are also used during drug delivery while keeping a single cell trapped. G) Pressure (P) is applied to S1 and L2, and a smaller pressure (P-ΔP) is applied to R3. This reverses the flow to bring the cell back through the SMR again. H) After the cell arrives at left bypass, pressure (P) is applied to all vials to ensure stop flow. Cell is stored here for a designated amount of time. I) Another flow reversal event occurs (P to S1 and R3, P-ΔP to L2) to bring the cell back through the SMR and is followed by another cell storage step (P to all vials) once it arrives at the right bypass. Steps (G), (H), and (I) describe the fluidic manipulation for long-term dynamic trapping.

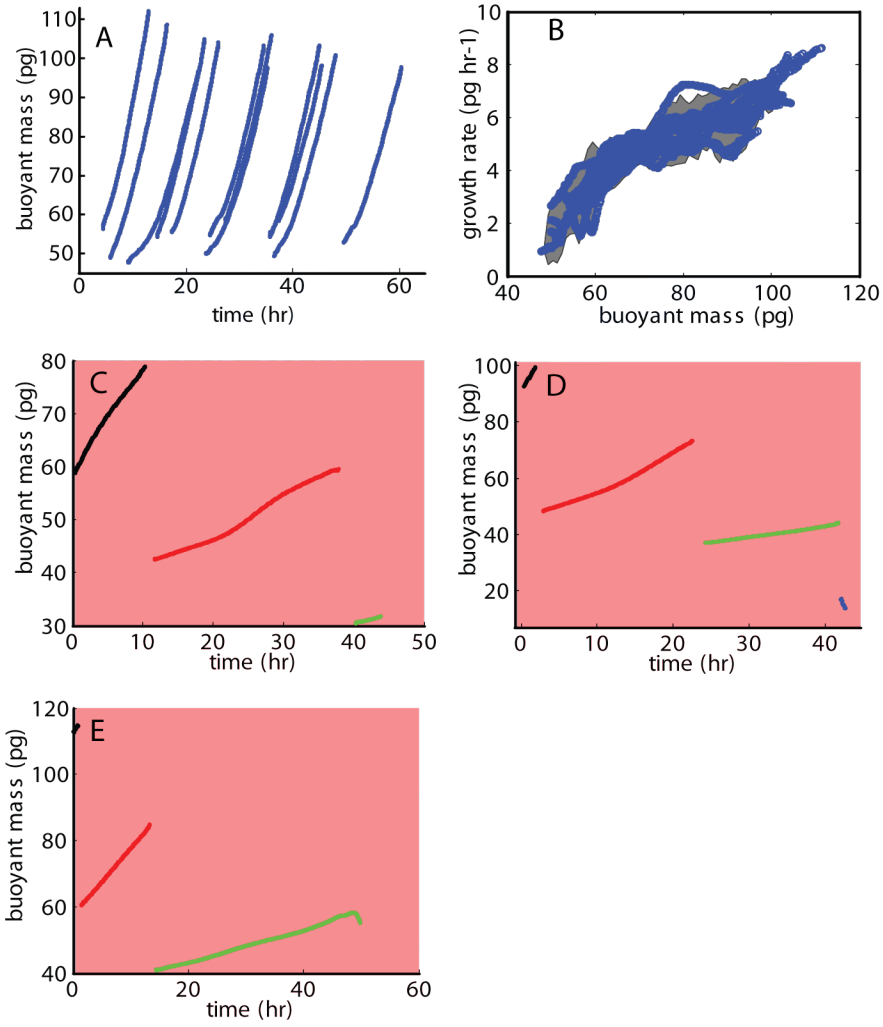

Supplementary Figure 4-2: A) Mass versus time of cells growing in media. B) Growth rate versus time of untreated cells. C,D,E) As a comparison to on-chip treated cells, growth trajectories of cells pre-treated with Torin1 (250 nM) are reported here.

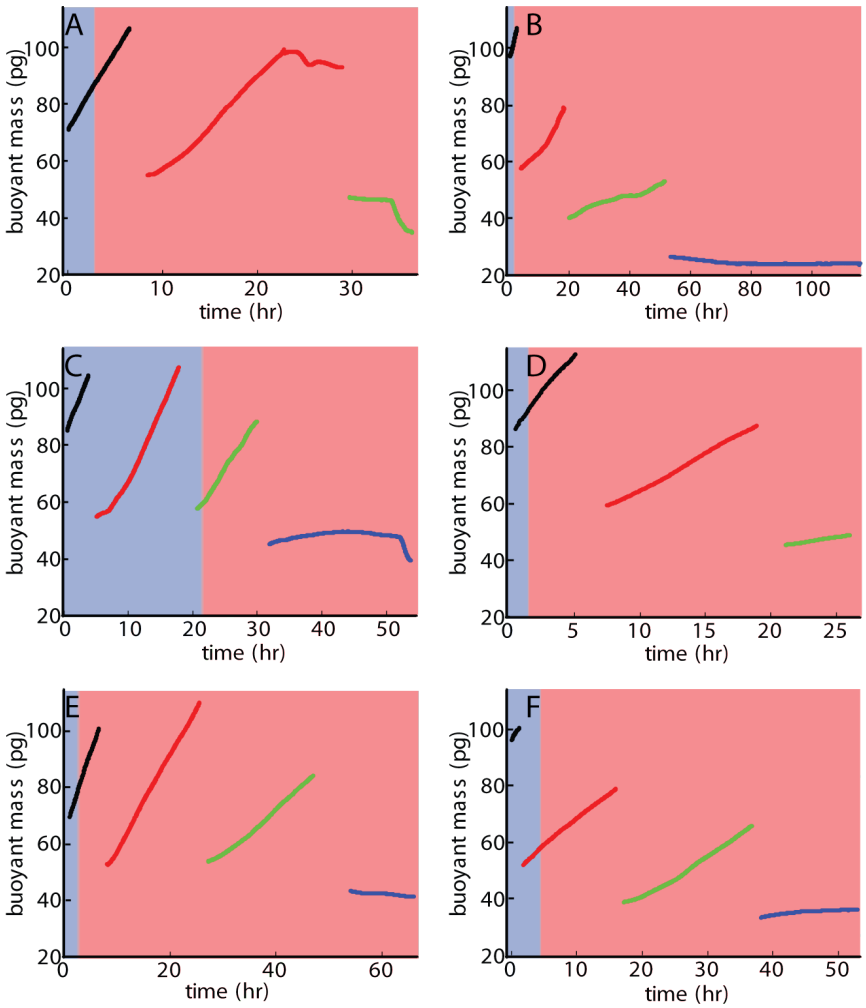

Supplementary Figure 4-3: Growth trajectories of individual cells before and after treatment with Torin1 (250 nM). Light blue indicates cell growing in media and red indicates cell treated with drug.

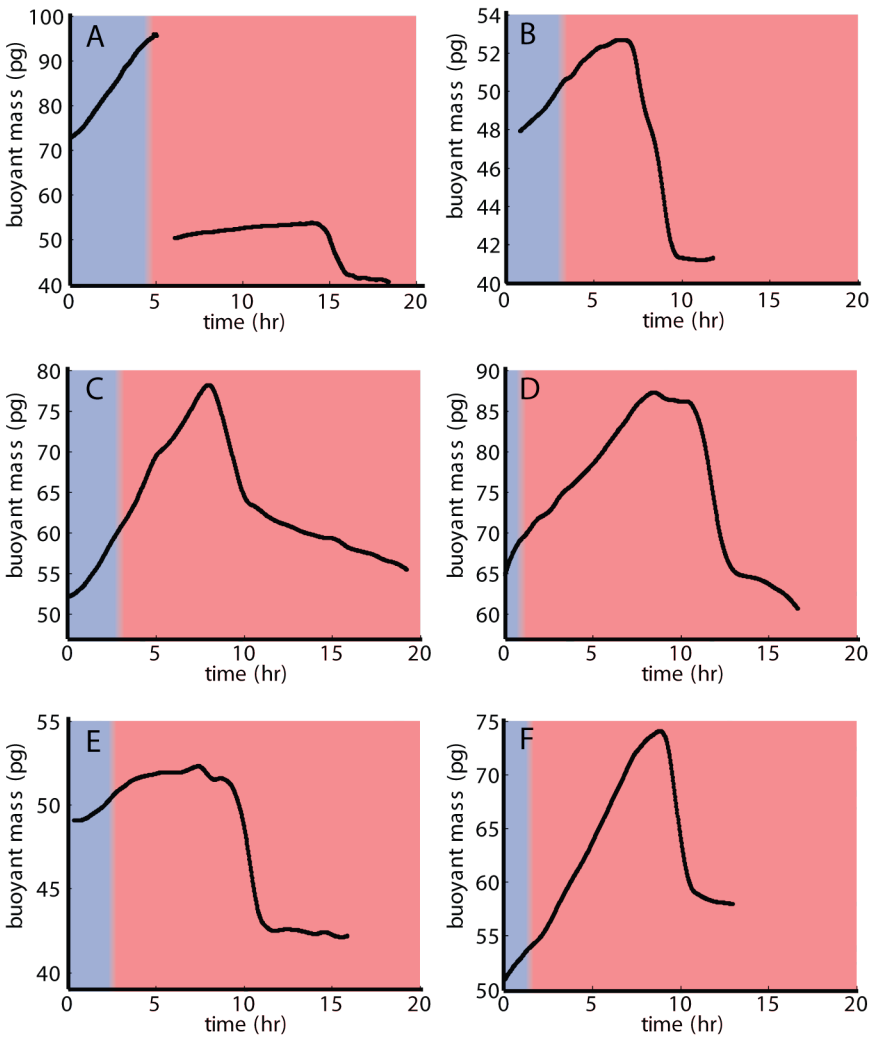

Supplementary Figure 4-4: Growth trajectories of individual cells before and after treatment with STS (3 μM). Light blue indicates cell growing in media and red indicates cell treated with drug.

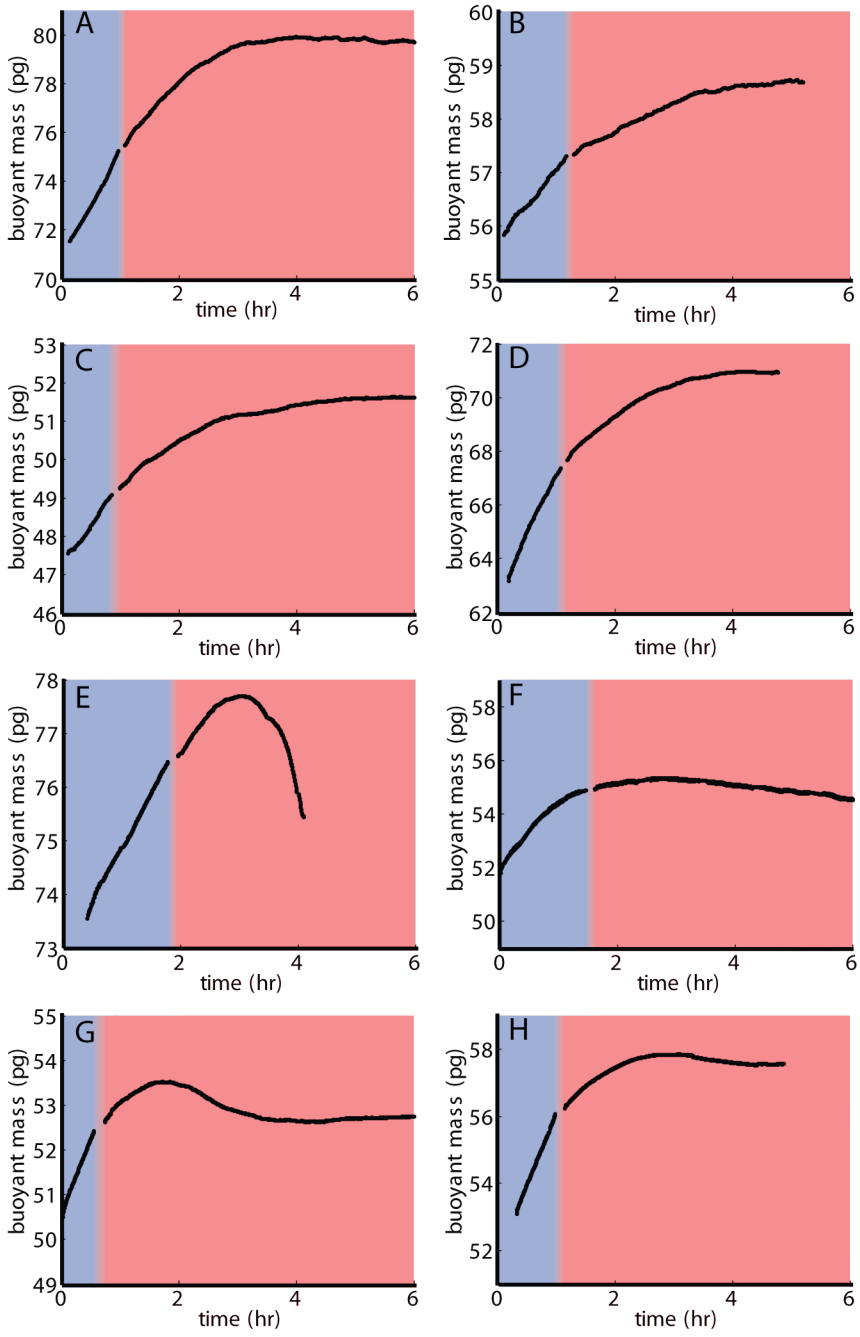

Supplementary Figure 4-5: Growth trajectories of individual cells before and after treatment with CHX (5 $\mu g\ mL^{-1}$). Light blue indicates cell growing in media and red indicates cell treated with drug.

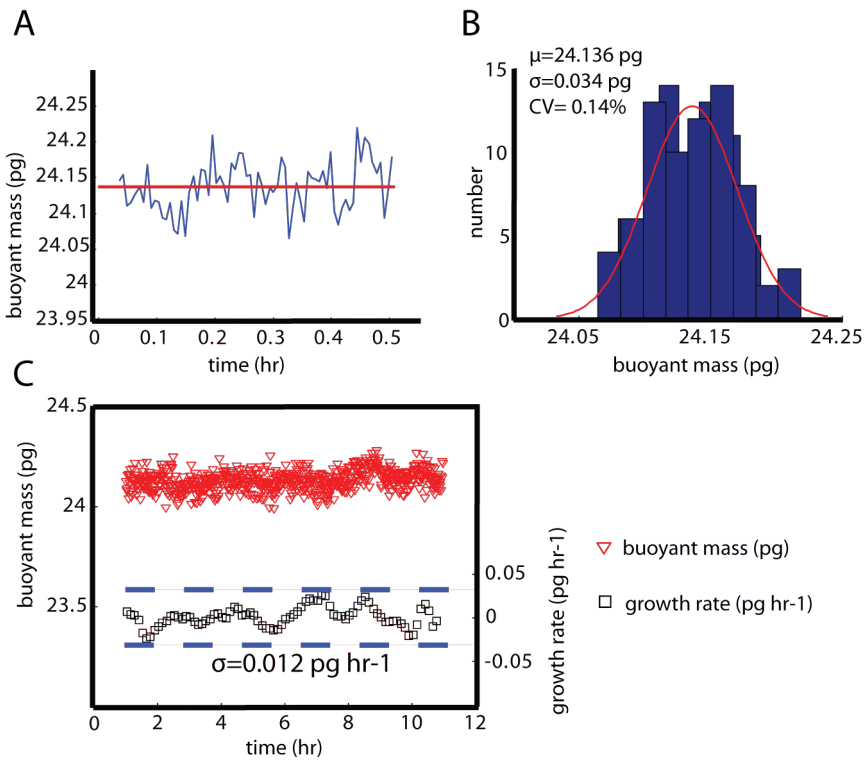

Supplementary Figure 4-6: Error analysis for the method. (A) thirty-minute trace of a trapped cell with no growth. (B) Gaussian fit on a histogram generated from repeated measurements of the same cell for thirty-minutes. (C) Buoyant mass and growth rate versus time plot of a trapped cell with no growth for 10 hours. The max and min of each serve as a good indication of error.

Chapter 5

Conclusions

Chapter 5

Conclusions

We approached the problem of understanding mammalian cellular behavior after drug intervention by tracking the growth and proliferation of individual cells. To monitor growth, we utilized the SMR mass sensor to measure the buoyant mass of cells with unparalleled precision. However, previous implementations of the SMR instrument can only record the mass of a cell once, i.e., in a flow through manner, but the process of quantifying mass accumulation requires multiple measurements of an individual cell.

We employed various single-cell manipulation techniques to enable both time-lapse measurements with the SMR and on-chip fluid exchange for drug delivery. After several iterations of instrument design, we developed the MMASS, a method that takes full advantage of laminar flow in the SMR device to allow periodic cell storage, repetitive mass measurements, and on-demand drug treatment. In addition to the femtogram level mass resolution of the SMR, what sets MMASS apart from other instruments in this area of research is its ability to investigate one or more generation of mammalian cell growth both before and after drug treatment. By measuring the same cell in both its native and its perturbed state, the method can make a fair comparison between a cell's normal behavior and its response to a drug therapy.

Although MMASS can perform its functions reliably without incidents of losing a cell during an experiment, a limitation to the method is that one system can only monitor one cell at a time. This can become extremely time-consuming if we are

trying to discover the behavior of rare or unusual cells in a population. Nevertheless, techniques to increase throughput are currently under development. For example, a new type of device, known as the serial SMR (or sSMR), contains a longer buried channel that can multiplex between a low number of cells ($N < 10$) at any given time. The sSMR can also study the growth dynamics of both daughter cells after a division event. In addition, we are also in the process of designing new devices which will contain anywhere between 100 to 1000 SMRs per chip.

Simultaneously, we are expanding into the area of translational research by seeking out clinical applications for MMASS. One unmet need for which the instrument can serve to fulfill is in the optimization of a personalized combinational therapy for cancer patients before or after surgery. At present, the treatment regimen is a standard course of radiation or chemotherapy based solely on the tumor's pathology. By screening the potency of drugs on individual cells taken from a biopsy or the patient's resected tumor, MMASS can pinpoint effective therapies against cells of varying genotypes. The results can then help a physician arrive at better treatment strategies to decrease the risk of metastases and improve a patient's quality of life by preemptively eliminating ineffective treatment options in vitro.

Appendix A

Drive and multiplier circuit

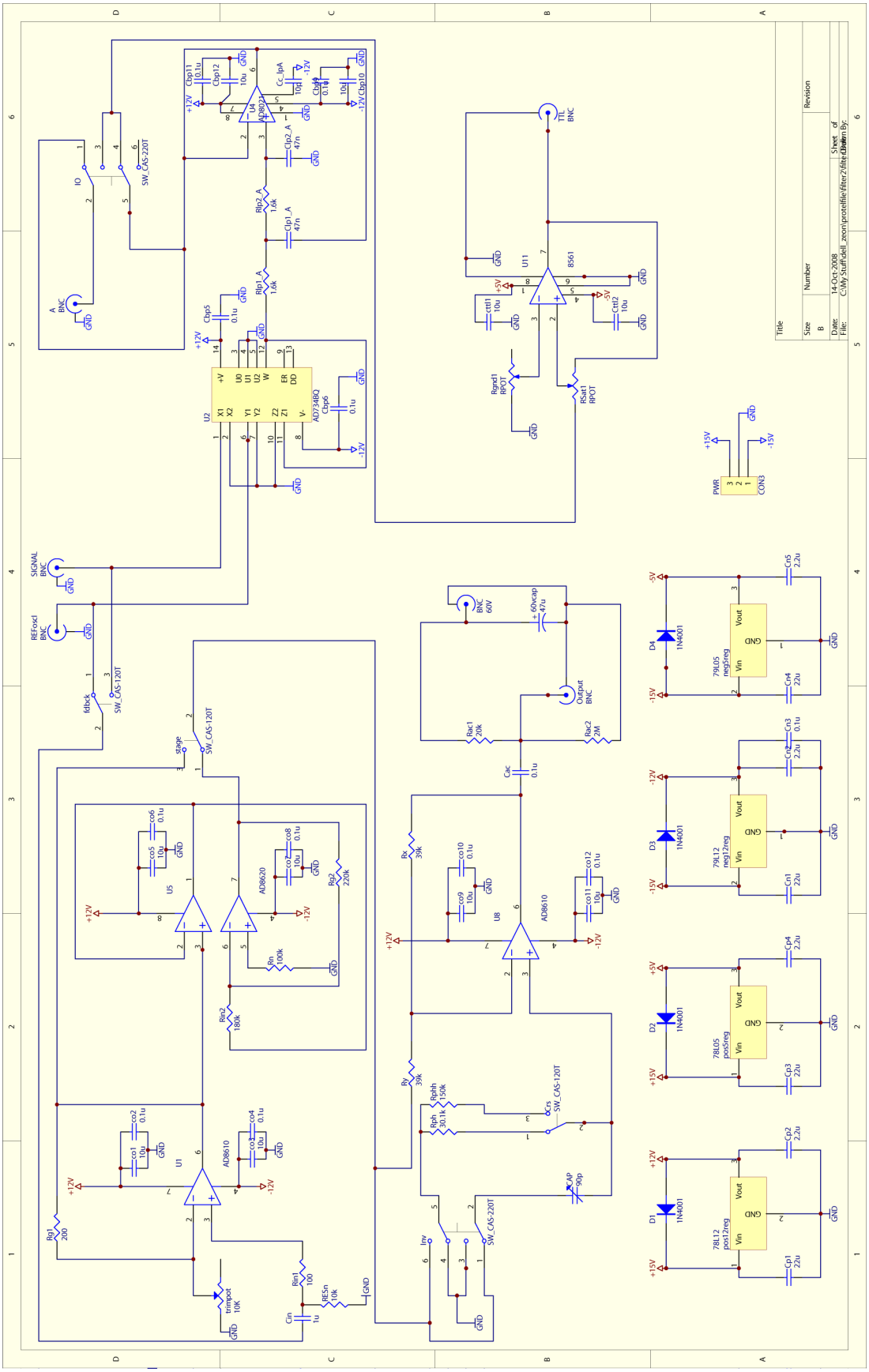

Figure A-1: The drive circuit optimizes the periodic signal from the photodetector board by amplifying and phase shifting it. The multiplier circuit convolves the periodic signal with a pure sine wave and filters for the lower frequency component, thereby resulting in a sinusoid with a frequency equivalent to the difference of the two input signals.

Appendix B

Supplementary material for chapter 2

Deriving Fluid Velocity Profile Within the SMR

Navier-Stokes equation in Cartesian coordinates:

$$\rho\left[\frac{dV_z}{dt} + V_x\frac{V_z}{dx} + V_y\frac{V_z}{dy} + V_z\frac{V_z}{dz}\right] = \rho g + \frac{dp}{dz} + \mu\left[\frac{d^2V_z}{dx^2} + \frac{d^2V_z}{dy^2} + \frac{d^2V_z}{dz^2}\right] \tag{B.1}$$

Inertial term is neglected because the flow is steady and fully developed without swirls.

$$\frac{1}{\mu}\frac{dP}{dz} = \left[\frac{d^2V_z}{dx^2} + \frac{d^2V_z}{dy^2}\right] \tag{B.2}$$

Suppose a cross section of the channel in the x-y plane yields a dimension of L_x x L_y. A solution of the form

$$V_z(x,y) = \sum_{m=1}^{\infty}\sum_{n=1}^{\infty} a_{m,n} cos\left(\frac{m\pi}{L_x}x\right) cos\left(\frac{n\pi}{L_y}y\right) \tag{B.3}$$

would yield 0 at x = $\frac{-L_x}{2}, \frac{L_x}{2}$ and at y = $\frac{-L_y}{2}, \frac{L_y}{2}$ because there is no-slip, or no flow, at the walls. Evaluating the RHS of (B.2) with (B.3), we get

$$\frac{1}{\mu}\frac{dP}{dz} = -\sum_{m=1}^{\infty}\sum_{n=1}^{\infty}\left[\left(\frac{n\pi}{L_x}\right)^2 + \left(\frac{m\pi}{L_y}\right)^2\right] a_{m,n} cos\left(\frac{m\pi}{L_x}x\right) cos\left(\frac{n\pi}{L_y}y\right) \tag{B.4}$$

Taking the Fourier series integral on both sides of (B.4) yields

$$\int_{\frac{-L_x}{2}}^{\frac{L_x}{2}}\int_{\frac{-L_y}{2}}^{\frac{L_y}{2}} \frac{1}{\mu}\frac{dP}{dz} cos\left(\frac{k\pi}{L_x}x\right) cos\left(\frac{l\pi}{L_y}y\right) dxdy = \int_{\frac{-L_x}{2}}^{\frac{L_x}{2}}\int_{\frac{-L_y}{2}}^{\frac{L_y}{2}}$$

$$-\sum_{m=1}^{\infty}\sum_{n=1}^{\infty}\left[\left(\frac{n\pi}{L_x}\right)^2 + \left(\frac{m\pi}{L_y}\right)^2\right] a_{m,n} cos\left(\frac{m\pi}{L_x}x\right) cos\left(\frac{n\pi}{L_y}y\right) cos\left(\frac{k\pi}{L_x}x\right) cos\left(\frac{l\pi}{L_y}y\right) dxdy$$

By the principle of orthogonality, the double sum collapses down to

$$\int_{\frac{-L_x}{2}}^{\frac{L_x}{2}} \int_{\frac{-L_y}{2}}^{\frac{L_y}{2}} \frac{1}{\mu} \frac{dP}{dz} cos\left(\frac{k\pi}{L_x}x\right) cos\left(\frac{l\pi}{L_y}y\right) dxdy$$

$$= \int_{\frac{-L_x}{2}}^{\frac{L_x}{2}} \int_{\frac{-L_y}{2}}^{\frac{L_y}{2}} -\left[\left(\frac{k\pi}{L_x}\right)^2 + \left(\frac{l\pi}{L_y}\right)^2\right] a_{k,l} cos^2\left(\frac{k\pi}{L_x}x\right) cos^2\left(\frac{l\pi}{L_y}y\right) dxdy \tag{B.5}$$

Evaluating the integral on both sides and solving for the Fourier series coefficient $a_{k,l}$, we find the solution

$$V_z(x,y) = \sum_{k=odd} \sum_{l=odd} a_{k,l} cos\left(\frac{k\pi}{L_x}x\right)\left(\frac{l\pi}{L_y}y\right) \tag{B.6}$$

where,

$$a_{k,l} = \frac{16}{kl\pi^2} \frac{1}{\mu} \frac{dP}{dz} \left[-\left(\frac{k\pi}{L_x}\right)^2 - \left(\frac{l\pi}{L_y}\right)^2 \right]^{-1} sin\left(\frac{k\pi}{2}\right) sin\left(\frac{l\pi}{2}\right) \tag{B.7}$$

For all even values of k and l, $a_{k,l}$=0. As a check to see if equation (B.6) is the complete solution, we evaluate the following solution into the RHS of (B.2)

$$V_z(x,y) = \sum_{m=1}^{\infty} \sum_{n=1}^{\infty} b_{m,n} sin\left(\frac{m\pi}{L_x}x\right) sin\left(\frac{n\pi}{L_y}y\right)$$

Taking the Fourier sine series integral for the LHS of (B.2), we get

$$\int_{\frac{-L_x}{2}}^{\frac{L_x}{2}} \int_{\frac{-L_y}{2}}^{\frac{L_y}{2}} \frac{1}{\mu} \frac{dP}{dz} sin\left(\frac{k\pi}{L_x}x\right) sin\left(\frac{l\pi}{L_y}y\right) dxdy = 0$$

Thus, all coefficients for the Fourier sine series, $b_{m,n}$, equal 0. Next we compute the average fluid velocity V_{avg} numerically.

$$\frac{1}{L_x L_y}\int\int_A V_z(x,y)\,dxdy = \left[\frac{1}{L_x L_y}\sum_{x=\frac{-L_x}{2}}^{\frac{L_x}{2}}\sum_{y=\frac{-L_y}{2}}^{\frac{L_y}{2}}\frac{V(x,y)}{dP/dz}\Delta x\Delta y\right]\frac{dP}{dz} = \tilde{v}\frac{dP}{dz} \tag{B.8}$$

We can relate pressure drop to flow rate,

$$Q = AV_{avg} = A\tilde{v}\frac{dP}{dz} \tag{B.9}$$

where $A = L_x Ly$, $\tilde{v}$ is computed numerically by (B.8), and $\frac{dP}{dz} \sim \frac{\Delta P}{\Delta z}$ across the SMR.

Displacement of micron-sized objects due to SMR oscillation

We want to calculate the displacement of nanometer to micron-sized objects due to SMR oscillation in the y-axis. The oscillation of the SMR and the fluid within is given by

$$y(t) = Acos(\omega t)$$

where A is the amplitude of oscillation and ω is the frequency of oscillation in radians.

$$v(t) = \frac{dy(t)}{dt} = -A\omega sin(\omega t)$$

Applying Stoke's law, we find that the drag force on an object is

$$F = ma = 6\pi\mu r\big[V_{fluid} - v_p\big] \tag{B.10a}$$

$$\frac{dv_p}{dt} = \frac{6\pi\mu r}{\rho\frac{4}{3}\pi r^3}\big[-A\omega sin(\omega t) - v_p\big] \tag{B.10b}$$

Let Φ be defined as the constant $\frac{6\mu}{\rho\frac{4}{3}r^2}$ where r is the radius of the object, ρ is the density difference between the cell and the fluid medium, and μ is the viscosity of the fluid. Alternatively, we can define Φ as $\frac{6\mu r}{m_b}$, a ratio of viscosity to buoyant mass. We rewrite equation (B.10b) as a first order differential equation

$$\frac{dv_p}{dt} + \Phi v_p = -\Phi A\omega sin(\omega t) \tag{B.11}$$

The general solution to equation (B.11) is

$$v_p = c_1 exp(-\Phi t) \tag{B.12}$$

The particular solution to equation (B.11) is

$$v_p = c_2 cos(\omega t) + c_3 sin(\omega t) \tag{B.13}$$

Evaluating the LHS of equation (B.11) with equation (B.13), we get

$$(c_3\omega + \Phi c_2)cos(\omega t) + (\Phi c_3 - c_2\omega)sin(\omega t) = -\Phi A\omega sin(\omega t)$$

$$c_2 = \frac{\Phi A\omega^2}{\omega^2 + \Phi^2} \tag{B.14}$$

$$c_3 = \frac{-\Phi A^2\omega}{\omega^2 + \Phi^2} \tag{B.15}$$

We superimpose the general (B.12) and particular (B.13) solutions and evaluate (B.14) and (B.15) into (B.13).

$$v_p = c_1 exp(-\Phi t) + \frac{\Phi A\omega^2}{\omega^2 + \Phi^2} cos(\omega t) - \frac{\Phi A^2\omega}{\omega^2 + \Phi^2} sin(\omega t)$$

Applying the boundary condition $v_p = 0$ at $t = 0$, we obtain the complete solution for an object's oscillation velocity within the SMR.

$$v_p = -\frac{\Phi A\omega^2}{\omega^2 + \Phi^2} exp(-\Phi t) + \frac{\Phi A\omega^2}{\omega^2 + \Phi^2} cos(\omega t) - \frac{\Phi^2 A\omega}{\omega^2 + \Phi^2} sin(\omega t) \tag{B.16}$$

where $\Phi = \frac{6\mu r}{m_b}$. To find the displacement of the object in the y-axis, we take the following integral and evaluate the boundary condition $y_p = A$ at $t = 0$.

$$y_p = \int v_p dt = \frac{A}{\omega^2 + \Phi^2}\left[\omega^2 exp(-\Phi t) + \Phi\omega sin(\omega t) + \Phi^2 cos(\omega t)\right] \tag{B.17}$$

Appendix C

Supplementary material for chapter 3

Centrifugal force on an object from the SMR's oscillation

An object near the SMR apex will experience a centrifugal force due to the cantilever's oscillation. To express this analytically, we employ the following equation:

$$F_c = \rho\frac{4}{3}\pi r^3\frac{{v_p}^2}{L} \tag{C.1}$$

where $\rho\frac{4}{3}\pi r^3$ is the buoyant mass of the object with radius r, ρ is the density difference between the object and the fluid medium, v_p is the velocity of oscillation given in (B.16), and L is the length of the cantilever. We can further solve for the velocity, v_c, of the object in the outward direction by a force balance between the centrifugal force (C.1) and Stoke's law.

$$v_c = \frac{2}{9}\frac{\rho r^2}{\mu}\frac{{v_p}^2}{L} \tag{C.2}$$

Next, since v_p is periodic and time-dependent, we integrate (C.1) and (C.2) over an entire oscillation period T, where $T = \frac{2\pi}{\omega}$. Because we are assuming steady state, the exponential (transient) term from (B.16) is ignored.

$$\mathbf{F_c} = \frac{1}{\mathrm{L}}\left[\rho\frac{4}{3}\pi\mathrm{r}^3\right]\left[\frac{1}{\mathrm{T}}\int_0^{\mathrm{T}}{\mathrm{v_p}}^2\mathrm{dt}\right] = \frac{1}{2\mathrm{L}}\left[\rho\frac{4}{3}\pi\mathrm{r}^3\right]\left[\left(\frac{\Phi\mathrm{A}\omega^2}{\omega^2+\Phi^2}\right)^2+\left(\frac{\Phi^2\mathrm{A}\omega}{\omega^2+\Phi^2}\right)^2\right] \tag{C.3}$$

$$\mathbf{v_c} = \frac{2}{9}\frac{\rho\mathrm{r}^2}{\mu\mathrm{L}}\left[\frac{1}{\mathrm{T}}\int_0^{\mathrm{T}}{\mathrm{v_p}}^2\mathrm{dt}\right] = \frac{1}{9}\frac{\rho\mathrm{r}^2}{\mu\mathrm{L}}\left[\left(\frac{\Phi\mathrm{A}\omega^2}{\omega^2+\Phi^2}\right)^2+\left(\frac{\Phi^2\mathrm{A}\omega}{\omega^2+\Phi^2}\right)^2\right] \tag{C.4}$$

Evaluating the integral, we get the average centrifugal force, $\mathbf{F_c}$, applied on an object near the apex of the SMR and the average velocity, $\mathbf{v_c}$, of the object in the outward direction due to the cantilever's oscillation.

On a 15x20 μm cantilever, electrostatic actuation will result in an oscillation amplitude equivalent to tens of nanometers, an amount too small for any centrifugal force to be realized. To achieve an oscillation amplitude above $\sim$100 nm where the effects of the centrifugal force are substantial, we require the use of a piezoelectric crystal for actuation. Figure C-1A plots the average centrifugal acceleration on a

10 μm object versus a range of ρ, a good indication of buoyant mass, m_b, for three different viscosities. Figure C-1B plots the average velocity on a 10 μm object versus ρ for the same viscosities. Both plots assume a cantilever oscillation amplitude of 200 nm.

According to Figure C-1A, for a given viscosity the object will experience the greatest centrifugal acceleration when it has a low m_b. As discussed in chapter 3, an object with little or no inertial effect will follow the oscillation of the cantilever exactly and will thus experience the maximum average centrifugal acceleration. As m_b increases, the object's inertial effects reduce its amplitude of oscillation and thereby decrease the average outward acceleration. As the viscosity of the fluid increases, the object's inertial effects are increasingly mitigated by the fluidic resistance. This causes the object's amplitude of oscillation to approach that of the cantilever. Thus, for a given m_b, the object will experience a greater acceleration at a higher fluid viscosity.

According to Figure C-1B, an object with m_b=0 does not move. It is essentially weightless and does not feel a force regardless of the acceleration applied. As the m_b of an object increases from zero, the velocity will initially increase. However, at some threshold m_b the inertial effects of the object takes over and any increase in mass will substantially decrease velocity. An increase in viscosity will increase the m_b threshold required for inertial effects of the object to become substantial. As an extreme case of high viscosity (black curve), the object's outward velocity remains low for a given m_b despite a large acceleration as seen in Figure B-1. This is because the fluid viscosity is hindering the object from moving outward quickly.

Based on the predicted values in Figure C-1B, a polystyrene bead $\rho = 1.05\ g\ cm^{-3}$ in water would have an average velocity of $\sim$26 $\mu m\ s^{-1}$. As we had determined empirically, it would be able to move into the column traps at the apex of the cantilever well within 1 s.

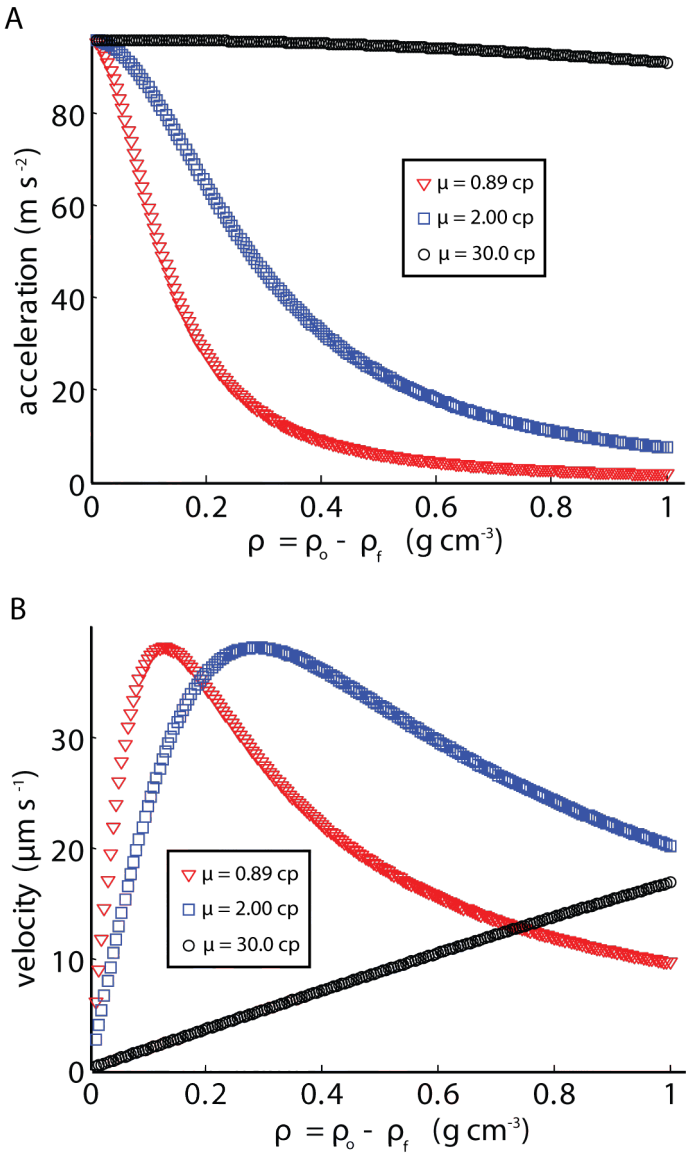

Figure C-1: A) Average centrifugal acceleration ($m\ s^{-2}$) versus ρ for a 10 μm object in three different viscosities. B) Average outward velocity ($\mu m\ s^{-1}$) versus ρ for a 10 μm object in three different viscosities.